



저작자표시-변경금지 2.0 대한민국

이용자는 아래의 조건을 따르는 경우에 한하여 자유롭게

- 이 저작물을 복제, 배포, 전송, 전시, 공연 및 방송할 수 있습니다.
- 이 저작물을 영리 목적으로 이용할 수 있습니다.

다음과 같은 조건을 따라야 합니다:



저작자표시. 귀하는 원저작자를 표시하여야 합니다.



변경금지. 귀하는 이 저작물을 개작, 변형 또는 가공할 수 없습니다.

- 귀하는, 이 저작물의 재이용이나 배포의 경우, 이 저작물에 적용된 이용허락조건을 명확하게 나타내어야 합니다.
- 저작권자로부터 별도의 허가를 받으면 이러한 조건들은 적용되지 않습니다.

저작권법에 따른 이용자의 권리는 위의 내용에 의하여 영향을 받지 않습니다.

이것은 [이용허락규약\(Legal Code\)](#)을 이해하기 쉽게 요약한 것입니다.

[Disclaimer](#)

공학박사 학위논문

**Frequency-domain Seismic Full
Waveform Inversion for 2-D Elastic
VTI Media**

2차원 횡등방성 탄성매질에 대한 주파수영역
탄성과 완전파형역산

2014년 8월

서울대학교 대학원

공과대학 에너지시스템공학부

김 원 기

Frequency-domain Seismic Full Waveform Inversion for 2-D Elastic VTI Media

2차원 횡등방성 탄성매질에 대한 주파수영역
탄성과 완전파형역산

지도 교수 민 동 주

이 논문을 공학박사 학위논문으로 제출함
2014년 5월

서울대학교 대학원
공과대학 에너지시스템공학부
김 원 기

김원기의 박사 학위논문을 인준함
2014년 6월

위 원 장 _____ (인)

부위원장 _____ (인)

위 원 _____ (인)

위 원 _____ (인)

위 원 _____ (인)

Abstract

Frequency-domain Seismic Full Waveform Inversion for 2-D Elastic VTI Media

Won-Ki Kim

Department of Energy Systems Engineering
The Graduate School
Seoul National University

I present a new parameterization method to improve the results of seismic full waveform inversion (FWI) for 2-D elastic VTI media. In the new parameterization method, the elastic parameters of C_{11} , C_{13} , C_{33} and C_{44} are replaced with the Lamé constants and the newly introduced parameters of ξ_1 and ξ_2 for anisotropic properties.

For multi-parametric FWI, a sequential inversion strategy is used: the primary parameters, which are inverted well and have strong influences on the data are inverted first, and the secondary parameters are inverted using the inverted primary parameters. In conventional VTI parameterization, C_{33} and C_{44} are chosen as the primary parameters, whereas the Lamé constants are the primary parameters in the new parameterization.

The new parameterization method is distinguished from the conventional VTI parameterization in the scattering patterns of the partial derivative wavefields with respect to the primary parameters. The scattering patterns of the Lamé constants are similar to those of the isotropic case. Because the Lamé constants are inverted well in the isotropic case, they can also be inverted well in the new parameterization. On the other hand, because ξ_1 and ξ_2 have the same scattering patterns as those of C_{11} and C_{13} , we cannot expect any improvements directly. The gradient directions showed that the resolution of

the gradient direction for μ can be improved. Although ξ_1 and ξ_2 in the new parameterization retain the characteristics of C_{11} and C_{13} used in the conventional VTI parameterization, the improved primary parameters (Lamé constants) affect the new parameters positively. Thus, the inversion results for anisotropic parameters can be improved. Synthetic FWI examples for the SEG/EAGE overthrust model and the SEG/HESS VTI model indicated that the new parameterization method provides more reliable subsurface properties than the conventional and sequential inversion methods. In addition, the inversion with new parameterization has better computational efficiency than the sequential inversion because it inverts all the parameters simultaneously and does not require an additional inversion stage. Therefore, our parameterization method can overcome the intrinsic disadvantages of the elastic inversion for VTI media.

To apply the new parameterization to real seismic data, it is necessary to increase its applicability to noisy and low-frequency missing data and to extend it to a 3-D case.

Keywords: seismic full waveform inversion (FWI), multi-parameter, vertical transverse isotropic (VTI), parameterization, elastic
Student Number: 2010-31015

Contents

Abstract	i
Contents	iii
List of Tables	v
List of Figures	vi
Chapter 1. Introduction	1
1.1 Seismic Full Waveform Inversion.....	1
1.2 Research Objectives.....	6
Chapter 2. Theory	7
2.1 Transverse Isotropic Media.....	7
2.1.1 Linear elasticity of earth media.....	7
2.1.2 Vertical transverse isotropic media	9
2.2 Forward Problems	15
2.2.1 Finite-element formula of the elastic wave equations.....	15
2.2.2 PML boundary condition	20
2.2.3 Verification of forward modeling algorithm	23
2.3 Inverse Problems.....	29
2.3.1 Seismic FWI using the l_2 -norm-based objective function.....	29
2.3.2 Preconditioned gradient direction	30

2.3.3 Conjugate gradient method and Source wavelet estimation	31
Chapter 3. New Parameterization.....	34
3.1 Former studies on seismic FWI for VTI media	34
3.2 New Parameterization.....	38
3.3 Sensitivity Analysis.....	42
3.3.1 Scattering patterns of partial derivative wavefields.	42
3.3.2 Comparisons of gradient directions	52
Chapter 4. Synthetic Examples.....	60
4.1 The SEG/EAGE Overthrust Model.....	61
4.1.1 Modified version of the overthrust model.....	61
4.1.2 Original version of the SEG/EAGE overthrust model	78
4.2 The SEG/HESS VTI model	93
4.2.1 Modified SEG/HESS VTI model.....	93
Chapter 5. Conclusions	113
Bibliography	117
초 록	123

List of Tables

Table 3.1 Elastic properties used to obtain partial derivative wavefields with respect to model parameters.	44
Table 3.2 Elastic properties of the simple two-layered model for the computation of gradient directions.	54
Table 4.1 Model mismatch errors of the final inversion results obtained by the conventional, sequential and new inversions for the modified version of the SEG/EAGE overthrust model.	76
Table 4.2 Computing time for one inversion iteration step for the modified version of the SEG/EAGE overthrust model.....	77
Table 4.3 Model mismatch errors of the final inversion results obtained by the conventional, sequential and new inversions for the original version of the SEG/EAGE overthrust model.....	92
Table 4.4 Model mismatch errors of the final inversion results obtained by the conventional, sequential and new inversions for the SEG/HESS VTI model.	112

List of Figures

Figure 1.1 Schematic image of seismic exploration.....	2
Figure 1.2 Workflow of the conventional seismic full waveform inversion.	3
Figure 2.1 (upper) Isotropic and (lower) vertical transverse isotropic media. ...	10
Figure 2.2 P-wave velocity variations with increasing ε : (black solid line) vertical P-wave velocity, (red solid line) horizontal P-wave velocity and (blue dashed line) ratio of horizontal and vertical P-wave velocities.....	14
Figure 2.3 Model dimension with PML boundary zone.....	22
Figure 2.4 Homogeneous model with single source-receiver geometry.....	24
Figure 2.5 Comparison of analytic and numerical solutions for (a) horizontal and (b) vertical displacements. Black solid and red dashed lines represent numerical and analytic solutions, respectively.....	25
Figure 2.6 Snapshots of (a, c and e) horizontal and (b, d and f) vertical displacements at $t = 0.968$ s, when δ is fixed at 0.0.	27
Figure 2.7 Snapshots of (a, c and e) horizontal and (b, d and f) vertical displacements at $t = 0.968$ s, when ε is fixed at 0.2.....	28
Figure 3.1 Global and local minimum points.	37
Figure 3.2 Workflow of the seismic FWI using the new parameterization.	41
Figure 3.3 Scattering patterns of horizontal (left) and vertical (right) components of partial derivative wavefields with respect to λ (a and b), μ (c and d) and ρ (e and f) for the isotropic parameterization.	46
Figure 3.4 Scattering patterns of horizontal (left) and vertical (right) components of partial derivative wavefields with respect to C_{11} (a and	

b), C_{13} (c and d), C_{33} (e and f), C_{44} (g and h) and ρ (i and j) for the conventional VTI parameterization.	47
Figure 3.5 Scattering patterns of horizontal (left) and vertical (right) components of partial derivative wavefields with respect to λ (a and b), μ (c and d), ξ_1 (e and f), ξ_2 (g and h) and ρ (i and j) for the conventional VTI parameterization.	50
Figure 3.6 Horizontal two-layered model and seismic survey geometry used to obtain gradient directions.	53
Figure 3.7 Normalized gradient directions in the first iteration for the simple two-layered model obtained by the conventional VTI parameterization: (a) C_{11} , (b) C_{13} , (c) C_{33} and (d) C_{44}	57
Figure 3.8 Normalized gradient directions in the first iteration for the simple two-layered model obtained by the new parameterization: (a) ξ_1 , (b) ξ_2 , (c) λ and (d) μ	58
Figure 3.9 Amplitude logs of the normalized gradient directions with respect to each parameter obtained by (black solid lines) the conventional and (red dashed lines) new parameterizations for VTI media: (a) C_{11} and ξ_1 , (b) C_{13} and ξ_2 , (c) C_{33} and λ and (d) C_{44} and μ . The logs are extracted at distances of (left) 1.0 km, (center) 1.3 km and (right) 1.7 km, respectively.	59
Figure 4.1 Modified versions of the SEG/EAGE overthrust models distributed by Delft University: (a) C_{11} , (b) C_{13} , (c) C_{33} , (d) C_{44} , (e) ρ , (f) ε and (g) δ . Poisson's ratio is fixed at 0.25, and the density is regenerated using the Gardner's relationship.	63
Figure 4.2 Seismic FWI results obtained by the isotropic inversion algorithm based on the Lamé constants parameterization for the modified version of the SEG/EAGE overthrust model: (a) C_{33} , (b) C_{44} and (c) ρ . C_{33} and C_{44} can be obtained from the inverted Lamé constants.	64

Figure 4.3 Elastic parameter logs extracted at a distance of 3 km of the (black solid lines) true, (gray solid lines) initial and inverted (red solid lines) models obtained by the isotropic inversion algorithm: (a) C_{33} , (b) C_{44} and (c) ρ **65**

Figure 4.4 Inversion results obtained by the conventional VTI parameterization for the modified version of the SEG/EAGE overthrust models: (a) C_{11} , (b) C_{13} , (c) C_{33} , (d) C_{44} , (e) ρ , (f) ε and (g) δ **67**

Figure 4.5 Inversion results obtained by the sequential (isotropic-anisotropic) inversion strategy for the modified version of the SEG/EAGE overthrust models: (a) C_{11} , (b) C_{13} , (c) C_{33} , (d) C_{44} , (e) ρ , (f) ε and (g) δ . The inversion results obtained by the isotropic inversion in Figure 4.2 are used for initial guesses..... **68**

Figure 4.6 Inversion results obtained by the new parameterization for the modified version of the SEG/EAGE overthrust models: (a) C_{11} , (b) C_{13} , (c) C_{33} , (d) C_{44} , (e) ρ , (f) ε and (g) δ **70**

Figure 4.7 Elastic parameter logs extracted at a distance of 3 km of the (black solid lines) true and inverted models obtained by (black dashed lines) the conventional, (blue solid lines) the sequential and (red solid lines) the new inversion: (a) C_{11} , (b) C_{13} , (c) C_{33} , (d) C_{44} , (e) ρ , (f) ε and (g) δ **71**

Figure 4.8 RMS error curves for (black solid line) the conventional VTI inversion, (gray dashed line) the isotropic inversion for first stage of the sequential inversion, (blue solid line) the conventional VTI inversion for second stage of the sequential inversion and (red solid line) new inversion for the modified version of the SEG/EAGE overthrust model..... **75**

Figure 4.9 Original versions of the SEG/EAGE overthrust models distributed by Delft University: (a) C_{11} , (b) C_{13} , (c) C_{33} , (d) C_{44} , (e) ρ , (f) ε , (g) δ

and (h) Poisson's ratio.	79
Figure 4.10 The starting models of seismic inversion for the original version of the SEG/EAGE overthrust model: (a) C_{11} , (b) C_{13} , (c) C_{33} , (d) C_{44} and (e) ρ	80
Figure 4.11 Inversion results obtained by the conventional VTI parameterization for the original version of the SEG/EAGE overthrust models: (a) C_{11} , (b) C_{13} , (c) C_{33} , (d) C_{44} , (e) ρ , (f) ε and (g) δ	83
Figure 4.12 Inversion results obtained by the sequential inversion strategy for the original version of the SEG/EAGE overthrust models: (a) C_{11} , (b) C_{13} , (c) C_{33} , (d) C_{44} , (e) ρ , (f) ε and (g) δ . The inversion results obtained by the isotropic inversion (not presented in this dissertation) are used for the initial models.	84
Figure 4.13 Inversion results obtained by the new parameterization for the original version of the SEG/EAGE overthrust models: (a) C_{11} , (b) C_{13} , (c) C_{33} , (d) C_{44} , (e) ρ , (f) ε and (g) δ	85
Figure 4.14 Elastic parameter logs extracted at a distance of 3 km of the (black solid lines) true and inverted models obtained by (black dashed lines) the conventional, (blue solid lines) the sequential and (red solid lines) the new inversion: (a) C_{11} , (b) C_{13} , (c) C_{33} , (d) C_{44} , (e) ρ , (f) ε and (g) δ	86
Figure 4.15 (a) True and reconstructed Poisson's ratio obtained by (b) the conventional, (c) the sequential and (d) the new inversion for	89
Figure 4.16 Poisson's ratio logs extracted at a distance of 3 km of the (black solid lines) true and inverted models obtained by (black dashed lines) the conventional, (blue solid lines) the sequential and (red solid lines) the new inversion.....	90
Figure 4.17 RMS error curves for (black solid line) the conventional VTI inversion, (gray dashed line) the isotropic inversion for first stage of the sequential inversion, (blue solid line) the conventional VTI	

inversion for second stage of the sequential inversion and (red solid line) new inversion.	91
Figure 4.18 The SEG/Hess VTI models: (a) C_{11} , (b) C_{13} , (c) C_{33} , (d) C_{44} , (e) ρ , (f) ε and (g) δ	94
Figure 4.19 The initial guesses of seismic inversion for the SEG/HESS VTI models: (a) C_{11} , (b) C_{13} , (c) C_{33} , (d) C_{44} and (e) ρ	95
Figure 4.20 Seismic FWI results obtained by the isotropic inversion algorithm based on the Lamé constants parameterization for the SEG/HESS VTI model: (a) C_{33} , (b) C_{44} and (c) ρ . C_{33} and C_{44} can be obtained from the Lamé constants (λ and μ).....	97
Figure 4.21 Elastic parameter logs extracted at a distance of 2.26 km of the (black solid lines) true, (gray solid lines) initial and inverted (red solid lines) models: (a) C_{33} , (b) C_{44} and (c) ρ . Inversion results are obtained by the isotropic inversion algorithm.	98
Figure 4.22 Elastic parameter logs extracted at a distance of 4.52 km of the (black solid lines) true, (gray solid lines) initial and inverted (red solid lines) models: (a) C_{33} , (b) C_{44} and (c) ρ . Inversion results are obtained by the isotropic inversion algorithm.	99
Figure 4.23 Inversion results obtained by the conventional VTI parameterization for the SEG/HESS VTI model: (a) C_{11} , (b) C_{13} , (c) C_{33} , (d) C_{44} , (e) ρ , (f) ε and (g) δ	101
Figure 4.24 Inversion results obtained by the sequential inversion: (a) C_{11} , (b) C_{13} , (c) C_{33} , (d) C_{44} , (e) ρ , (f) ε and (g) δ . The inversion results obtained by the isotropic inversion in Figure 4.16 are used for the initial models.	102
Figure 4.25 Inversion results obtained by the new parameterization: (a) C_{11} , (b) C_{13} , (c) C_{33} , (d) C_{44} , (e) ρ , (f) ε and (g) δ	103
Figure 4.26 Elastic parameter logs extracted at a distance of 2.26 km of the (black solid lines) true and inverted models obtained by (black dashed	

lines) the conventional, (blue solid lines) the sequential and (red solid lines) the new inversion: (a) C_{11} , (b) C_{13} , (c) C_{33} , (d) C_{44} , (e) ρ , (f) ε and (g) δ **104**

Figure 4.27 Elastic parameter logs extracted at a distance of 4.52 km of the (black solid lines) true and inverted models obtained by (black dashed lines) the conventional, (blue solid lines) the sequential and (red solid lines) the new inversion: (a) C_{11} , (b) C_{13} , (c) C_{33} , (d) C_{44} , (e) ρ , (f) ε and (g) δ **106**

Figure 4.28 (a) True and reconstructed Poisson’s ratio obtained by (b) the conventional, (c) the sequential and (d) the new inversion for the SEG/HESS VTI model. **109**

Figure 4.29 Poisson’s ratio logs extracted at a distance of (a) 2.26 km and (b) 4.52 km of the (black solid line) true and inverted models obtained by (black dashed lined) the conventional, (blue solid line) the sequential and (red solid lines) the new inversion for the SEG/HESS VTI model. **110**

Figure 4.30 RMS error curves for (black solid line) the conventional VTI inversion, (gray dashed line) the isotropic inversion for first stage of the sequential inversion, (blue solid line) the conventional VTI inversion for second stage of the sequential inversion and (red solid line) new inversion for the SEG/HESS VTI model..... **111**

Chapter 1. Introduction

1.1 Seismic Full Waveform Inversion

Seismic exploration uses artificial controlled seismic sources to acquire seismic data for the interpretation of subsurface structures and physical properties. Seismic data are records of seismic waves that arrive at receivers (Figure 1.1). Thus, recorded signals reflect subsurface information because they are influenced by subsurface structures and the physical properties of the medium through which they travel. Therefore, we can infer the subsurface structures and properties through appropriate data processing procedures.

Seismic full waveform inversion (FWI) is a method for inferring subsurface structures and properties by minimizing differences between modeled and field data (Tarantola, 1984; Pratt, 1999; Shin and Min, 2006; Guitton and Symes, 2003; Virieux and Operto, 2009). Seismic FWI can be used for reservoir characterization and to monitor reservoirs in oil and gas exploration or exploitation (Brossier et al., 2009) as well as for monitoring CO₂ capture and storage (CCS) projects (Gosselet and Singh, 2007). In the FWI, subsurface structures and properties are obtained by updating model parameters using computed model perturbations during the inversion process (Figure 1.2). Model perturbations can be computed using the modeled and field data, and the seismic FWI can be performed based on seismic wave equations in the time or frequency domains.

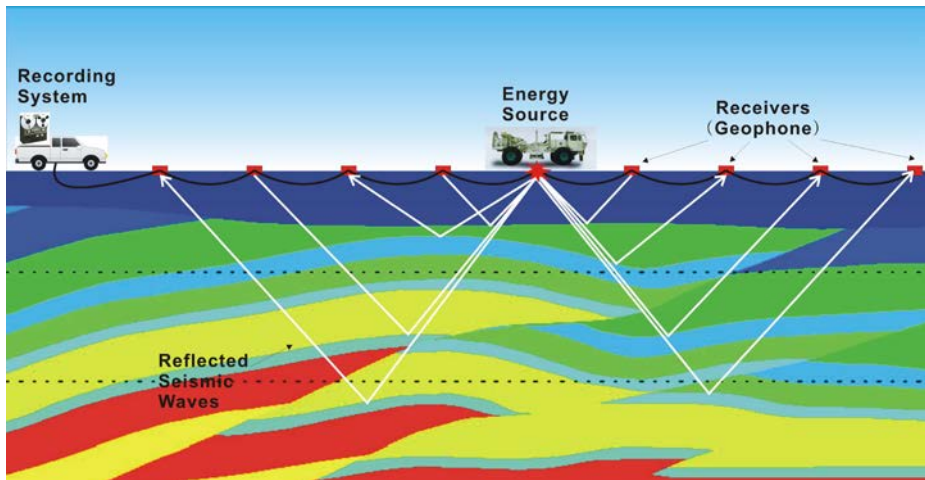


Figure 1.1 Schematic image of seismic exploration.

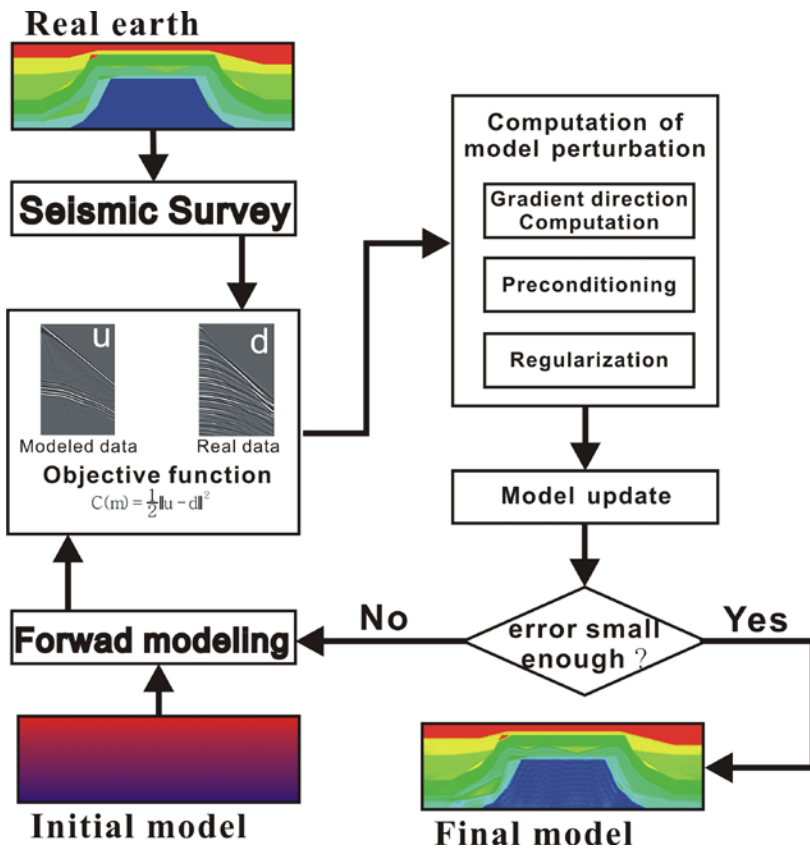


Figure 1.2 Workflow of the conventional seismic full waveform inversion.

Unfortunately, it is difficult to perfectly simulate seismic wave propagation through numerical simulations because real earth media have many unknown factors and complexities. For this reason, it is also difficult to extract accurate subsurface information by seismic FWI. Furthermore, FWI has been performed under the assumptions that subsurface media can be regarded as acoustic or elastic, isotropic or anisotropic, and homogeneous or inhomogeneous. However, some simple assumptions can result in degraded FWI results.

Recently, the need for seismic FWI that considers the intrinsic characteristics of actual subsurface media has increased because the targets of seismic surveys are often complex structures, such as sub-salt, sub-basalt and anisotropic layers. Thus, considering these characteristics is becoming increasingly important to improving results and increasing the validity of FWI. Among the intrinsic properties, anisotropy is an important property of subsurface media because shale, commonly encountered in both conventional and unconventional reservoirs can be characterized as a vertical transverse isotropic (VTI) medium, which is the simplest version of anisotropy. Shale often serves as a caprock of the reservoir or as the reservoir itself. Therefore, we need to consider the anisotropic properties of subsurface media to improve oil and gas exploration accuracy.

To obtain more accurate inversion results with FWI in anisotropic media, we need to address the difficulties associated with multi-parametric FWI. In the case of FWI for VTI media, the number of parameters increases because the anisotropic parameters are also inverted. This means that the possibility of

becoming trapped in local minima increases during the FWI process. Furthermore, the anisotropic properties are more difficult to estimate by seismic FWI than the P- and S-wave velocities or the Lamé constants. To overcome these difficulties, many studies have focused on FWI for VTI media. Several of these studies are based on the pseudo-acoustic wave equations (Alkhalifah, 1998; Duveneck and Bankker, 2011; Operto et al., 2009; Plessix and Cao, 2011; Zhou et al., 2006). Fewer parameters are inverted when the pseudo-acoustic wave equations are used than when the full elastic wave equations are used. In this case, although the possibility of being stuck in local minima is reduced by the decreasing of parameters, we cannot obtain information of shear modulus when the pseudo-acoustic approximation is applied. In contrast, several studies have been carried out based on the full elastic wave equations (Gholami et al., 2010; Koo et al., 2010; Lee et al., 2010). In this case, a strategy such as sequential inversion is needed to improve the inversion results for all the parameters. Unfortunately, the sequential inversions require an additional inversion stage to improve the inversion results for anisotropic parameters, and it is challenging when processing large amounts of seismic data, such as 2-D wide angle and 3-D data. Therefore, we need to develop a computationally efficient technique to improve inversion results for VTI media.

1.2 Research Objectives

As the targets of seismic explorations become more complex, we need to employ new inversion techniques to infer reliable subsurface material properties. In general, the reliability and accuracy of seismic FWI results are associated with partial derivative wavefields with respect to model parameters, which are dependent on source, frequency and model parameters (Malinowski et al., 2011). Therefore, we can increase the reliability and accuracy of seismic FWI results from the improved partial derivative wavefields by applying an optimal parameterization. This is because the other parameters are fixed and cannot be modified.

In this dissertation, a new parameterization is proposed to obtain accurate inversion results for 2-D elastic VTI media. The new parameterization is based on isotropic parameterization because it can provide better inversion results than the conventional VTI parameterization, although the anisotropic properties cannot be obtained. New anisotropic parameters are introduced instead of the conventional anisotropic parameters. To verify the effectiveness of the new parameterization, the scattering patterns of partial derivative wavefields with respect to model parameters and gradient directions are compared for a horizontal two-layered model, and the seismic FWI is applied to two types of bench-marking models.

Chapter 2. Theory

2.1 Transverse Isotropic Media

2.1.1 Linear elasticity of earth media

If a medium is linear elastic, the stress-strain relationship can be described by the generalized Hooke's law as follows:

$$\sigma_{ij} = C_{ijkl} \varepsilon_{kl}, \quad (2.1)$$

where σ_{ij} is a stress tensor, ε_{kl} is a strain tensor, and C_{ijkl} is a stiffness tensor. The stiffness tensor includes the stiffness coefficients for the linear stress-strain relationship, and indices i, j, k and l represent x, y and z . The stress and strain tensors have nine components in the 3-D case. Thus, the stiffness tensor has 81 components. Because of the symmetry of the stress and strain tensors ($\sigma_{ij} = \sigma_{ji}$, $\varepsilon_{kl} = \varepsilon_{lk}$), they are reduced to six components each, and the stiffness tensor is reduced to 36 components. If we define $xx = 1, yy = 2, zz = 3, yz = 4, xz = 5, xy = 6$ for simplicity, we can express the stress-strain relationship as:

$$\begin{pmatrix} \sigma_1 \\ \sigma_2 \\ \sigma_3 \\ \sigma_4 \\ \sigma_5 \\ \sigma_6 \end{pmatrix} = \begin{pmatrix} C_{11} & C_{12} & C_{13} & C_{14} & C_{15} & C_{16} \\ C_{21} & C_{22} & C_{23} & C_{24} & C_{25} & C_{26} \\ C_{31} & C_{32} & C_{33} & C_{34} & C_{35} & C_{36} \\ C_{41} & C_{42} & C_{43} & C_{44} & C_{45} & C_{46} \\ C_{51} & C_{52} & C_{53} & C_{54} & C_{55} & C_{56} \\ C_{61} & C_{62} & C_{63} & C_{64} & C_{65} & C_{66} \end{pmatrix} \begin{pmatrix} e_1 \\ e_2 \\ e_3 \\ 2e_4 \\ 2e_5 \\ 2e_6 \end{pmatrix}. \quad (2.2)$$

When orthotropic linear elastic materials are considered, the stiffness matrix can be expressed as

$$C = \begin{pmatrix} C_{11} & C_{12} & C_{13} & 0 & 0 & 0 \\ C_{21} & C_{22} & C_{23} & 0 & 0 & 0 \\ C_{31} & C_{32} & C_{33} & 0 & 0 & 0 \\ 0 & 0 & 0 & C_{44} & 0 & 0 \\ 0 & 0 & 0 & 0 & C_{55} & 0 \\ 0 & 0 & 0 & 0 & 0 & C_{66} \end{pmatrix}. \quad (2.3)$$

In the 2-D case (i.e. $y = 0$), the stiffness tensor can be expressed with four components as follows:

$$C = \begin{pmatrix} C_{11} & C_{13} & 0 \\ C_{13} & C_{33} & 0 \\ 0 & 0 & C_{44} \end{pmatrix}. \quad (2.4)$$

Therefore, there are four independent stiffness coefficients or elastic parameters for the 2-D elastic case.

2.1.2 Vertical transverse isotropic media

When the medium is assumed to be isotropic, the stiffness tensor can be expressed only by the Lamé constants, and C_{11} becomes equal to C_{33} , as shown below:

$$\begin{aligned}C_{11} &= C_{33} = \lambda + 2\mu, \\C_{13} &= \lambda, \\C_{44} &= \mu, \\V_P &= \sqrt{\frac{\lambda + 2\mu}{\rho}}, \\V_S &= \sqrt{\frac{\mu}{\rho}},\end{aligned}\tag{2.5}$$

where ρ is the density, and V_P and V_S are the P- and S-wave velocities of the isotropic media, respectively.

However, most subsurface materials are not isotropic. Thus, the stiffness coefficient cannot be expressed solely by the Lamé constants. Transverse isotropy is a symmetric system along the axis that describes the intrinsic characteristic of subsurface media. Vertical transverse isotropy (VTI) is the simplest version of transverse isotropy and is symmetric along the vertical axis of the materials (Figure 2.1). VTI is a commonly used assumption in seismic exploration because shale is a representative VTI rock that serves as a caprock for a reservoir or is the reservoir itself. Therefore, consideration of the VTI characteristics is important for inferring subsurface properties in seismic FWI.

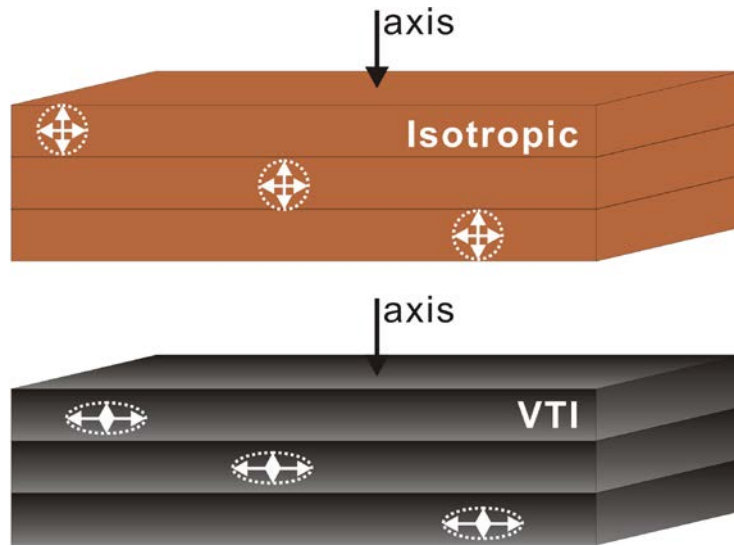


Figure 2.1 (upper) Isotropic and (lower) vertical transverse isotropic media.

Although elastic media are assumed to be isotropic in petroleum geophysics, most earth materials are characterized by anisotropic media due to the orientation of grains, the layering of sedimentary rocks and fracturing. The anisotropy affects both P- and S-wave velocities. In petroleum seismology, P-wave anisotropy is a more important characteristic than S-wave anisotropy because seismic surveys mainly address P-wave data (Linear, 2004). The anisotropy of subsurface media is quantified by seismic wave velocities with propagation angles (Daley and Hron, 1977). In order to quantify the degree of anisotropy, Thomsen (1986) proposed the Thomsen parameters (ϵ , δ and γ) to describe the anisotropic features based on the weak anisotropy assumption. These parameters are well suited for quantifying the effect of anisotropic characteristics of materials. In common layered rocks such as shale, the horizontal P-wave velocity is up to 20 % faster than vertical P-wave velocity. This means most rocks are weakly anisotropic, even though the minerals constituting them may be highly anisotropic (Linear, 2004; Thomsen, 1986). Thus, the weak anisotropy assumption is valid in seismic processing and interpretation (Tsvankin et al., 2010 Wang, 2006).

In anisotropic media, P- and S-wave velocities and Thomsen parameters can be expressed as follows:

$$\begin{aligned}
V_{p0} &= \sqrt{\frac{C_{33}}{\rho}}, \\
V_{s0} &= \sqrt{\frac{C_{44}}{\rho}}, \\
\varepsilon &= \frac{C_{11} - C_{33}}{2C_{33}}, \\
\delta &= \frac{(C_{13} + C_{44})^2 - (C_{33} - C_{44})^2}{2C_{33}(C_{33} - C_{44})}, \\
\gamma &= \frac{C_{66} - C_{44}}{2C_{44}},
\end{aligned} \tag{2.6}$$

where V_{p0} and V_{s0} are the P- and S-wave velocities along the vertical axis, respectively. In this relationship, ε represents the difference between the vertical and horizontal P-wave velocities, and γ describes the difference between vertical and horizontal S-wave velocities. The parameter δ represents the angular dependence of the P-wave velocity in the vicinity of the vertical axis (Ikelle and Amundsen, 2005). Therefore, ε and γ represent anisotropy of P- and S-wave velocities and determine the shape of the wavefronts of P- and S-waves, respectively. When δ has large negative values, the wavefront of an SV-wave is shaped like a square. The stiffness coefficients for 2-D VTI media can be expressed as follows:

$$\begin{aligned}
C_{33} &= \lambda + 2\mu, \\
C_{44} &= \mu, \\
C_{11} &= C_{33}(1 + 2\varepsilon), \\
C_{13} &= \sqrt{(C_{33} - C_{44})^2 + 2\delta C_{33}(C_{33} - C_{44})} - C_{44}.
\end{aligned} \tag{2.7}$$

If the subsurface media are weakly anisotropic, ε and δ are less than 0.2, and δ can be simplified as follows:

$$\delta = \frac{C_{13} - C_{33} + 2C_{44}}{C_{33}}. \quad (2.8)$$

Figure 2.2 shows P-wave velocity variations with increasing ε . When ε is zero, the P-wave velocity is the same in all propagation directions, whereas the horizontal P-wave velocity is up to 20 % faster than the vertical velocity when ε is 0.2.

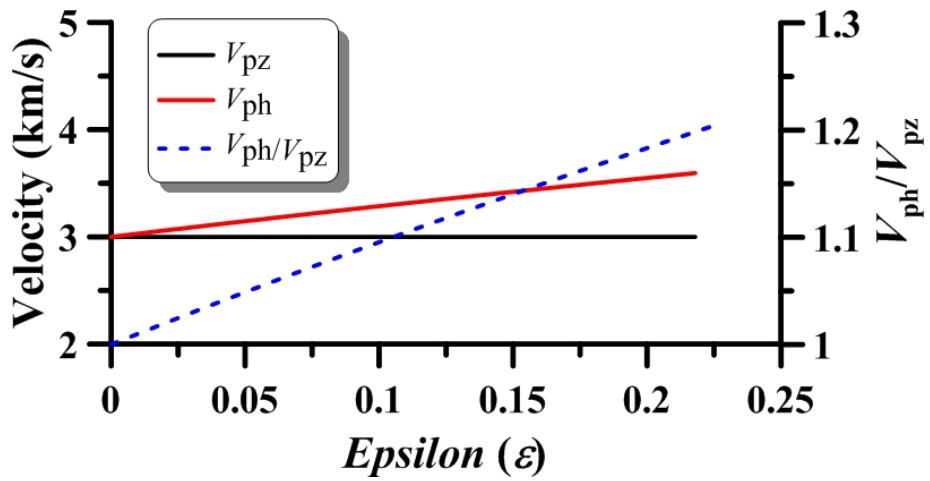


Figure 2.2 P-wave velocity variations with increasing ϵ : (black solid line) vertical P-wave velocity, (red solid line) horizontal P-wave velocity and (blue dashed line) ratio of horizontal and vertical P-wave velocities.

2.2 Forward Problems

2.2.1 Finite-element formula of the elastic wave equations

The equations of motion for 2-D elastic media can be written in the time domain as:

$$\begin{aligned}\rho \frac{\partial^2 u}{\partial t^2} &= \frac{\partial \sigma_{xx}}{\partial x} + \frac{\partial \sigma_{xz}}{\partial z}, \\ \rho \frac{\partial^2 v}{\partial t^2} &= \frac{\partial \sigma_{xz}}{\partial x} + \frac{\partial \sigma_{zz}}{\partial z},\end{aligned}\tag{2.9}$$

where u and v are the horizontal and vertical displacements, respectively. The strain is related to the particle displacement as follows:

$$e_{ij} = \frac{1}{2} \left(\frac{\partial u}{\partial z} + \frac{\partial v}{\partial x} \right),\tag{2.10}$$

where i and j represent x and z , respectively. Using this relationship, the displacement-based 2-D elastic wave equations can be expressed in the time domain as:

$$\begin{aligned}\rho \frac{\partial^2 u}{\partial t^2} &= \frac{\partial}{\partial x} \left[C_{11} \frac{\partial u}{\partial x} + C_{13} \frac{\partial v}{\partial z} \right] + \frac{\partial}{\partial z} \left[C_{44} \left(\frac{\partial u}{\partial z} + \frac{\partial v}{\partial x} \right) \right], \\ \rho \frac{\partial^2 v}{\partial t^2} &= \frac{\partial}{\partial z} \left[C_{33} \frac{\partial v}{\partial z} + C_{13} \frac{\partial u}{\partial x} \right] + \frac{\partial}{\partial x} \left[C_{44} \left(\frac{\partial u}{\partial z} + \frac{\partial v}{\partial x} \right) \right].\end{aligned}\tag{2.11}$$

In the isotropic case, we can express the elastic wave equations using only the Lamé constants as:

$$\begin{aligned}\rho \frac{\partial^2 u}{\partial t^2} &= \frac{\partial}{\partial x} \left[(\lambda + 2\mu) \frac{\partial u}{\partial x} + \lambda \frac{\partial v}{\partial z} \right] + \frac{\partial}{\partial z} \left[\mu \left(\frac{\partial u}{\partial z} + \frac{\partial v}{\partial x} \right) \right], \\ \rho \frac{\partial^2 v}{\partial t^2} &= \frac{\partial}{\partial z} \left[(\lambda + 2\mu) \frac{\partial v}{\partial z} + \lambda \frac{\partial u}{\partial x} \right] + \frac{\partial}{\partial x} \left[\mu \left(\frac{\partial u}{\partial z} + \frac{\partial v}{\partial x} \right) \right].\end{aligned}\tag{2.12}$$

In the VTI case, the elastic wave equations using the Lamé constants and Thomsen parameters can be written as follows:

$$\begin{aligned}\rho \frac{\partial^2 u}{\partial t^2} &= \frac{\partial}{\partial x} \left\{ [(\lambda + 2\mu)(1 + 2\varepsilon)] \frac{\partial u}{\partial x} + [(\lambda + 2\mu)(1 + \delta) - 2\mu] \frac{\partial v}{\partial z} \right\} \\ &\quad + \frac{\partial}{\partial z} \left\{ \mu \left(\frac{\partial u}{\partial z} + \frac{\partial v}{\partial x} \right) \right\}, \\ \rho \frac{\partial^2 v}{\partial t^2} &= \frac{\partial}{\partial z} \left[\lambda + 2\mu \right] \frac{\partial v}{\partial z} + [(\lambda + 2\mu)(1 + \delta) - 2\mu] \frac{\partial u}{\partial x} \\ &\quad + \frac{\partial}{\partial x} \left[\mu \left(\frac{\partial u}{\partial z} + \frac{\partial v}{\partial x} \right) \right].\end{aligned}\tag{2.13}$$

In this dissertation, we perform the elastic forward modeling in the frequency domain based on the 2-D elastic wave equations. In the frequency domain, the elastic wave equations can be expressed as:

$$\begin{aligned}
-\rho\omega^2\tilde{u} &= \frac{\partial}{\partial x} \left[C_{11} \frac{\partial\tilde{u}}{\partial x} + C_{13} \frac{\partial\tilde{v}}{\partial z} \right] + \frac{\partial}{\partial z} \left[C_{44} \left(\frac{\partial\tilde{u}}{\partial z} + \frac{\partial\tilde{v}}{\partial x} \right) \right], \\
-\rho\omega^2\tilde{v} &= \frac{\partial}{\partial z} \left[C_{33} \frac{\partial\tilde{v}}{\partial z} + C_{13} \frac{\partial\tilde{u}}{\partial x} \right] + \frac{\partial}{\partial x} \left[C_{44} \left(\frac{\partial\tilde{u}}{\partial z} + \frac{\partial\tilde{v}}{\partial x} \right) \right],
\end{aligned} \tag{2.14}$$

where \tilde{u} and \tilde{v} are the Fourier-transformed horizontal and vertical displacements, respectively, and ω represents the angular frequency.

In general, wave propagation can be simulated numerically using the finite-difference or the finite-element methods (Kelly et al., 1976; Marfurt, 1984; Virieux, 1986; Pratt, 1990). The finite-element method for seismic forward modeling is often based on the weighted residual method (Pinder and Gray, 1977; Zienkiewicz, 1977). The weighted residual method requires that the weighted average of given equation goes to zero in the domain Ω as follows:

$$\iint Lq d\Omega = 0, \tag{2.15}$$

where L is the linear differential equation, and q is the weighting function.

Thus, we obtain:

$$\begin{aligned}
\iint_{\Omega} \left[-\rho\omega^2\tilde{u} - \frac{\partial}{\partial x} \left(C_{11} \frac{\partial\tilde{u}}{\partial x} + C_{13} \frac{\partial\tilde{v}}{\partial z} \right) - \frac{\partial}{\partial z} \left(C_{44} \left(\frac{\partial\tilde{u}}{\partial z} + \frac{\partial\tilde{v}}{\partial x} \right) \right) \right] \tilde{q} dx dz, \\
\iint_{\Omega} \left[-\rho\omega^2\tilde{v} - \frac{\partial}{\partial z} \left(C_{33} \frac{\partial\tilde{v}}{\partial z} + C_{13} \frac{\partial\tilde{u}}{\partial x} \right) - \frac{\partial}{\partial x} \left(C_{44} \left(\frac{\partial\tilde{u}}{\partial z} + \frac{\partial\tilde{v}}{\partial x} \right) \right) \right] \tilde{q} dx dz.
\end{aligned} \tag{2.16}$$

By applying integration by parts (Zienkiewicz and Taylor, 2000) and considering the Neumann boundary conditions for surface boundaries, the weak form of the elastic wave equations can be obtained as:

$$\begin{aligned} \iint_{\Omega} \left[-\rho\omega^2 \tilde{u}\tilde{q} + \left(C_{11} \frac{\partial \tilde{u}}{\partial x} + C_{13} \frac{\partial \tilde{v}}{\partial z} \right) \frac{\partial \tilde{q}}{\partial x} + \left(C_{44} \left(\frac{\partial \tilde{u}}{\partial z} + \frac{\partial \tilde{v}}{\partial x} \right) \right) \frac{\partial \tilde{q}}{\partial z} \right] dx dz = 0, \\ \iint_{\Omega} \left[-\rho\omega^2 \tilde{v}\tilde{q} + \left(C_{33} \frac{\partial \tilde{v}}{\partial z} + C_{13} \frac{\partial \tilde{u}}{\partial x} \right) \frac{\partial \tilde{q}}{\partial z} + \left(C_{44} \left(\frac{\partial \tilde{u}}{\partial z} + \frac{\partial \tilde{v}}{\partial x} \right) \right) \frac{\partial \tilde{q}}{\partial x} \right] dx dz = 0. \end{aligned} \quad (2.17)$$

From the Galerkin method, we can deploy the basis function (ϕ) for the horizontal and vertical displacements as:

$$\begin{aligned} \iint_{\Omega} \left[-\rho\omega^2 \sum_{i=1}^N \tilde{u}_i \phi_i \sum_{j=1}^N \phi_j + \left\{ C_{11} \sum_{i=1}^N \tilde{u}_i \frac{\partial \phi_i}{\partial x} + C_{13} \sum_{i=1}^N \tilde{v}_i \frac{\partial \phi_i}{\partial z} \right\} \sum_{j=1}^N \frac{\partial \phi_j}{\partial x} \right. \\ \left. + \left\{ C_{44} \left(\sum_{i=1}^N \tilde{u}_i \frac{\partial \phi_i}{\partial z} + \sum_{i=1}^N \tilde{v}_i \frac{\partial \phi_i}{\partial x} \right) \right\} \sum_{j=1}^N \frac{\partial \phi_j}{\partial z} \right] dx dz = 0, \\ \iint_{\Omega} \left[-\rho\omega^2 \sum_{i=1}^N \tilde{v}_i \phi_i \sum_{j=1}^N \phi_j + \left\{ C_{33} \sum_{i=1}^N \tilde{v}_i \frac{\partial \phi_i}{\partial z} + C_{13} \sum_{i=1}^N \tilde{u}_i \frac{\partial \phi_i}{\partial x} \right\} \sum_{j=1}^N \frac{\partial \phi_j}{\partial z} \right. \\ \left. + \left\{ C_{44} \left(\sum_{i=1}^N \tilde{u}_i \frac{\partial \phi_i}{\partial z} + \sum_{i=1}^N \tilde{v}_i \frac{\partial \phi_i}{\partial x} \right) \right\} \sum_{j=1}^N \frac{\partial \phi_j}{\partial x} \right] dx dz = 0. \end{aligned} \quad (2.18)$$

From Eq. 2.18, seismic forward modeling can be performed. Eq. 2.18 can also be written in matrix form as:

$$\begin{bmatrix} \mathbf{M}_e + \mathbf{K}_e^{xx} & \mathbf{K}_e^{xz} \\ \mathbf{K}_e^{zx} & \mathbf{M}_e + \mathbf{K}_e^{zz} \end{bmatrix} \begin{bmatrix} \mathbf{u} \\ \mathbf{v} \end{bmatrix} = \begin{bmatrix} \mathbf{f}_h \\ \mathbf{f}_v \end{bmatrix}, \quad (2.19)$$

where

$$\mathbf{M}_e = \sum_{e=1}^{Ne} \iint_{\Omega} [-\rho\omega^2 \phi_i \phi_j] dx dz, \quad (2.20)$$

$$\mathbf{K}_e^{xx} = \sum_{e=1}^{Ne} \iint_{\Omega} \left[C_{11} \frac{\partial \phi_i}{\partial x} \frac{\partial \phi_j}{\partial x} + C_{44} \frac{\partial \phi_i}{\partial z} \frac{\partial \phi_j}{\partial z} \right] dx dz, \quad (2.21)$$

$$\mathbf{K}_e^{zz} = \sum_{e=1}^{Ne} \iint_{\Omega} \left[C_{33} \frac{\partial \phi_i}{\partial z} \frac{\partial \phi_j}{\partial z} + C_{44} \frac{\partial \phi_i}{\partial x} \frac{\partial \phi_j}{\partial x} \right] dx dz, \quad (2.22)$$

$$\mathbf{K}_e^{zz} = \sum_{e=1}^{Ne} \iint_{\Omega} \left[C_{13} \frac{\partial \phi_j}{\partial x} \frac{\partial \phi_i}{\partial z} + C_{44} \frac{\partial \phi_i}{\partial x} \frac{\partial \phi_j}{\partial z} \right] dx dz, \quad (2.23)$$

$$\mathbf{K}_e^{zz} = \sum_{e=1}^{Ne} \iint_{\Omega} \left[C_{13} \frac{\partial \phi_i}{\partial x} \frac{\partial \phi_j}{\partial z} + C_{44} \frac{\partial \phi_j}{\partial x} \frac{\partial \phi_i}{\partial z} \right] dx dz, \quad (2.24)$$

To decrease dispersion errors during numerical modeling, the eclectic method, i.e., linear combinations of the consistent and lumped mass matrices, is used (Marfurt, 1984) as follows:

$$\mathbf{M}_e^c = \frac{\Delta h^2}{36} \begin{bmatrix} 4 & 2 & 1 & 2 \\ 2 & 4 & 2 & 1 \\ 1 & 2 & 4 & 2 \\ 2 & 1 & 2 & 4 \end{bmatrix}, \quad (2.25)$$

$$\mathbf{M}'_e = \frac{\Delta h^2}{4} \begin{bmatrix} 1 & 0 & 0 & 0 \\ 0 & 1 & 0 & 0 \\ 0 & 0 & 1 & 0 \\ 0 & 0 & 0 & 1 \end{bmatrix}, \quad (2.26)$$

where \mathbf{M}_e^c and \mathbf{M}'_e are the consistent and lumped mass matrices, respectively, and Δh is the grid interval. We use 65 % of the consistent mass and 35 % of the lumped mass matrices.

2.2.2 PML boundary condition

In numerical simulations of seismic wave propagation, unwanted seismic wave reflections are generated at the artificial boundaries of a given model because of the limited model dimensions. Several techniques can be used to suppress these artificial reflections, including those proposed by Claytons and Engquist (1977), Reynolds (1978), Higdon (1986) and Shin (1995). In this dissertation, the boundary condition using the perfect matched layer (PML) proposed by Cohen (2002) is adopted. To apply the PML boundary condition, an additional zone is required for the PML layer (Figure 2.3). A damping coefficient is defined only at the PML zone. Thus, a damping function can be defined as:

$$\zeta_x = \begin{cases} 0 & x \in \text{Modeling zone} \\ \frac{3c_0}{2x_{PML}} \log(R) \left(\frac{x'}{x_{PML}} \right)^2 & x \in \text{PML zone} \end{cases}, \quad (2.27)$$

and

$$\zeta_z = \begin{cases} 0 & z \in \text{Modeling zone} \\ \frac{3c_0}{2z_{PML}} \log(R) \left(\frac{z'}{z_{PML}} \right)^2 & z \in \text{PML zone} \end{cases} . \quad (2.28)$$

Using Eqs. 2.27 and 2.28, artificial reflections are suppressed.

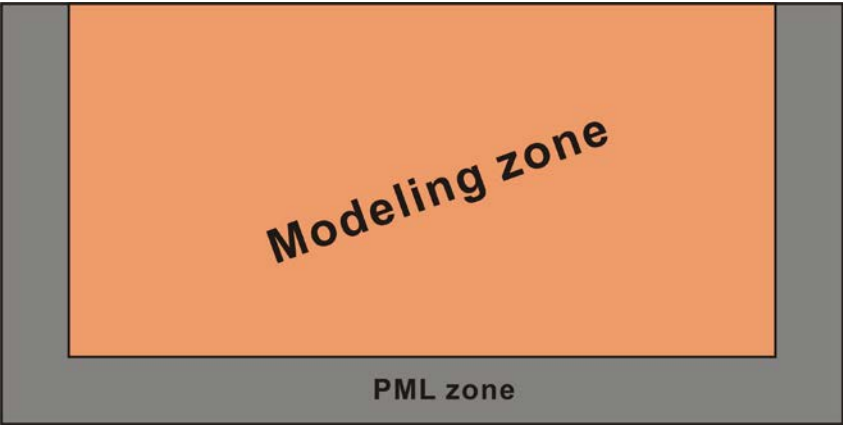


Figure 2.3 Model dimension with PML boundary zone.

2.2.3 Verification of the forward modeling algorithm

In general, a forward modeling algorithm is verified by comparing numerical solutions obtained by the forward modeling algorithm with analytical solutions obtained by solving Lamb's problem (Ewing et al, 1957; Pilant, 1979). Figure 2.4 shows a semi-infinite homogeneous model with a single source-receiver geometry. The offset between the source and the receiver positions is 1.5 km. The first derivative of the Gaussian function is used as a source. In this case, the Thomsen parameters are set to be zero to match the Lamb's problems, so the medium is assumed to be isotropic.

Figure 2.5 compares numerical and analytical solutions for the horizontal and vertical displacements. It can be seen that the numerical solutions obtained by the forward modeling algorithm agree well with the analytical solutions.

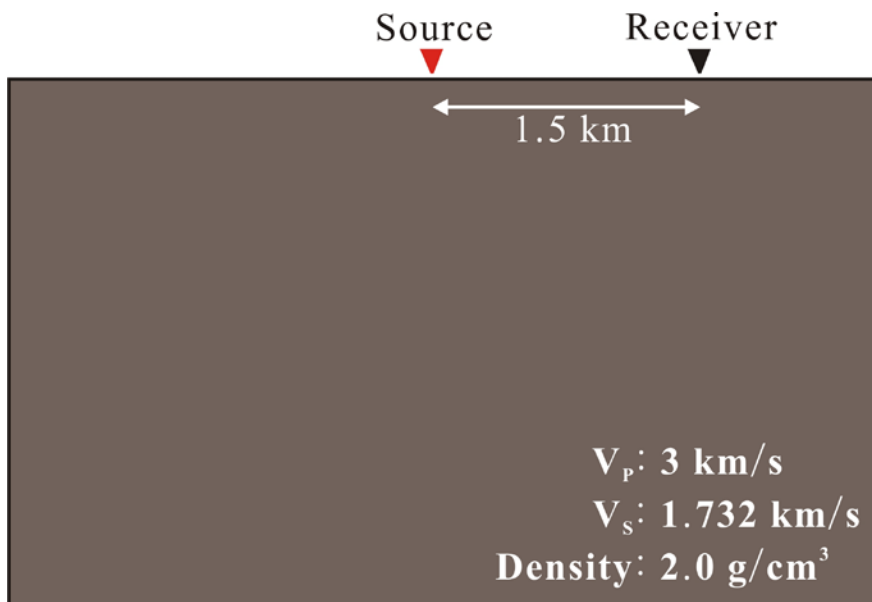


Figure 2.4 Homogeneous model with a single source-receiver geometry.

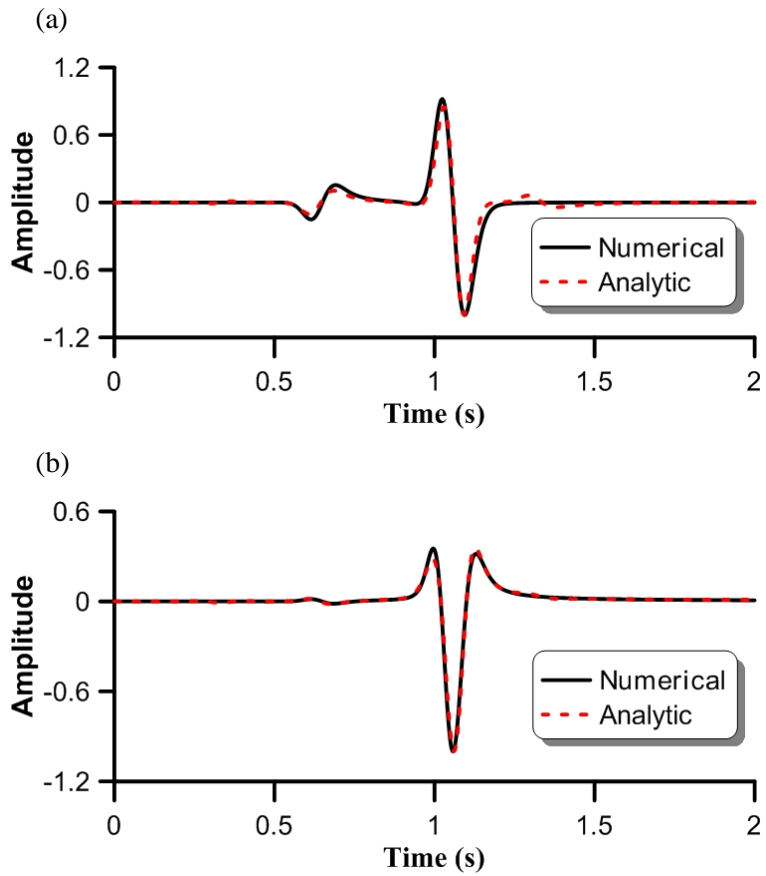


Figure 2.5 Comparison of analytic and numerical solutions for (a) horizontal and (b) vertical displacements. Black solid and red dashed lines represent numerical and analytic solutions, respectively.

The characteristics of seismic waves in anisotropic media are different from those in isotropic media, and the shape of the wavefront varies with the intensity of anisotropy. Figure 2.6 shows wavefronts for various values of ε , which represents the P-wave anisotropy. For this verification, it is assumed that the P-and S-wave velocities are 4 km/s and 2 km/s, respectively, and the density is 2 g/cm³. A source is located at the center of the model. When ε is zero, the wavefronts are isotropic in all directions. On the other hand, wavefronts at the perpendicular directions to the vertical symmetric axis are faster than those at the vicinity of the symmetric axis with increasing ε . In addition, the diamond-shaped wavefront develops when the medium is anisotropic due to the small value of δ .

It is well known that variations of the Thomsen parameters cause significant differences in the SV-wave (Ikelle and Amundsen, 2005). Figure 2.7 shows variations of wavefronts of SV-waves with respect to ε and δ . In this figure, the wavefront of the P-wave remains elliptical in all cases. When $\varepsilon - \delta \neq 0$, the wavefront of the SV-wave is rectangular. On the other hand, the SV-wave is maintained as isotropic when $\varepsilon - \delta = 0$.

Horizontal displacement

Vertical displacement

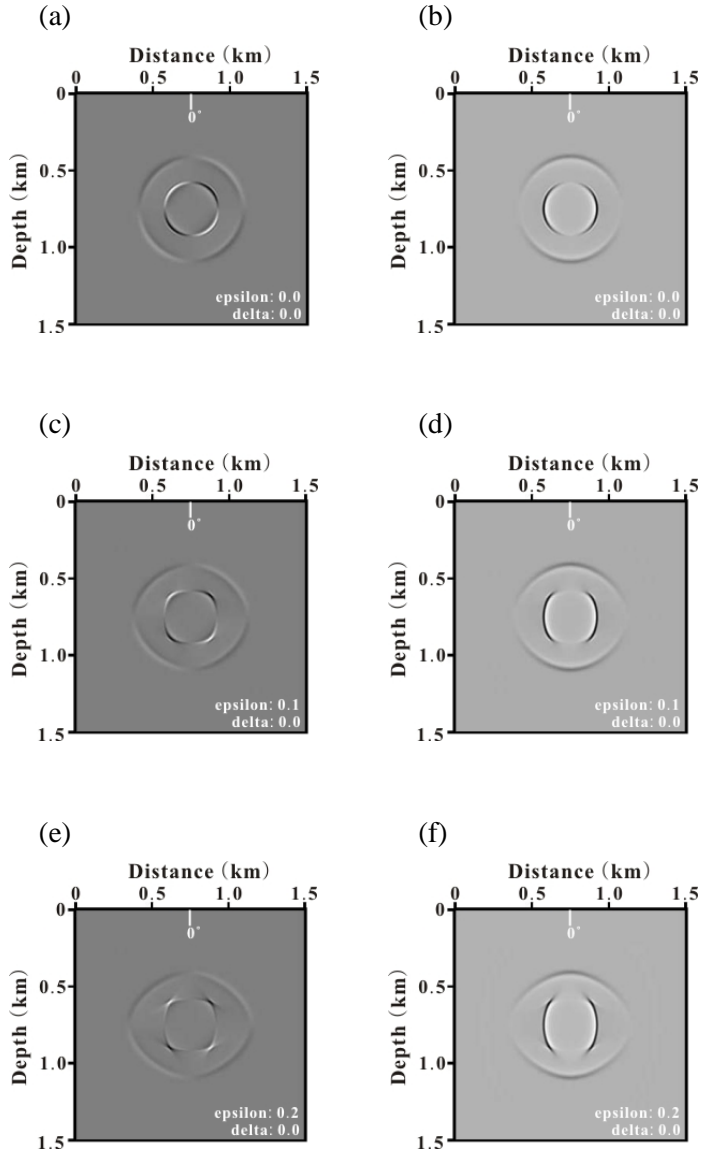


Figure 2.6 Snapshots of (a, c and e) horizontal and (b, d and f) vertical displacements at $t = 0.968$ s, when δ is fixed at 0.0.

Horizontal displacement

Vertical displacement

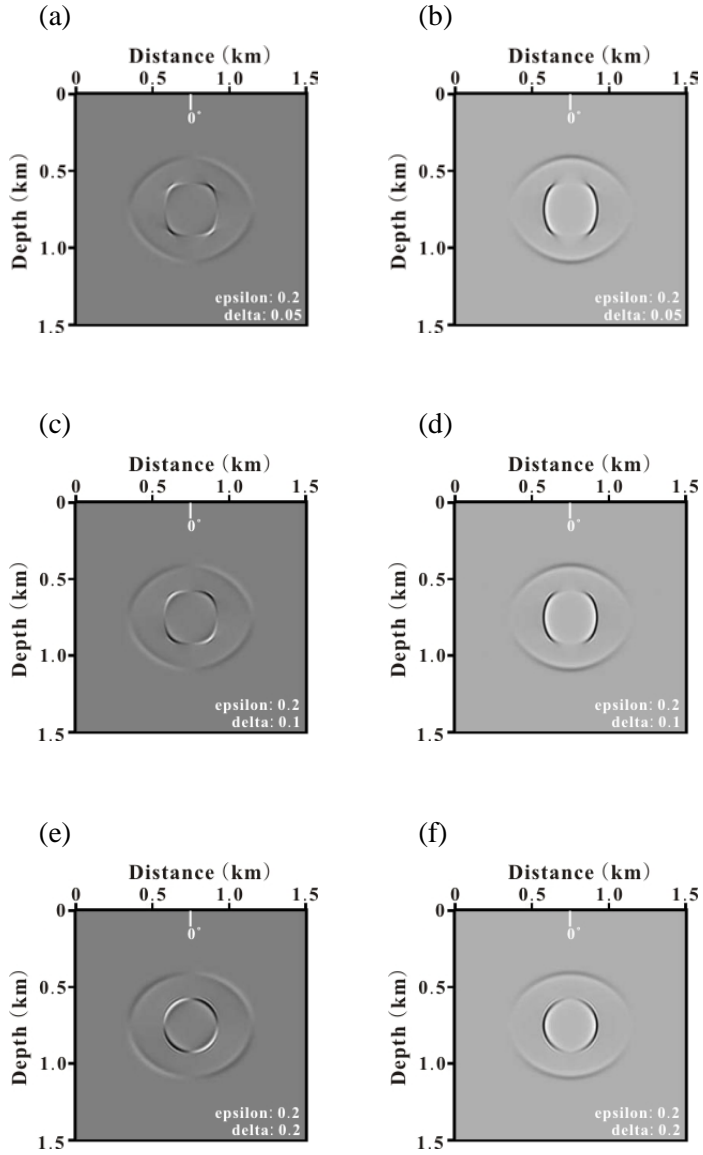


Figure 2.7 Snapshots of (a, c and e) horizontal and (b, d and f) vertical displacements at $t = 0.968$ s, when ϵ is fixed at 0.2.

2.3 Inverse Problems

Seismic FWI is performed using an iterative procedure to find the minimum error of the objective function. There are several objective functions for seismic FWI, such as l_1 -, l_2 - and Huber-norms. (Guitton and Symes, 2003; Pyun et al., 2009; Virieux and Operto, 2009). In this dissertation, the l_2 -norm-based objective function is used.

2.3.1 Seismic FWI using the l_2 -norm-based objective function

In the case of a single shot and a single frequency, for simplicity, the objective function based on the l_2 -norm can be written as:

$$E = \frac{1}{2} (\tilde{\mathbf{u}} - \tilde{\mathbf{d}})^T (\tilde{\mathbf{u}} - \tilde{\mathbf{d}})^*, \quad (2.29)$$

where $\tilde{\mathbf{u}}$ and $\tilde{\mathbf{d}}$ are the Fourier-transformed modeled and observed seismic data vectors, respectively, and the superscripts T and $*$ indicate the transpose and the complex conjugate, respectively. The gradient direction with respect to the model parameter m can be expressed using the backpropagation technique (Pratt et al., 1998) as:

$$\nabla_m E = \frac{\partial E}{\partial m} = \text{Re} \left\{ \left(\frac{\partial \tilde{\mathbf{u}}}{\partial m} \right)^T (\tilde{\mathbf{u}} - \tilde{\mathbf{d}})^* \right\} = \text{Re} \left\{ [\mathbf{f}]^T [\mathbf{S}^{-1}]^T (\tilde{\mathbf{u}} - \tilde{\mathbf{d}})^* \right\}, \quad (2.30)$$

where $\frac{\partial \tilde{\mathbf{u}}}{\partial m}$ is the partial derivative wavefield with respect to model parameter m , \mathbf{S} is the complex impedance matrix (modeling operator), and \mathbf{f} is the virtual source for model parameter m . The virtual source for model parameter m can be written as:

$$\mathbf{f} = -\frac{\partial \mathbf{S}}{\partial m} \mathbf{u}. \quad (2.31)$$

2.3.2 Preconditioned gradient direction

The subsurface model parameters are updated using the gradient direction of the objective function. In the full Newton and Gauss-Newton methods, the gradient direction is preconditioned by the full Hessian and approximate Hessian matrices (Pratt et al., 1998), respectively. However, it is difficult to compute the Hessian matrix because of the computational cost. In the quasi-Newton method, on the other hand, such as the limited-memory Broyden-Fletcher-Goldfarb-Shanno (L-BFGS) method, the inverse Hessian matrix is not computed directly, but the preconditioned gradient ($\delta m = -\mathbf{H}^{-1} \nabla_m E$) is computed using the gradient direction and model difference vector from the previous iterations (Nocedal and Wright, 1999; Brossier, 2011). An alternative preconditioning operator is the pseudo-Hessian matrix suggested by Shin et al. (2001). The pseudo-Hessian matrix is written as:

$$\mathbf{H}_{Pseudo} = (\mathbf{F})^T \mathbf{F}^*. \quad (2.32)$$

Although the pseudo-Hessian matrix cannot properly compensate for the geometrical spreading effect, it provides computational efficiency and convenience. The model parameter m is updated in the i th iteration as follows:

$$\mathbf{m}^{i+1} = \mathbf{m}^i - \alpha \left(\mathbf{H}_{Pseudo}^i + \lambda \mathbf{I} \right)^{-1} \nabla_m E, \quad (2.33)$$

where α is a step length, \mathbf{H}_{Pseudo}^i is the pseudo-Hessian matrix for the parameter m , \mathbf{I} is the identity matrix and λ is a damping factor for the Marquardt-Levenverg method (Lines and Treitel, 1984).

2.3.3 Conjugate gradient method and Source wavelet estimation

To increase the convergence rate, the conjugate gradient method is applied during the FWI process (Fletcher and Reeves, 1964). The conjugate gradient direction can be expressed as:

$$\mathbf{g}^i = -\nabla E^i + \beta^i \mathbf{g}^{i-1}, \quad (2.34)$$

where the superscript i represents the iteration number, and β^i is defined as:

$$\beta^i = \frac{(\nabla_m E^i)^T \nabla_m E^i}{(\nabla_m E^{i-1})^T \nabla_m E^{i-1}}. \quad (2.35)$$

Thus, equation (2. 33) can be changed as follows:

$$\mathbf{m}^{i+1} = \mathbf{m}^i + \alpha g^i. \quad (2.36)$$

The source wavelet is an important factor for successful seismic FWI. However, because the actual source wavelet is unknown in real data, it is necessary to estimate the source wavelet during the FWI process. In this dissertation, the source wavelet is estimated using the Newton method in the frequency domain (Pratt, 1999; Shin and Min, 2006; Shin et al., 2007). The source wavelet is updated using:

$$\begin{aligned} e^{i+1} &= \frac{\sum_j (a_j c_j + b_j d_j)}{\sum_j (c_j^2 + d_j^2)}, \\ f^{i+1} &= \frac{\sum_j (a_j d_j + b_j c_j)}{\sum_j (c_j^2 + d_j^2)}, \end{aligned} \quad (2.37)$$

where e and f are the real and imaginary parts of source wavelet, respectively,

a and b are the real and imaginary parts of observed data, respectively, and c and d are the real and imaginary parts of the numerical green's function, respectively.

Chapter 3. New Parameterization

3.1 Former studies on seismic FWI for VTI media

Multi-parametric inversion algorithms suffer from nonlinearity, meaning that they can become stuck in local minima as the number of parameters increases (Figure 3.1). In general, three parameters, such as P-wave velocity, S-wave velocity and density or the Lamé constants (λ and μ) and density, are inverted during seismic FWI for isotropic elastic media. Unfortunately, the numbers of inverted parameters increases when the anisotropic characteristics such as C_{11} and C_{13} or the Thomsen parameters are considered. Eventually, the probability of becoming trapped in local minima becomes higher than in the isotropic case (Virieux and Operto, 2009).

In seismic FWI, the sequential inversion strategies and parameterizations have been used to overcome the weakness of multi-parametric inversion. Since Tarantola (1986) suggested a sequential inversion strategy for the isotropic elastic FWI by analyzing the scattering patterns of parameters, various sequential inversion strategies have been developed, and several parameterizations have been proposed to obtain density, attenuation factor and anisotropic parameters in addition to velocities. However, the FWI for anisotropic properties remains difficult due to the multi-parametric inversion problems and different characteristics and sensitivities of seismic data. Gholami et al. (2013) developed a parameterization based on the pseudo-acoustic wave equations. In their strategy, the vertical P-wave velocity is

inverted with the constant Thomsen parameters because the inversion process is not sensitive to the Thomsen parameters. This is because the scattering patterns of the partial derivative wavefields with respect to the Thomsen parameters are not dominant compared to those of the P-wave velocity. They also showed that the joint inversion of vertical and horizontal P-wave velocities with a fixed δ provides reliable inversion results because the influence of δ on the seismic data is not strong. Koo et al. (2010) and Lee et al. (2010) studied seismic FWI based on full elastic wave equations using multi-component data. Koo et al. (2010) suggested a sequential inversion strategy that uses isotropic and VTI inversion algorithms. In this strategy, the parameters (C_{33} and C_{44}), expressed only by the Lamé constants, are inverted using the isotropic inversion algorithm in the first inversion stage, and all the elastic parameters (C_{11} , C_{13} , C_{33} and C_{44}) are inverted using the VTI inversion algorithm in the second stage. Lee et al. (2010) developed a coupling method to improve C_{11} by modifying the virtual source for C_{11} and then improved C_{13} by performing additional inversion using the inversion results obtained in the first stage as the initial models. In most sequential inversion strategies, the parameters that are inverted well and have a strong influence on seismic data are inverted first. In the second stage, the other parameters are inverted using the inversion results of the first stage. This strategy provides good inversion results regardless of the inversion settings. This means that the parameters that are inverted first can positively influence the other parameters during the inversion. In this dissertation, we will call the parameters having a strong influence on data the primary parameters, and the other parameters are called

secondary parameters. In the acoustic case, the P-wave velocity or bulk modulus can be the primary parameters, and the P- and S-wave velocities or the Lamé constants can be the primary parameters in the elastic case. In the case of 2-D elastic VTI media, C_{33} and C_{44} can be the primary parameters because they are directly related to vertical P-wave velocity and S-wave velocity, respectively. However, despite the application of sequential inversion strategies, the inversion results for elastic VTI media still require improvement. In particular, it is still difficult to obtain reliable inversion results for anisotropic properties such as C_{11} and C_{13} or the Thomsen parameters. Furthermore, the sequential strategies require additional computational effort when dealing with large amount of seismic data, such as 2-D wide-angle and 3-D data.

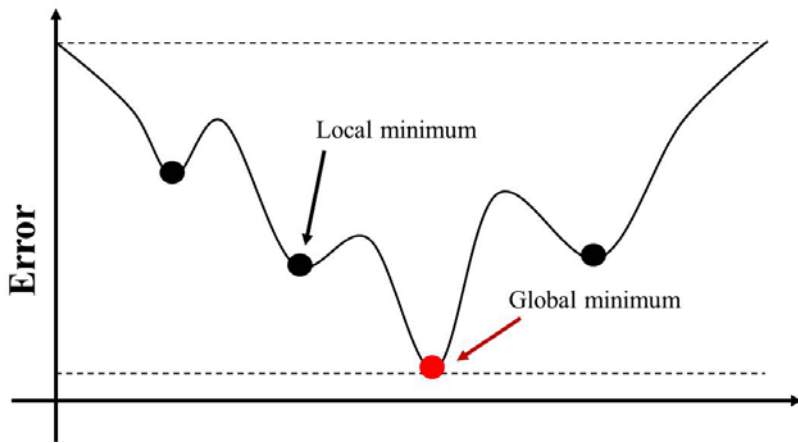


Figure 3.1 Global and local minimum points.

3.2 New Parameterization

It is well known that isotropic inversion can provide good inversion results, although subsurface media are anisotropic. Based on this capability, we propose a new parameterization for 2-D elastic VTI media based on the isotropic parameterization.

The general form of elastic wave equations in the frequency domain (Eq. 2.14) contains four elastic parameters (C_{11} , C_{13} , C_{33} and C_{44}). When the medium is isotropic, as described in Chapter 2, C_{11} is the same as C_{33} , and all the parameters can be expressed only by the Lamé constants. This means there are only three inverted parameters. In the VTI case, however, four parameters are independent and should be inverted individually. In the wave equations, the primary parameters (C_{33} and C_{44}) for the VTI case have fewer spatial derivative terms than the Lamé constants in the isotropic case, which may decrease the resolution of inversion for the primary parameters. Because the parameters are interdependent during the inversion, the resolution of inversion for the secondary parameters may also be decreased. Therefore, a new parameterization is required to overcome this problem.

As shown in Eq. 2.7, C_{33} and C_{44} can be expressed only by the Lamé constants in isotropic and anisotropic media. If the medium is weakly anisotropic, C_{13} can be simplified as follows (Ikelle and Amundsen, 2005):

$$C_{13} = C_{33}(1 + \delta) - 2C_{44}. \quad (3.1)$$

Thus, the elastic parameters for VTI media can be represented by the Lamé constants and new parameters as follows:

$$\begin{aligned}
C_{11} &= \lambda + 2\mu + \xi_1, \\
C_{13} &= \lambda + \xi_2, \\
C_{33} &= \lambda + 2\mu, \\
C_{44} &= \mu,
\end{aligned} \tag{3.2}$$

where the parameters ξ_1 and ξ_2 can be expressed as:

$$\begin{aligned}
\xi_1 &= 2\varepsilon(\lambda + 2\mu), \\
\xi_2 &= \delta(\lambda + 2\mu).
\end{aligned} \tag{3.3}$$

In Eqs. 3.2 and 3.3, the anisotropic properties of the subsurface media are described by ξ_1 and ξ_2 . Using the Lamé constants and new parameters, the elastic wave equations for 2-D VTI media can be written as:

$$\begin{aligned}
-\rho\omega^2\tilde{u} &= \frac{\partial}{\partial x} \left[(\lambda + 2\mu + \xi_1) \frac{\partial \tilde{u}}{\partial x} + (\lambda + \xi_2) \frac{\partial \tilde{v}}{\partial z} \right] + \frac{\partial}{\partial z} \left[\mu \left(\frac{\partial \tilde{u}}{\partial z} + \frac{\partial \tilde{v}}{\partial x} \right) \right], \\
-\rho\omega^2\tilde{v} &= \frac{\partial}{\partial z} \left[(\lambda + 2\mu) \frac{\partial \tilde{v}}{\partial z} + (\lambda + \xi_2) \frac{\partial \tilde{u}}{\partial x} \right] + \frac{\partial}{\partial x} \left[\mu \left(\frac{\partial \tilde{u}}{\partial z} + \frac{\partial \tilde{v}}{\partial x} \right) \right].
\end{aligned} \tag{3.4}$$

In Eq. 3.4, the Lamé constants (λ and μ) are the primary parameters, and the new parameters (ξ_1 and ξ_2) and density are the secondary parameters. A

comparison of Eq.3.4 with the elastic wave equations for isotropic media shows that the Lamé constants are multiplied by the same derivatives as in the isotropic case. Thus, the new parameterization can preserve the characteristics of the isotropic parameterization. In addition, these characteristics cause the Lamé constants to have different characteristics from C_{33} and C_{44} for VTI media. On the other hand, ξ_1 and ξ_2 are multiplied by the same derivatives that are used for C_{11} and C_{13} . Thus, the new parameters for anisotropic properties can preserve the characteristics of C_{11} and C_{13} during the inversion, and C_{11} , C_{13} , C_{33} and C_{44} for VTI media are obtained from the inverted Lamé constants and the new parameters. Figure 3.2 shows the workflow of seismic FWI with the new parameterization.

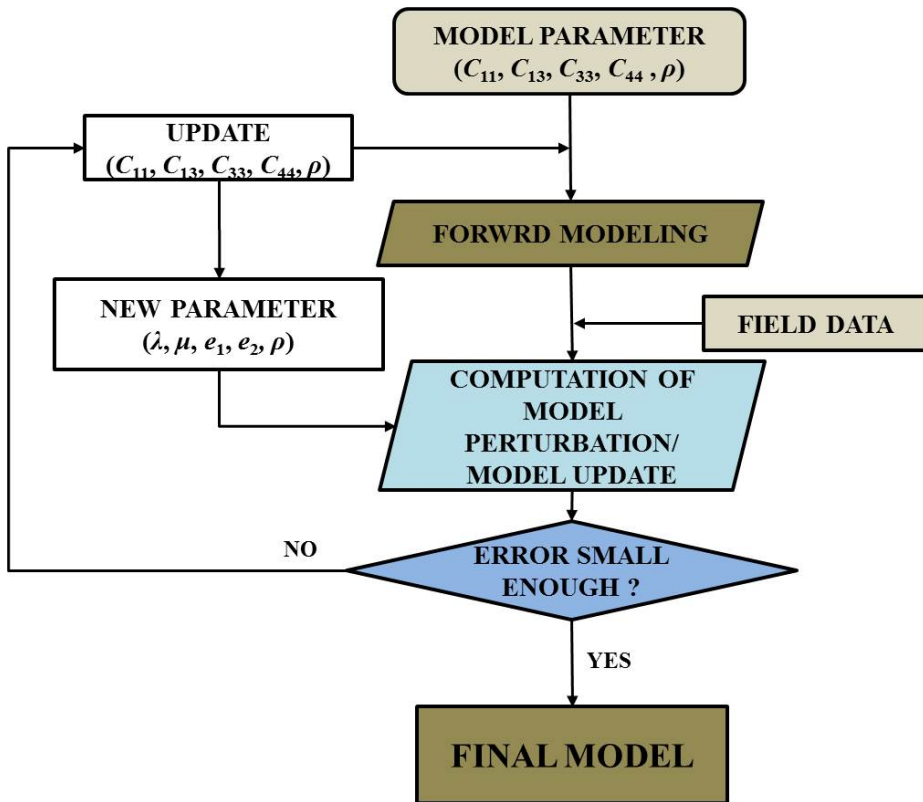


Figure 3.2 Workflow of the seismic FWI using the new parameterization.

3.3 Sensitivity Analysis

3.3.1 Scattering patterns of partial derivative wavefields

Many studies have shown that analyzing the scattering patterns of partial derivative wavefields provides insight into the sensitivity of parameters for scattering angles, which helps us develop an inversion strategy (Gholami et al., 2013; Prioux et al., 2013; Tarantola, 1986). By investigating the scattering patterns of partial derivative wavefields with respect to model parameters, we can estimate the offset-dependency of each parameter and the trade-off between parameters in the inversion. When the scattering pattern of a given parameter is uniformly distributed over a wide range of angles, the influence of the parameter on data is less dependent on the offset. In contrast, inversion of the parameter is offset-dependent when the scattering pattern is concentrated at specific angles (Gholami et al., 2010; Prioux et al., 2013; Tarantola, 1986; Virieux and Operto, 2009).

Because partial derivative wavefields with respect to model parameters are dependent on parameterization, the new parameterization yields different features of the partial derivative wavefields of each parameter. Because the scattering patterns of partial derivative wavefields are related to the virtual source in Eq. 2.31, the use of different derivatives generates different scattering patterns. The partial derivative wavefield with respect to the model parameter m can be easily obtained using the virtual source for the model parameter m as below:

$$\frac{\partial \mathbf{u}}{\partial m} = \mathbf{S}^{-1} \mathbf{F}^m, \quad (3.5)$$

Using Eq. 3.5, the partial derivative wavefield with respect to each model parameter is computed and compared. Modeled wavefields are obtained for a homogenous model assuming ideal acquisition geometry in which sources and receivers are located at whole grid points of the surface. The maximum frequency of the source is 20 Hz. The virtual source is placed at the central grid point of the model to generate the partial derivative wavefields. Table 3.1 shows the material properties of the model.

Table 3.1 Elastic properties used to obtain partial derivative wavefields with respect to model parameters.

Parameter	C_{11} (Gpa)	C_{13} (Gpa)	C_{33} (Gpa)	C_{44} (Gpa)	ρ (g/cm ³)	ξ_1 (Gpa)	ξ_2 (Gpa)	λ (Gpa)	μ (Gpa)
Isotropic	19.44	6.48	19.44	6.48	2.16	-	-	6.48	6.48
VTI	27.22	8.424	19.44	6.48	2.16	3.00	3.55	6.48	6.48

Figures 3.3 and 3.4 show the scattering patterns of the horizontal and vertical components of the partial derivative wavefields obtained using the conventional isotropic and VTI parameterizations. These are comprehensive scattering patterns of diffracted wave components obtained by the combination of all of the scattered waves, such as P-P, P-S, S-P and S-S waves. The scattering patterns for the primary parameters by the isotropic parameterization are different from those of the conventional VTI parameterization. In the case of isotropic parameterization, the scattered energies of λ and μ are widely distributed over the wide angles with strong amplitudes. The scattering pattern of C_{33} in the conventional VTI parameterization (Figures 3.4e and 3.4f) shows a similar pattern to that of μ in the isotropic parameterization (Figures 3.3c and 3.3d), whereas the scattering pattern of C_{44} is concentrated at several specific angles with relatively small amplitudes. These features indicate that inversion result for C_{44} is worse than that for μ in the isotropic parameterization, even though C_{44} is the primary parameter. The scattering patterns of density (ρ) in both parameterizations are very similar. This indicates that the success of density inversion is dependent on the inversion results for the other parameters.

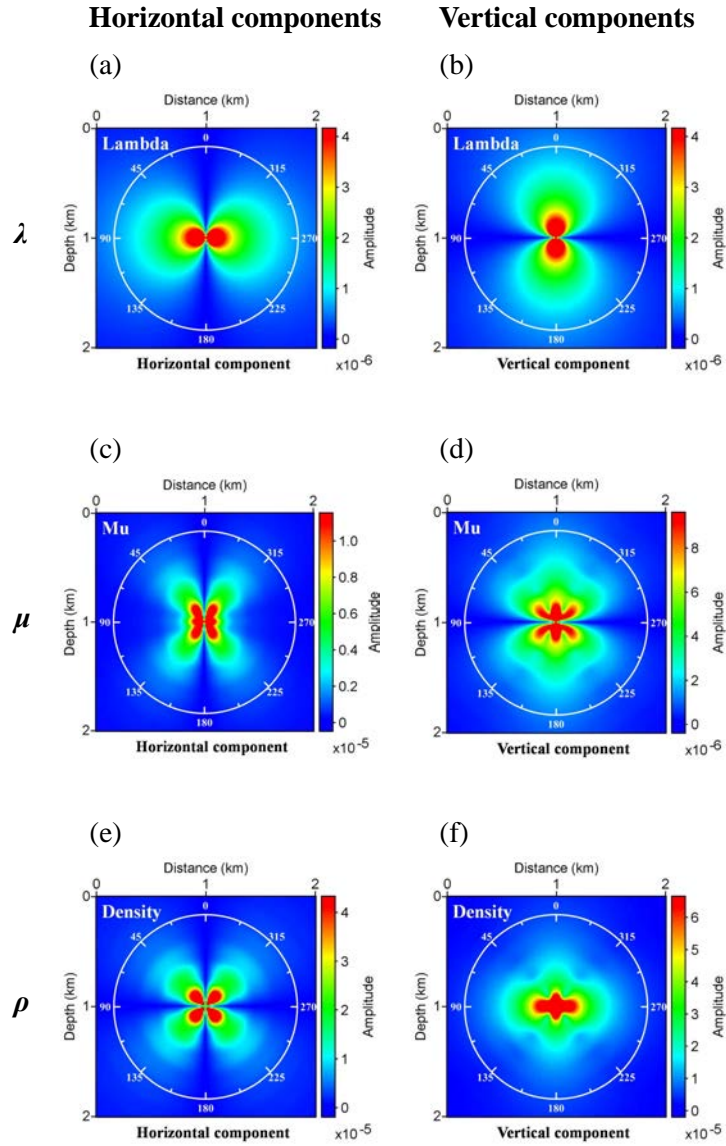


Figure 3.3 Scattering patterns of horizontal (left) and vertical (right) components of partial derivative wavefields with respect to λ (a and b), μ (c and d) and ρ (e and f) for the isotropic parameterization.

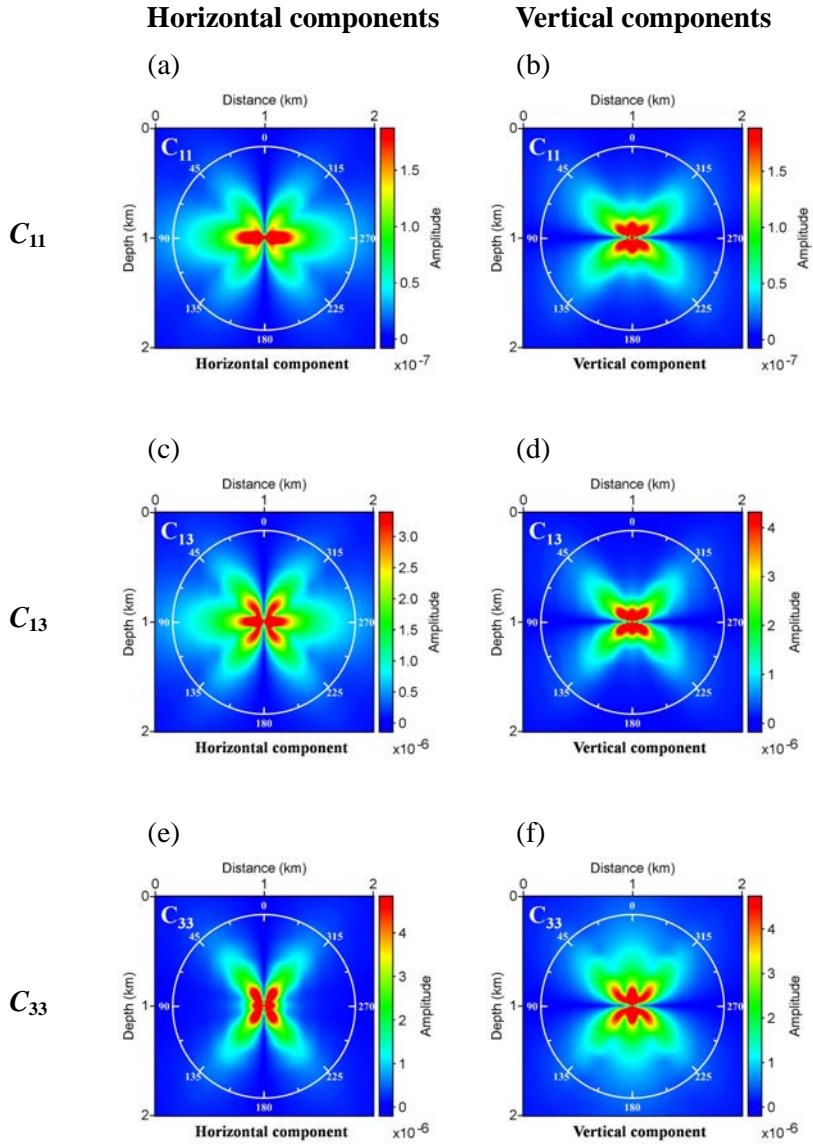


Figure 3.4 Scattering patterns of horizontal (left) and vertical (right) components of partial derivative wavefields with respect to C_{11} (a and b), C_{13} (c and d), C_{33} (e and f), C_{44} (g and h) and ρ (i and j) for the conventional VTI parameterization.

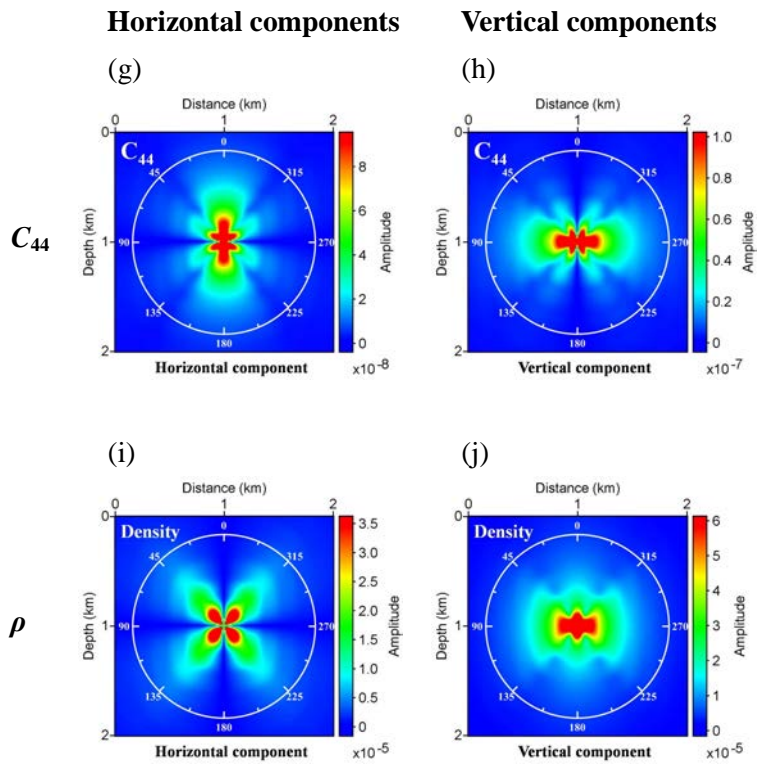


Figure 3.4 (Continued)

Figure 3.5 shows the scattering patterns of the Lamé constant, the new parameters and density when the new parameterization is applied for VTI media. The scattering patterns of λ and μ (Figure 3.5) are similar to those in the isotropic case (Figure 3.3). Small differences are observed for different modeling. The results indicate that the Lamé constants obtained by applying the new parameterization to VTI media are as good as those obtained using the isotropic inversion. In the case of anisotropic parameters (C_{11} and C_{13} in Figure 3.4 and ξ_1 and ξ_2 in Figure 3.5), the scattering patterns of ξ_1 and ξ_2 are the same as those of C_{11} and C_{13} , respectively; this is because they are related to the same spatial derivatives in the elastic wave equations. Thus, the new parameterization maintains the characteristics and resolutions of C_{11} and C_{13} in the conventional parameterization. C_{11} and C_{13} are not inverted well; thus, ξ_1 and ξ_2 are not recovered well. However, better inversion results for the anisotropic parameters are expected using the new parameterization because the improved Lamé constants positively affect the anisotropic parameter. In the case of density, different scattering patterns cannot be identified because the virtual source for density is not modified by the new parameterization. Thus, improvement of the inversion result for density is not expected. However, we can obtain improved inversion results for density if the other parameters are improved by the new parameterization.

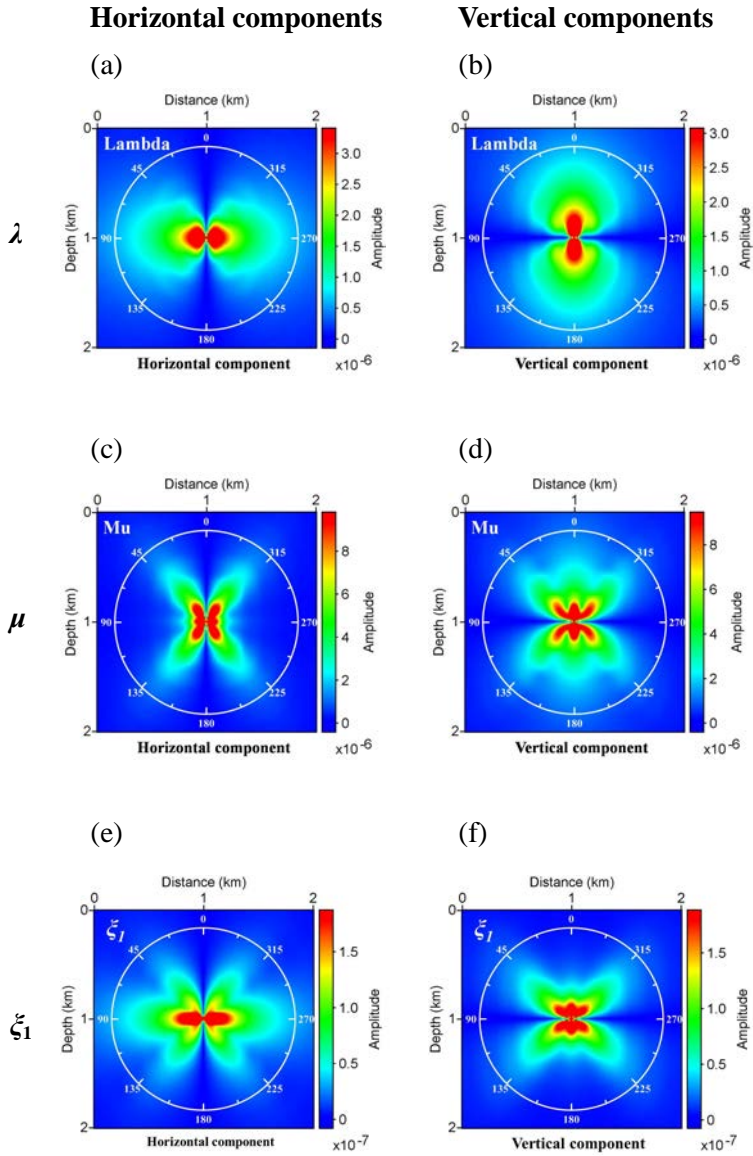


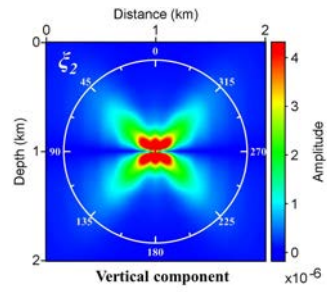
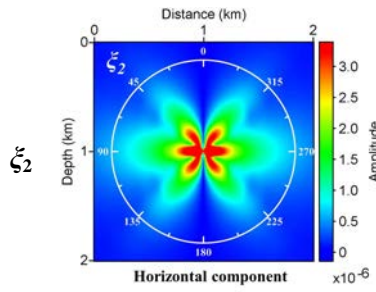
Figure 3.5 Scattering patterns of horizontal (left) and vertical (right) components of partial derivative wavefields with respect to λ (a and b), μ (c and d), ξ_1 (e and f), ξ_2 (g and h) and ρ (i and j) for the conventional VTI parameterization.

Horizontal components

Vertical components

(a)

(b)



(c)

(d)

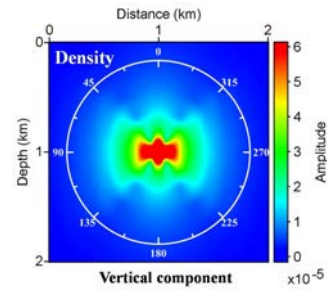
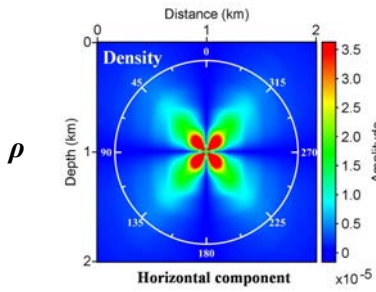


Figure 3.5 (Continued)

3.3.2 Comparisons of gradient directions

To directly investigate the effectiveness of the new parameterization, the gradient directions in the first iteration obtained by the conventional VTI parameterization were compared with those obtained by the new parameterization for the horizontal two-layered model (Figure 3.6). Seismic data were acquired through an ideal survey acquisition in which receivers are placed on whole surface stations at intervals of 10 m, and the source interval is 50 m. The maximum frequency of the source is 15 Hz. The material properties of the medium are described in Table 3.2.

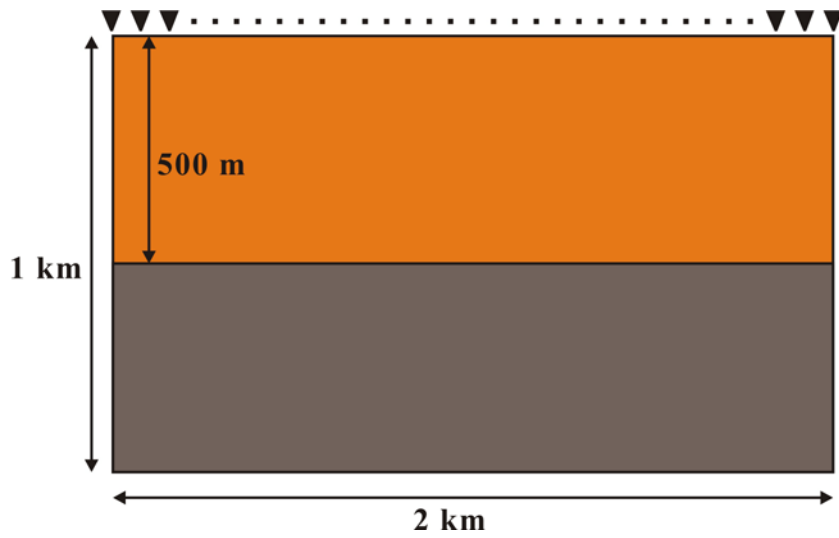


Figure 3.6 Horizontal two-layered model and seismic survey geometry used to obtain gradient directions.

Table 3.2 Elastic properties of the simple two-layered model for the computation of gradient directions.

Parameter	C_{11} (Gpa)	C_{13} (Gpa)	C_{33} (Gpa)	C_{44} (Gpa)	ρ (g/cm ³)
Layer 1	12.10	3.74	8.64	2.88	2.16
Layer 2	27.22	8.42	19.44	6.48	2.16

Figures 3.7 and 3.8 show normalized gradient directions in the first iteration for the conventional and new parameterizations. The normalized gradient directions of ξ_1 and ξ_2 obtained by the new parameterization (Figures 3.8a and 3.8b) are the same as those of C_{11} and C_{13} obtained by the conventional VTI parameterization (Figures 3.7a and 3.7b), respectively. This indicates that the new parameterization can recover the anisotropic properties as effectively as the conventional parameterization, and it matches well with the scattering patterns of partial derivative wavefields.

Figures 3.7c and 3.8c represent the normalized gradient directions of C_{33} and λ after the first iteration. The gradient directions do not represent the same subsurface properties. However, C_{33} and λ are compared because they are closely related to P-wave velocity. The gradient direction sections for λ and C_{33} show similar resolutions, which indicates that the inversion results for λ obtained by the new parameterization are comparable to those of C_{33} obtained by the conventional VTI parameterization. Figure 3.7d shows that the resolution of the gradient direction of C_{44} is not as good as that of C_{33} , although C_{44} is regarded as a primary parameter in the conventional VTI parameterization. On the other hand, the resolution of μ in the new parameterization is similar to that of λ , and the resolution of μ is improved compared to that of C_{44} in the conventional parameterization. These results also match well the analysis of the scattering patterns of partial derivative wavefields. These comparisons indicate that the new parameterization can improve inversion results for the primary parameters (particularly μ) compared to the conventional VTI parameterization.

Figure 3.9 shows the depth logs at distances of 1 km, 1.3 km and 1.7 km. In all the depth logs, the same resolution of anisotropic parameters (C_{11} , C_{13} , ξ_1 and ξ_2) and a compatible resolution of λ with C_{33} are observed. In addition, an improvement in the gradient direction for μ in the new parameterization can be clearly seen. Therefore, the new parameterization can improve the inversion results of the primary parameters (λ and μ or C_{33} and C_{44}) compared to those obtained by the conventional VTI parameterization.

In the new parameterization, the new parameters (ξ_1 and ξ_2) are not directly improved, but we expect that improved inversion results of the anisotropic parameters would be obtained because the improved primary parameters positively affect the anisotropic parameters during the inversion. We also expect improvements in the density because of the improvements of the other parameters.

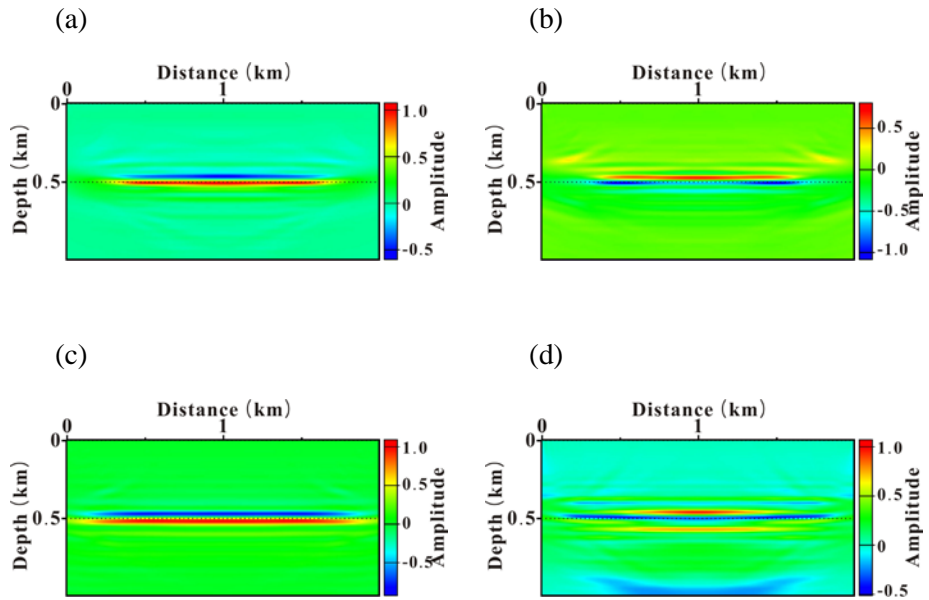


Figure 3.7 Normalized gradient directions in the first iteration for the simple two-layered model obtained by the conventional VTI parameterization: (a) C_{11} , (b) C_{13} , (c) C_{33} and (d) C_{44} .

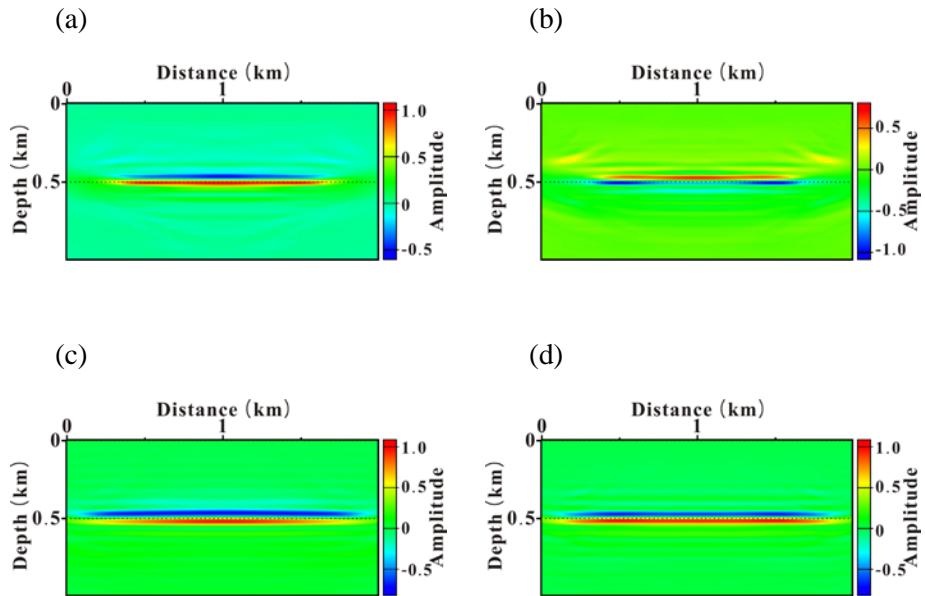


Figure 3.8 Normalized gradient directions in the first iteration for the simple two-layered model obtained by the new parameterization: (a) ξ_1 , (b) ξ_2 , (c) λ and (d) μ .

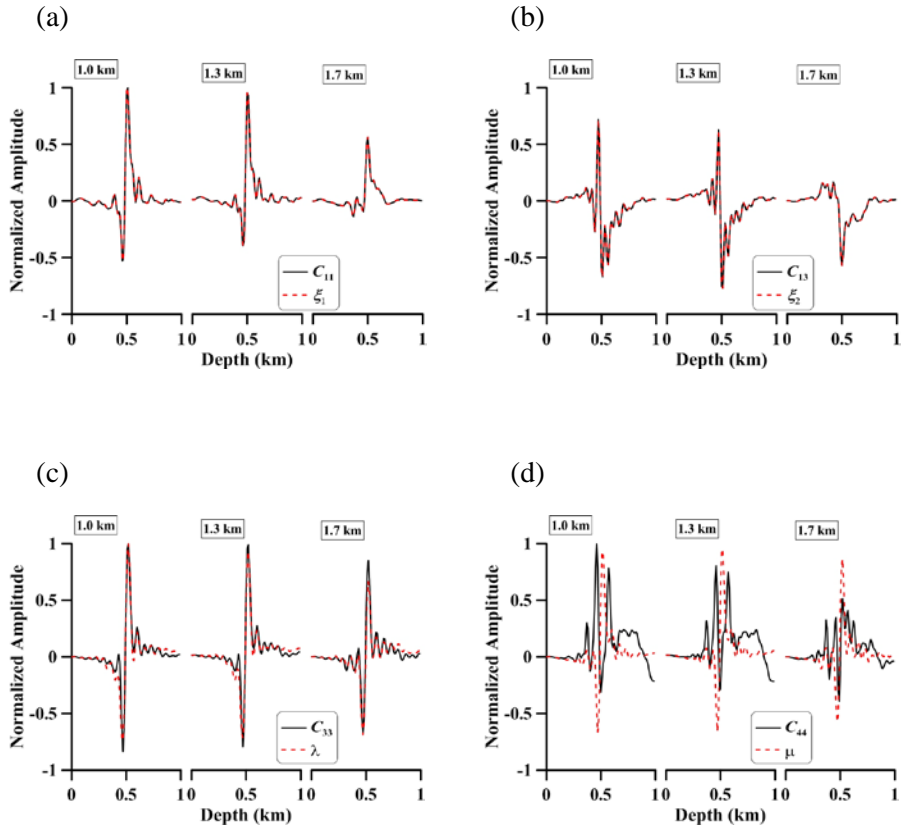


Figure 3.9 Amplitude logs of the normalized gradient directions with respect to each parameter obtained by (black solid lines) the conventional and (red dashed lines) new parameterizations for VTI media: (a) C_{11} and ξ_1 , (b) C_{13} and ξ_2 , (c) C_{33} and λ and (d) C_{44} and μ . The logs are extracted at distances of (left) 1.0 km, (center) 1.3 km and (right) 1.7 km, respectively.

Chapter 4. Synthetic Examples

To verify the improvements of the inversion results for VTI media by the new parameterization, numerical inversion with the new parameterization is performed for two VTI bench-marking models with complicated subsurface media. One is the SEG/EAGE overthrust model, which is characterized by an overthrust fault with anisotropy. The second model is the SEG/HESS model, which contains a salt body characterized by high velocities and low density. The sequential inversion is performed for comparison.

4.1 The SEG/EAGE Overthrust Model

4.1.1 Modified version of the overthrust model

Figure 4.1 shows the modified version of the overthrust models distributed by Delft University (<http://aniso.citg.tudelft.nl>). The models are mainly characterized by anticlines and overthrust faults. In this case, the Poisson's ratio is assumed to be constant at 0.25 for the entire model in order to identify the effectiveness of the new parameterization. Lee et al. (2010) used a similar model assuming a constant density of 2.16 g/cm^3 . However, the density is a critical factor for characterizing subsurface media. For this reason, the density was varied in this study. To maintain the simplicity of the inversion, a regenerated density model based on Gardner's relationship (Gardner et al., 1974) was used. The model size for the inversion is 6 km by 3 km with a grid interval of 10 m. The parameter ϵ for the P-wave anisotropy varies from 0 to 0.15, and δ has values ranging from -0.2 to 0.05. The Thomsen parameters are the same as those in the original model, even though the Poisson's ratio and the density are modified. In the synthetic inversion tests, I assumed that the maximum frequency of the source is 10 Hz, and the record length of the data is 4 seconds. Linearly increasing models were used as initial models, and the conjugate gradient method was applied to accelerate the convergence rate. During the inversion, the source wavelet was estimated because it was assumed to be unknown.

Figures 4.2 and 4.3 show the seismic FWI results obtained by the

isotropic inversion algorithm and their elastic parameter logs extracted at a distance of 3 km, respectively. The recovered elastic parameters are generally reliable. However, the anisotropic properties cannot be obtained with the isotropic inversion algorithm, and the parameters of the anisotropic layers are not recovered properly at depths of approximately 1 km and 2.2 km. These results indicate that the isotropic inversion algorithm cannot provide reliable information for anisotropic media, although the overall resolution is reasonable. Therefore, application of the VTI inversion algorithm is needed to obtain more reliable elastic and anisotropic properties.

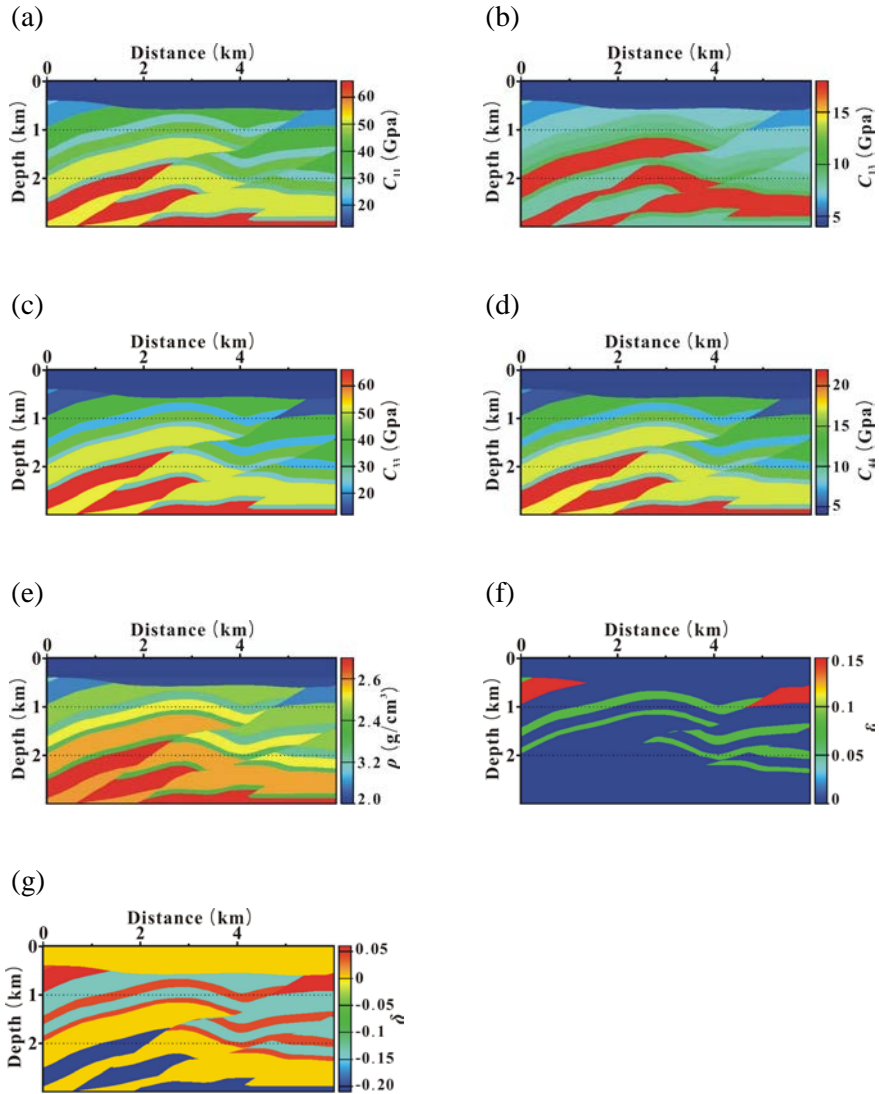


Figure 4.1 Modified versions of the SEG/EAGE overthrust models distributed by Delft University: (a) C_{11} , (b) C_{13} , (c) C_{33} , (d) C_{44} , (e) ρ , (f) ε and (g) δ . Poisson's ratio is fixed at 0.25, and the density is regenerated using the Gardner's relationship.

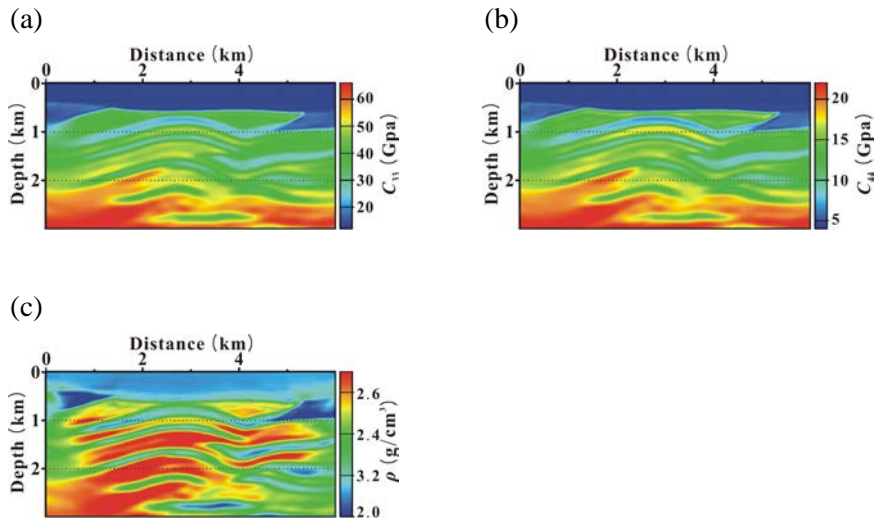


Figure 4.2 Seismic FWI results obtained by the isotropic inversion algorithm based on the Lamé constants parameterization for the modified version of the SEG/EAGE overthrust model: (a) C_{33} , (b) C_{44} and (c) ρ . C_{33} and C_{44} can be obtained from the inverted Lamé constants.

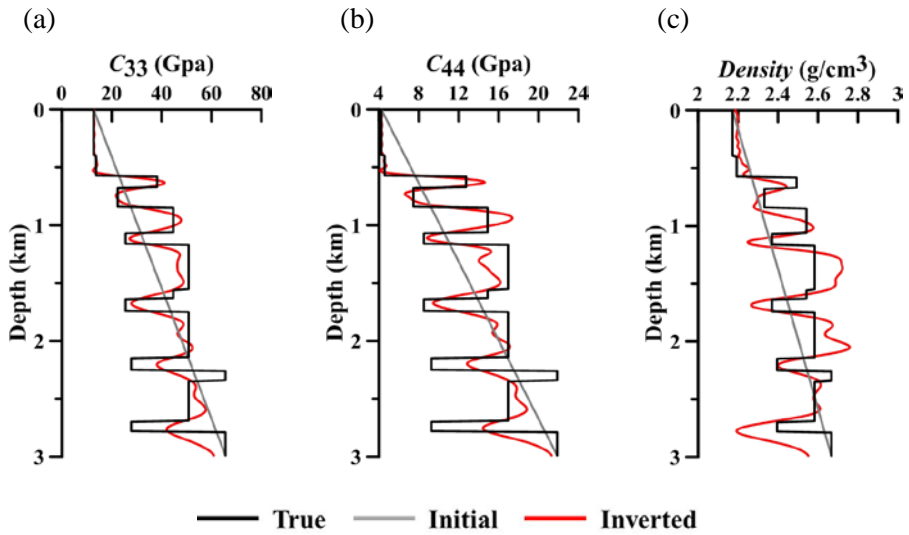


Figure 4.3 Elastic parameter logs extracted at a distance of 3 km of the (black solid lines) true, (gray solid lines) initial and inverted (red solid lines) models obtained by the isotropic inversion algorithm: (a) C_{33} , (b) C_{44} and (c) ρ .

To reconstruct the subsurface properties including the anisotropic parameters, the seismic FWI based on the conventional parameterization was also performed for VTI media (Figure 4.4). The primary parameters (C_{33} and C_{44}) were recovered properly (Figures 4.4c and 4.4d), but the resolution of C_{44} is poorer than that of C_{33} . These results are consistent with those of the sensitivity analysis in the previous chapter. Furthermore, the inversion results of C_{11} and C_{13} are severely distorted (Figures 4.4a and 4.4b), and the density is generally overestimated. Accordingly, ε and δ extracted from the inverted parameters are severely distorted (Figures 4.4f and 4.4g). To improve the inversion results for VTI media, the sequential inversion strategy was applied. This sequential inversion strategy was proposed by Koo et al. (2010), in which C_{33} and C_{44} were inverted first using the isotropic inversion, and then VTI inversion with the conventional VTI parameterization was performed for all the parameters in the second stage. The inversion results obtained by the isotropic inversion in Figure 4.2 were used as initial guesses. Figure 4.5 shows that the sequential inversion strategy provides improved inversion results compared to the conventional VTI inversion. However, the inverted Thomsen parameters still have poor resolutions (Figures 4.5f and 4.5g). The results indicate that the anisotropic parameters still need to be improved, although the inversion results for the anisotropic parameters (C_{11} and C_{13}) are better than those obtained by the conventional VTI parameterization. Furthermore, the sequential strategy has a computational disadvantage because it requires an additional inversion stage, which can be a critical problem in some cases.

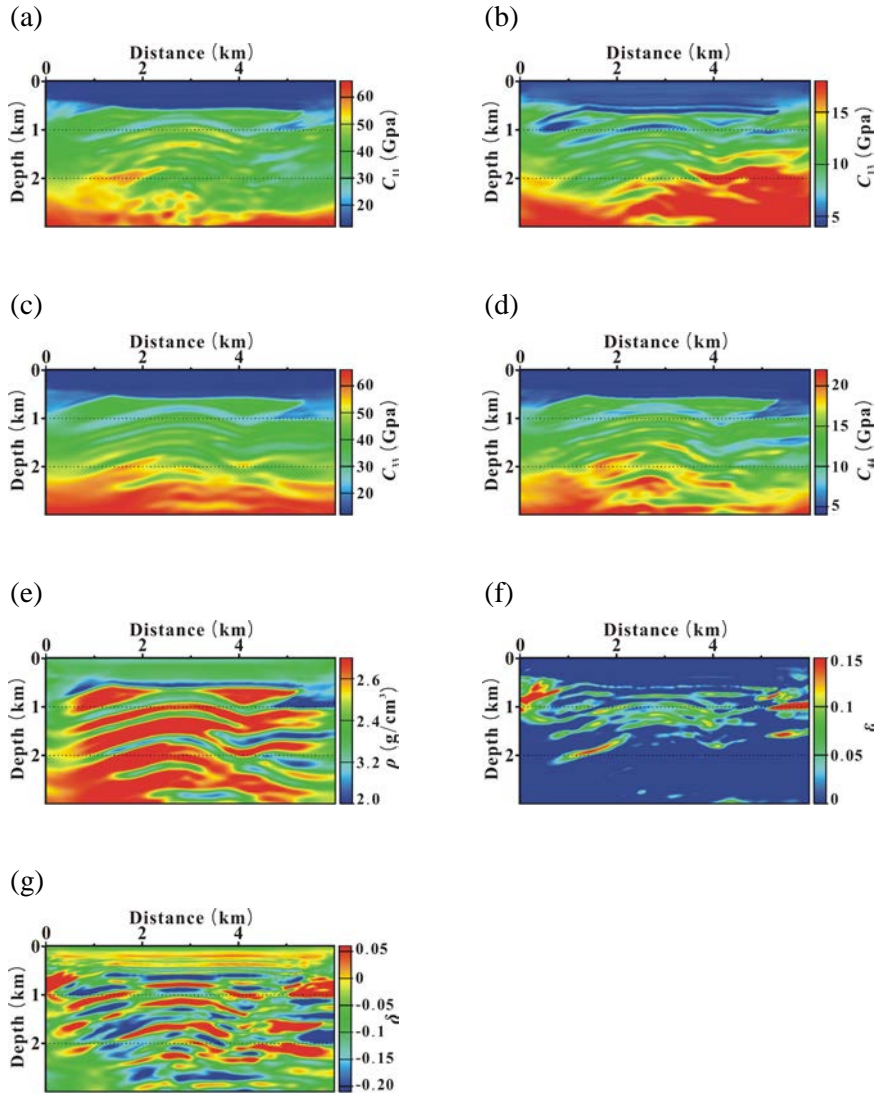


Figure 4.4 Inversion results obtained by the conventional VTI parameterization for the modified version of the SEG/EAGE overthrust models: (a) C_{11} , (b) C_{13} , (c) C_{33} , (d) C_{44} , (e) ρ , (f) ε and (g) δ .

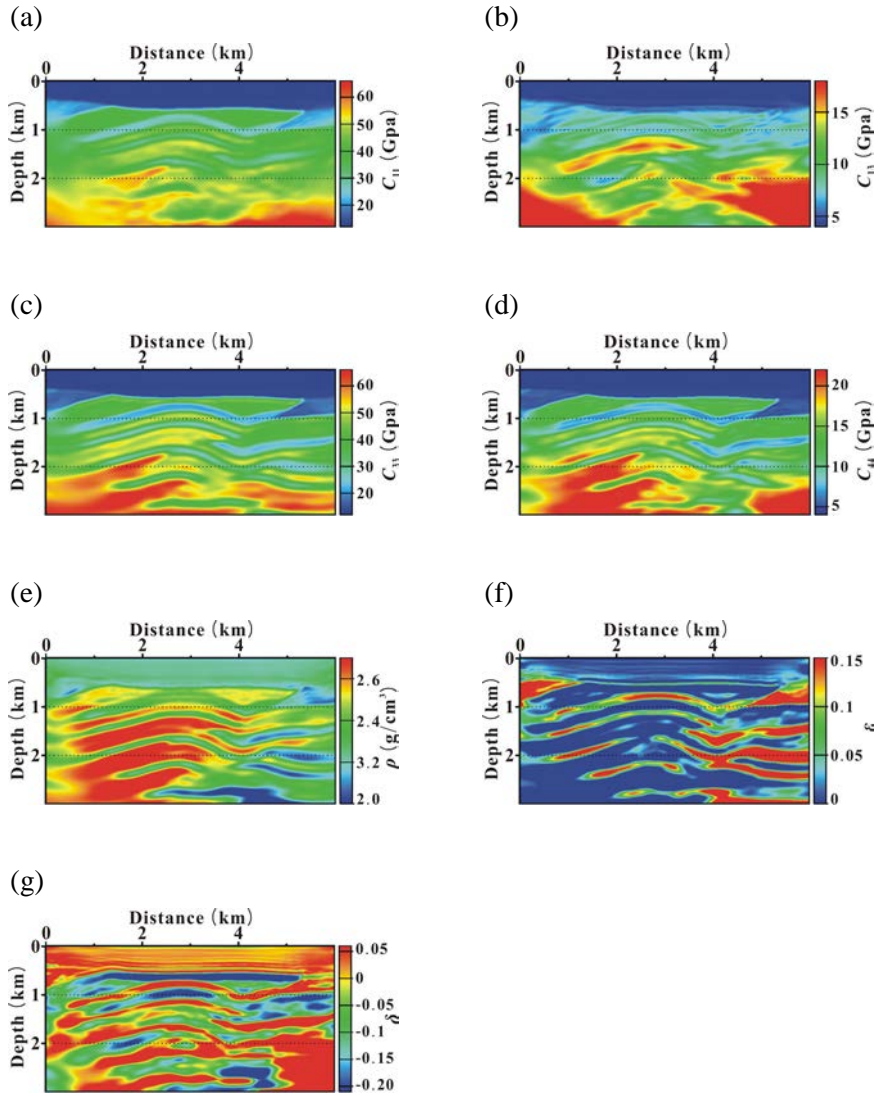


Figure 4.5 Inversion results obtained by the sequential (isotropic-anisotropic) inversion strategy for the modified version of the SEG/EAGE overthrust models: (a) C_{11} , (b) C_{13} , (c) C_{33} , (d) C_{44} , (e) ρ , (f) ϵ and (g) δ . The inversion results obtained by the isotropic inversion in Figure 4.2 are used for initial guesses.

Figure 4.6 shows FWI results obtained with the new parameterization. The inversion results of all the parameters, including the anisotropic parameters and density, are improved compared to those obtained by the conventional and sequential inversions. As described in the sensitivity analyses, these improvements of inversion results for the anisotropic parameters and density result from the improvements of the primary parameters (λ and μ). Figure 4.7 shows the elastic parameter logs extracted at a distance of 3 km. In these logs, the inversion results obtained by the new parameterization are better than those obtained by the sequential inversion and conventional parameterization (Figures 4.7a, 4.7b, 4.7c and 4.7d). Figure 4.7e shows that the inverted density from the new parameterization has sufficient accuracy, whereas the inverted densities from the conventional and sequential inversions contain severe overestimations, although the elastic parameters reconstructed by the sequential inversion are reasonable. These improved elastic parameters can be used to obtain the improved Thomsen parameters through the new parameterization (Figures 4.7f and 4.7g). The inversion results in Figure 4.6 were obtained at the same time, whereas an additional inversion stage was required for the inversion results in Figure 4.5. Therefore, it is clear that the new parameterization has a high computational efficiency compared to the sequential inversion.

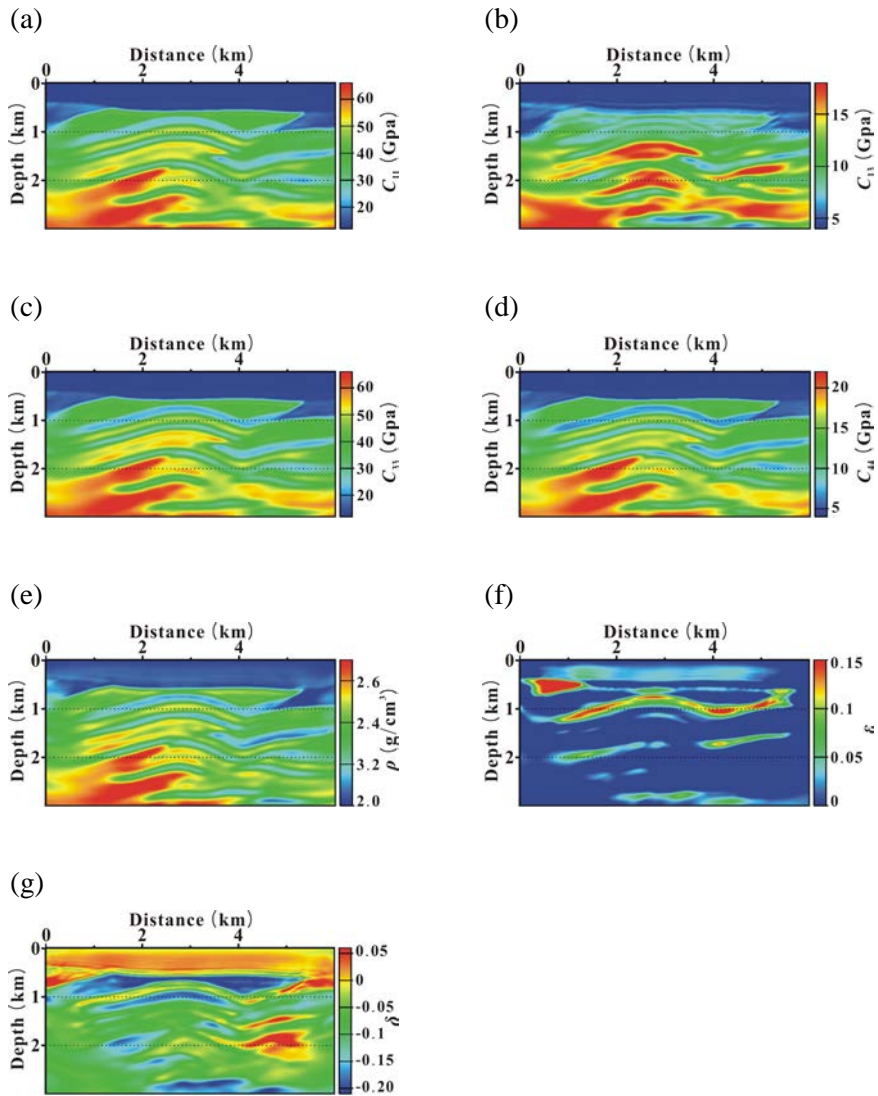


Figure 4.6 Inversion results obtained by the new parameterization for the modified version of the SEG/EAGE overthrust models: (a) C_{11} , (b) C_{13} , (c) C_{33} , (d) C_{44} , (e) ρ , (f) ε and (g) δ .

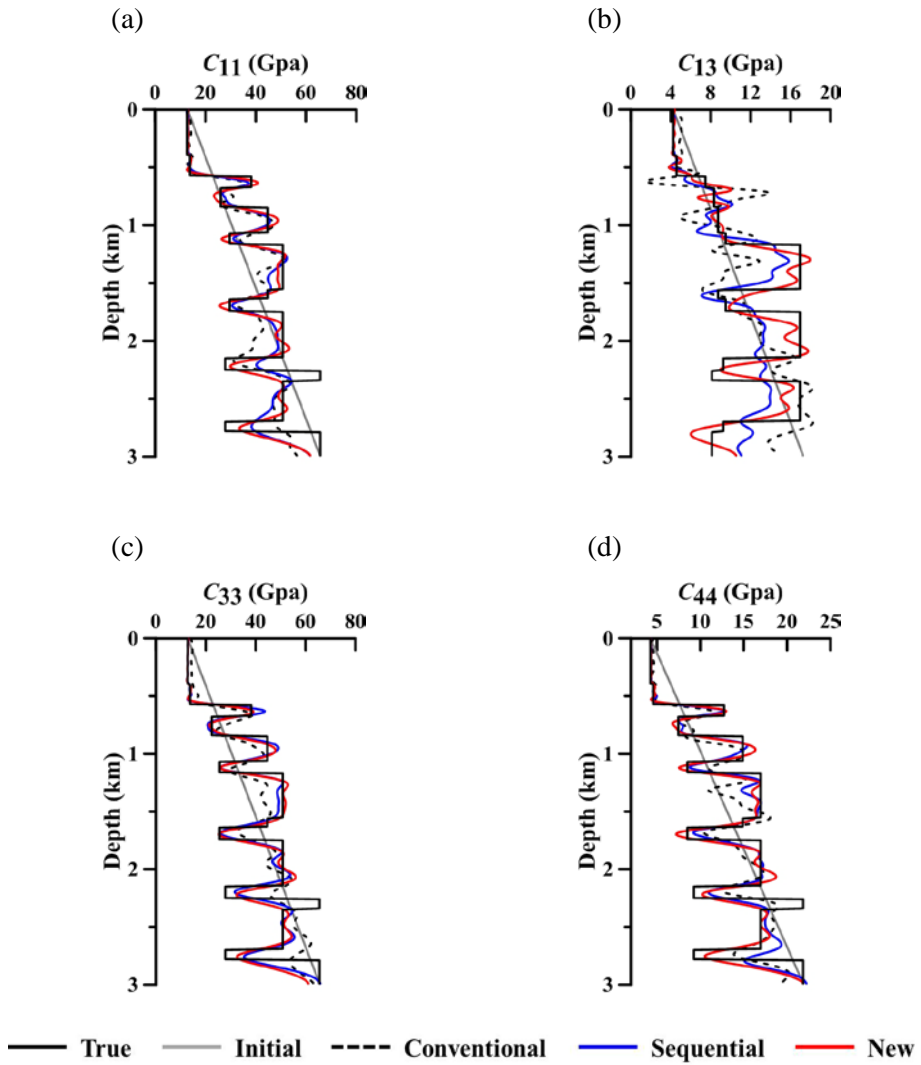


Figure 4.7 Elastic parameter logs extracted at a distance of 3 km of the (black solid lines) true and inverted models obtained by (black dashed lines) the conventional, (blue solid lines) the sequential and (red solid lines) the new inversion: (a) C_{11} , (b) C_{13} , (c) C_{33} , (d) C_{44} , (e) ρ , (f) ε and (g) δ .

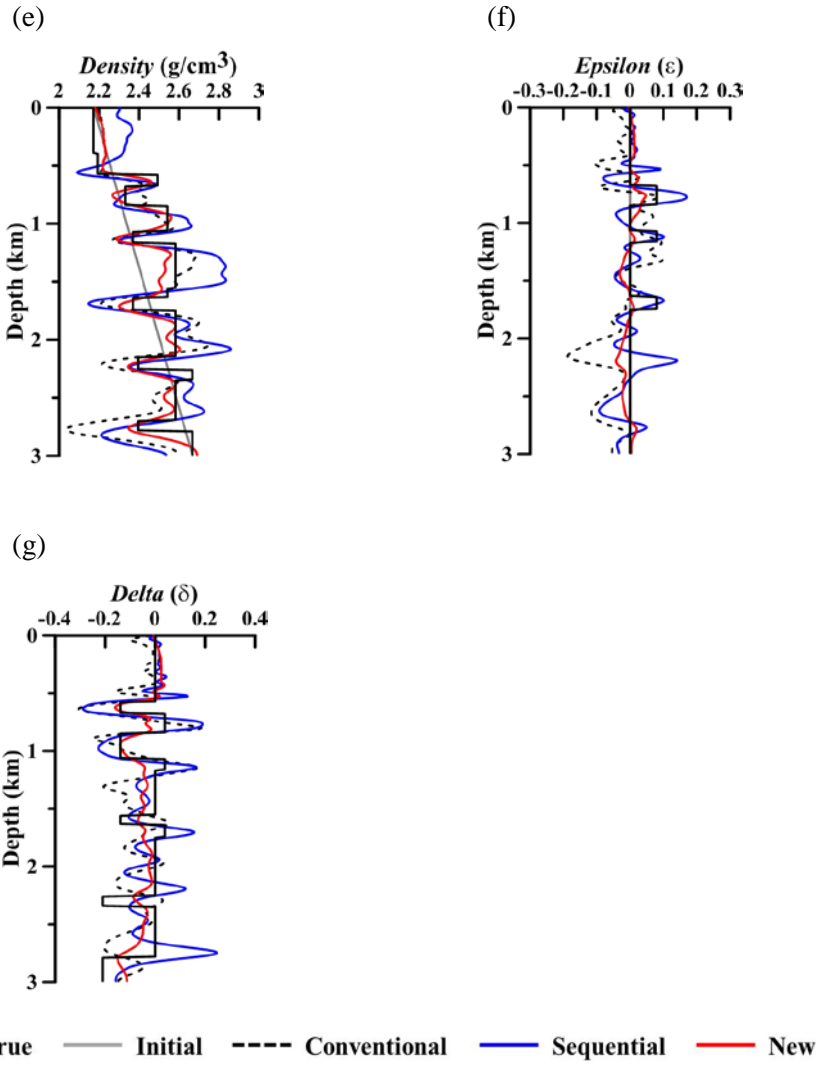


Figure 4.7 (Continued)

Figure 4.8 shows RMS error curves for each inversion technique. In the first stage of the sequential inversion using the isotropic inversion algorithm (gray dashed line), the RMS error is larger than that of the other inversion techniques at the early iteration (black solid line). However, the error is converged more quickly compared to the conventional VTI inversion. This means the isotropic inversion algorithm is better than the conventional VTI inversion algorithm, although anisotropic properties are not considered. The RMS curve for the second stage of the sequential inversion shows that sequential inversion can reduce errors. The RMS curve for the new parameterization converges to small values compared to that of the conventional VTI inversion, and the values are very similar to those of the second stage of the sequential inversion. This achievement is obtained at only one stage of inversion.

To quantify the reliabilities of the inversion results, model mismatch errors are computed using Eq. 4.1.

$$\varepsilon_m = \frac{\|m_i - m_t\|_2}{\|m_t\|_2}, \quad (4.1)$$

where ε_m is the model mismatch error, and m_i and m_t are inverted and true models, respectively. Table 4.1 shows model mismatch errors between the entire inverted and true models. The model mismatch errors for the elastic parameters are similar but the inversion results obtained by the new parameterization are slightly better than those obtained by the conventional

and sequential inversions. In the case of density, the new parameterization provides more improved results than those obtained by the other inversions. Table 4.2 shows the computing time for one iteration step of each inversion technique. The isotropic, conventional VTI and new inversions have a similar computing time, which means the new parameterization does not have computational overburden compared to the isotropic and conventional VTI inversion algorithm. Therefore, it is obvious that the new parameterization can provide improved inversion results without additional computations.

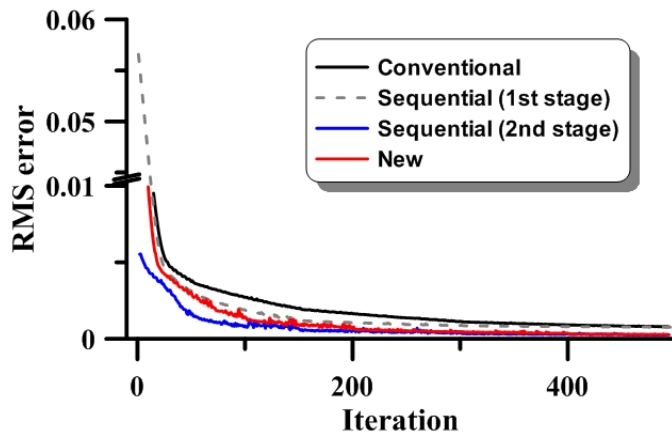


Figure 4.8 RMS error curves for (black solid line) the conventional VTI inversion, (gray dashed line) the isotropic inversion for first stage of the sequential inversion, (blue solid line) the conventional VTI inversion for second stage of the sequential inversion and (red solid line) new inversion for the modified version of the SEG/EAGE overthrust model.

Table 4.1 Model mismatch errors of the final inversion results obtained by the conventional, sequential and new inversions for the modified version of the SEG/EAGE overthrust model.

	C_{11} (%)	C_{13} (%)	C_{33} (%)	C_{44} (%)	ρ (%)
Conventional	0.049	0.108	0.054	0.049	0.015
Sequential	0.047	0.081	0.046	0.051	0.017
New	0.041	0.069	0.043	0.041	0.008

Table 4.2 Computing time for one inversion iteration step for the modified version of the SEG/EAGE overthrust model.

Method	Isotropic	Sequential	New
Time (sec)	97.60	105.38	103.08

4.1.2 Original version of the SEG/EAGE overthrust model

Numerical examples for the modified overthrust model showed that the new parameterization can provide improved inversion results compared to the conventional and sequential inversions without an additional inversion stage. However, real subsurface media are generally characterized by a wide range of Poisson's ratios and complex density structures with wide variations in P- and S-wave velocities. Therefore, additional simulations were performed to verify the efficiency of the new parameterization in more realistic subsurface environments.

To this end, seismic FWIs for the original version of the SEG/EAGE overthrust model were conducted (Figure 4.9) because it has a wide range of Poisson's ratios. In addition, the ranges of parameter values are wider than those in the modified version, which means this original version is more difficult to invert than the modified version of the overthrust model. The FWI settings were the same as the previous FWI settings, but the record length of the data was 5 seconds. A smoothed versions of the true models were used as the starting models (Figure 4.10).

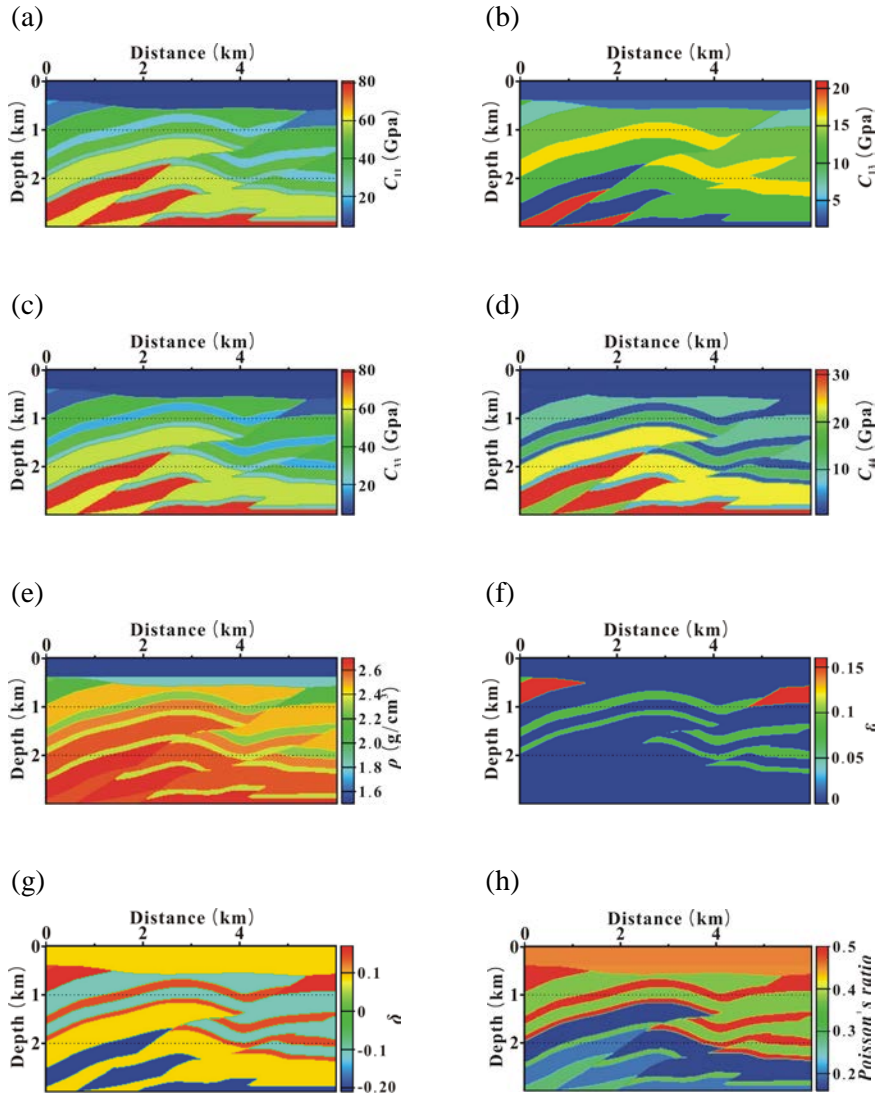


Figure 4.9 Original versions of the SEG/EAGE overthrust models distributed by Delft University: (a) C_{11} , (b) C_{13} , (c) C_{33} , (d) C_{44} , (e) ρ , (f) ϵ , (g) δ and (h) Poisson's ratio.

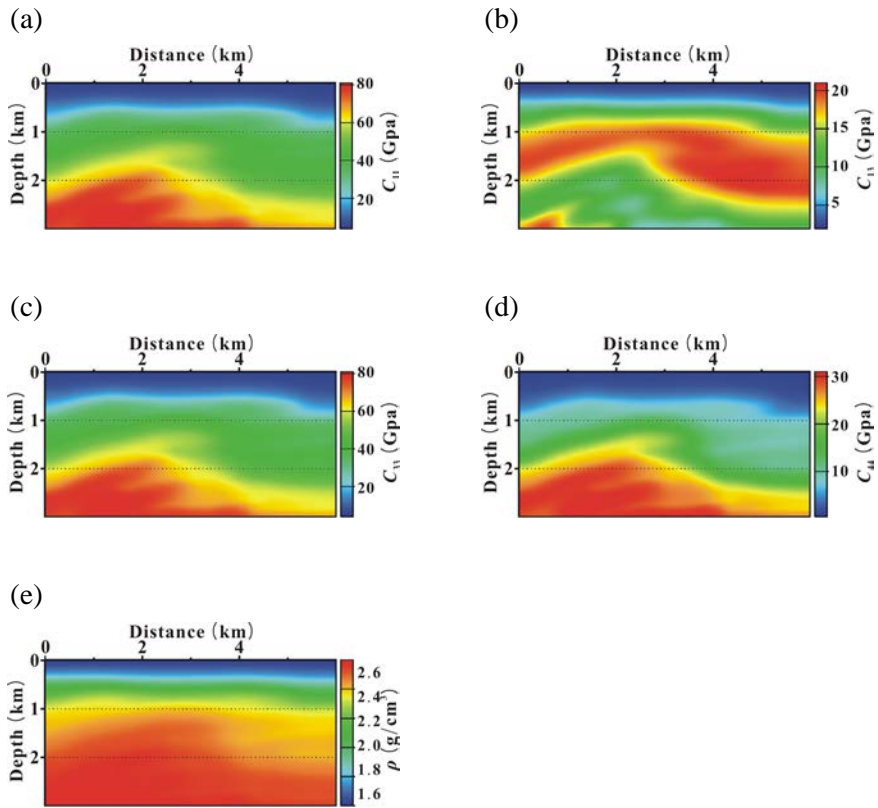


Figure 4.10 The starting models of seismic inversion for the original version of the SEG/EAGE overthrust model: (a) C_{11} , (b) C_{13} , (c) C_{33} , (d) C_{44} and (e) ρ .

Figures 4.11 and 4.12 show the reconstructed elastic parameters, density and Thomsen parameters by the conventional and sequential inversions, respectively. The results show poor resolutions for all the parameters in both inversion cases compared to those for the modified version. In particular, the conventional parameterization does not produce acceptable subsurface properties (Figure 4.11). Accordingly, the Thomsen parameters from Figures 4.11f and 4.11g, which are extracted from the inverted elastic parameters, are very poor across the entire model. The two-stage inversion provides improved inversion results for all the parameters compared to the conventional VTI inversion (Figure 4.12). However, Figures 4.12f and 4.12g show that the extracted Thomsen parameters (ϵ and δ) are still not satisfactory, although the additional FWI was performed to improve the inversion results. Furthermore, the inverted density is severely overestimated (Figure 4.12e). Figure 4.13 shows the inversion results obtained by the new parameterization, in which all the parameters are inverted simultaneously. The resolutions of C_{33} and C_{44} are improved compared to those obtained by the sequential inversion. The recovered values of C_{11} and C_{13} in Figures 4.13a and 4.13b are more accurate than those in Figures 4.12a and 4.12b, respectively. The extracted values of ϵ and δ in Figures 4.13f and 4.13g are also improved compared to those obtained by the sequential inversion. However, large variations of the parameters near the surface (approximately 500 m depth) yield unstable estimates of the Thomsen parameters. To verify the effectiveness of the new parameterization more clearly, the elastic parameter logs were extracted and are compared in Figure 4.14. The figure shows that the new parameterization

provides better inversion results than the other inversion strategies, including for the density. The extracted ε and δ values have more reasonable values than those obtained by the sequential inversion, even though improvement is still needed (Figures 4.14f and 4.14g). These synthetic inversion results support that the new parameterization can improve the inversion results compared to conventional and sequential inversions without an additional inversion.

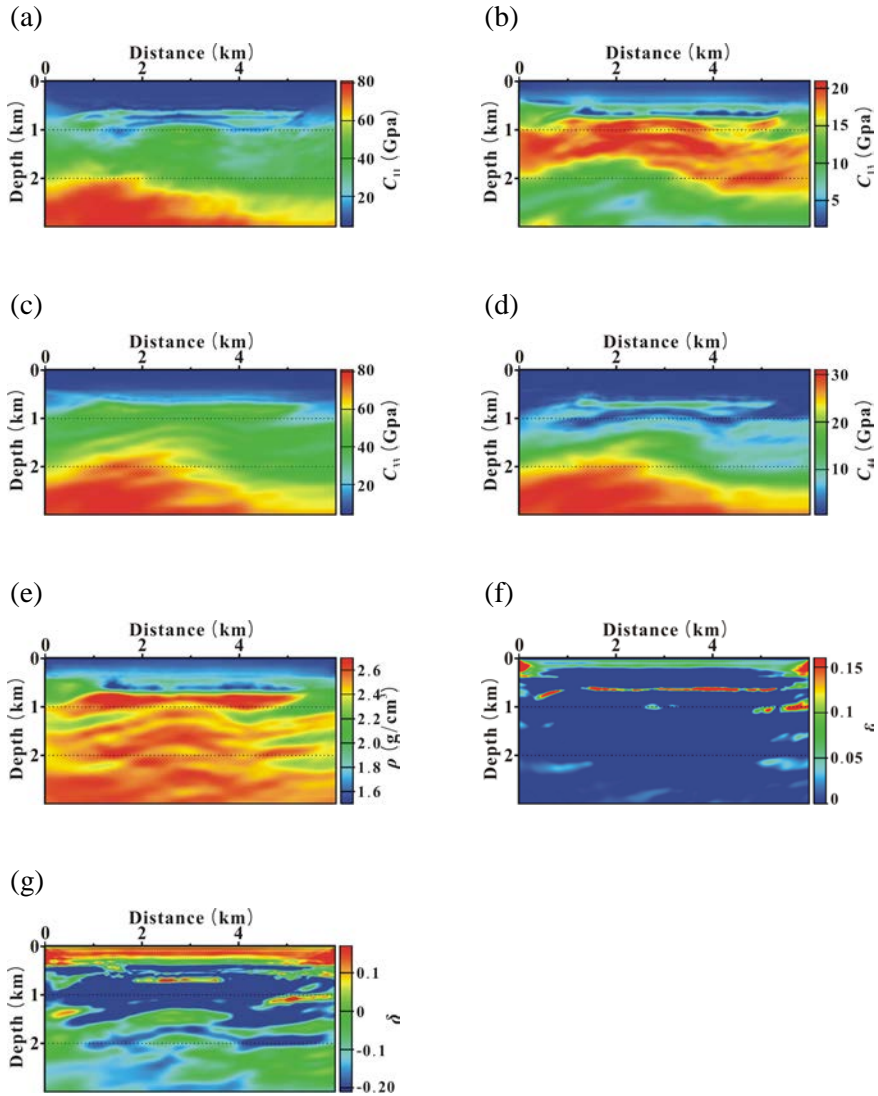


Figure 4.11 Inversion results obtained by the conventional VTI parameterization for the original version of the SEG/EAGE overthrust models: (a) C_{11} , (b) C_{13} , (c) C_{33} , (d) C_{44} , (e) ρ , (f) ϵ and (g) δ .

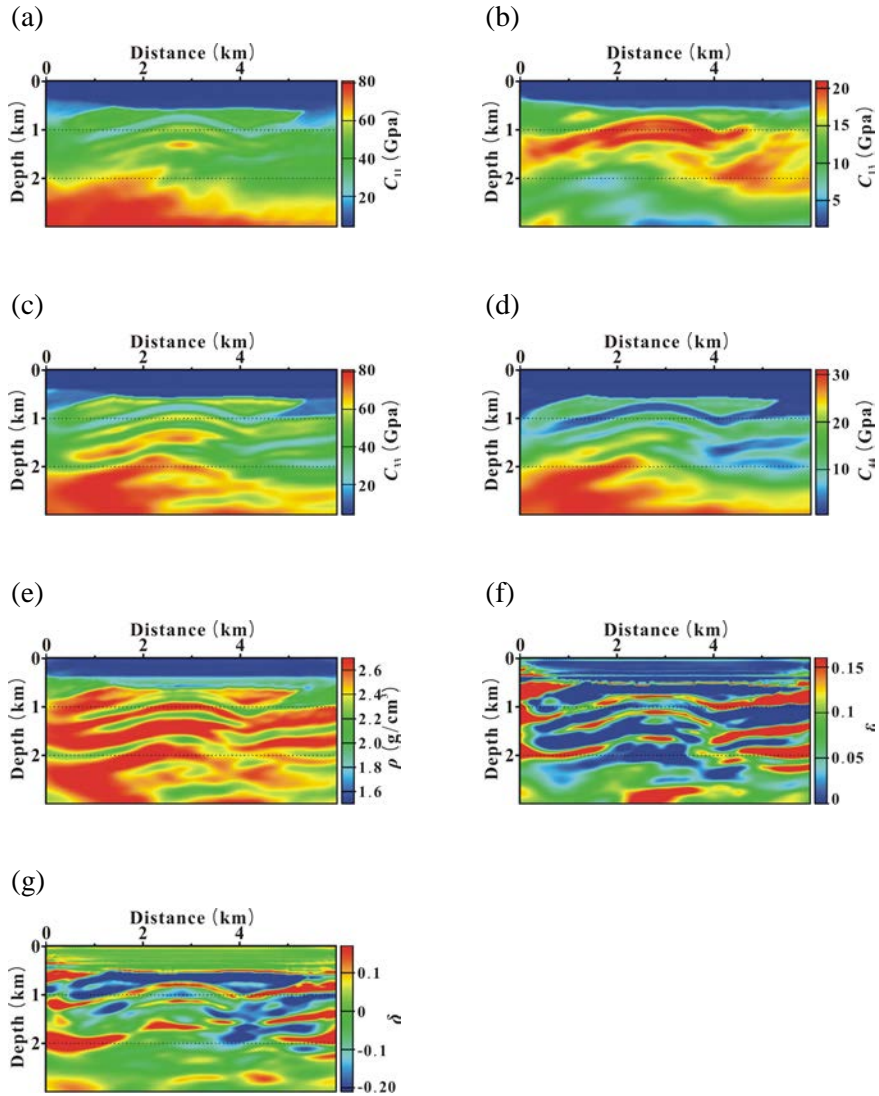


Figure 4.12 Inversion results obtained by the sequential inversion strategy for the original version of the SEG/EAGE overthrust models: (a) C_{11} , (b) C_{13} , (c) C_{33} , (d) C_{44} , (e) ρ , (f) ϵ and (g) δ . The inversion results obtained by the isotropic inversion (not presented in this dissertation) are used for the initial models.

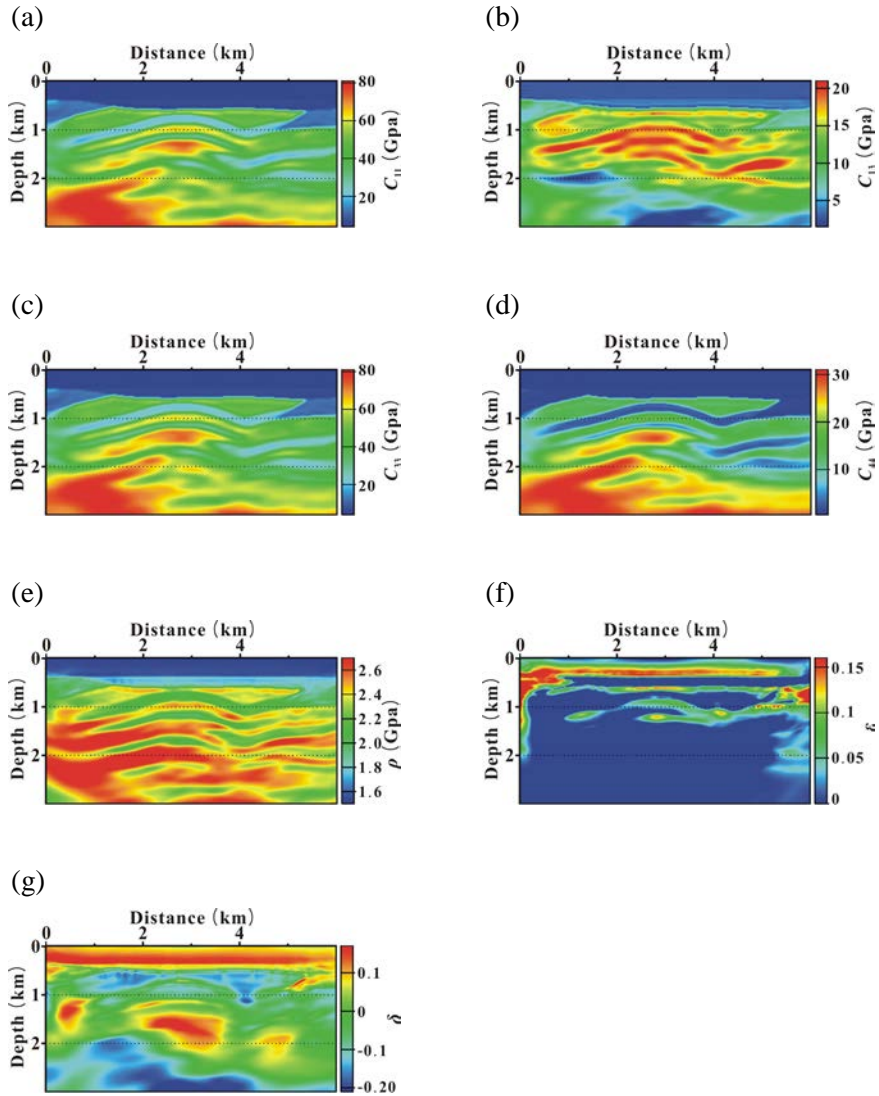


Figure 4.13 Inversion results obtained by the new parameterization for the original version of the SEG/EAGE overthrust models: (a) C_{11} , (b) C_{13} , (c) C_{33} , (d) C_{44} , (e) ρ , (f) ϵ and (g) δ .

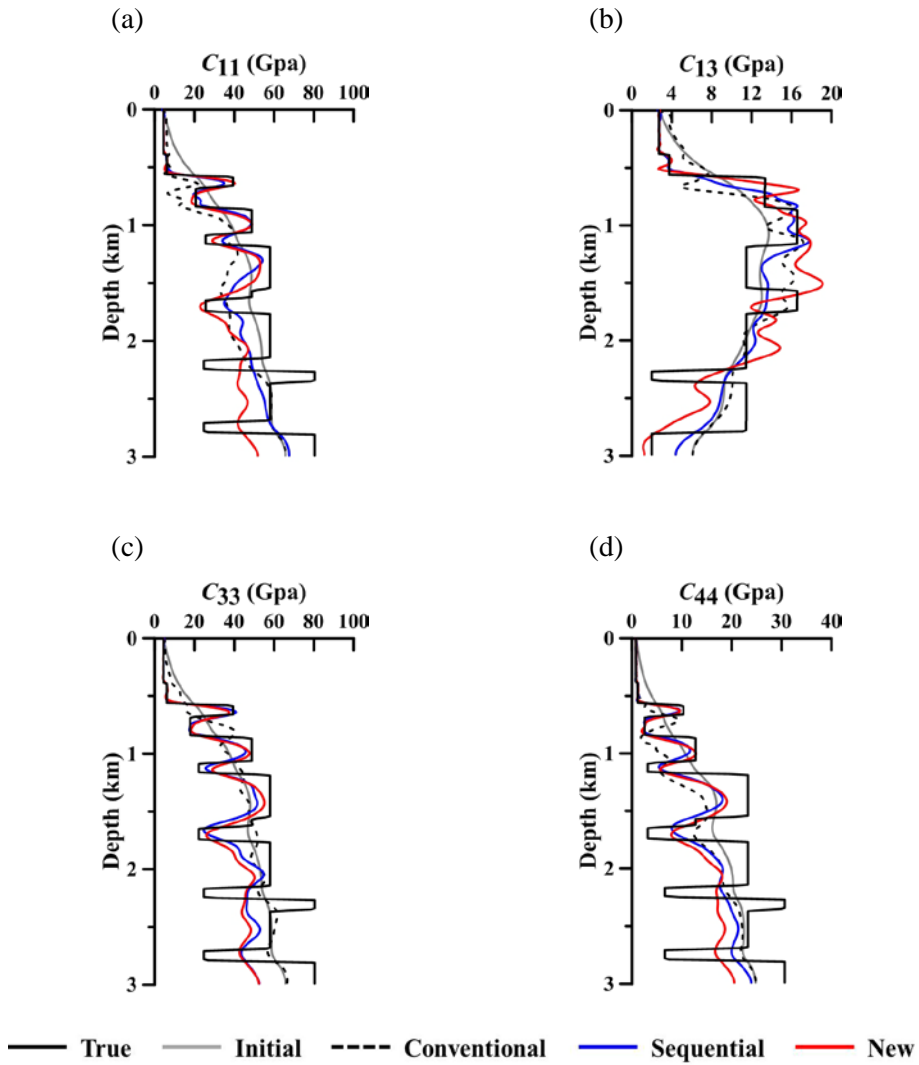


Figure 4.14 Elastic parameter logs extracted at a distance of 3 km of the (black solid lines) true and inverted models obtained by (black dashed lines) the conventional, (blue solid lines) the sequential and (red solid lines) the new inversion: (a) C_{11} , (b) C_{13} , (c) C_{33} , (d) C_{44} , (e) ρ , (f) ε and (g) δ .

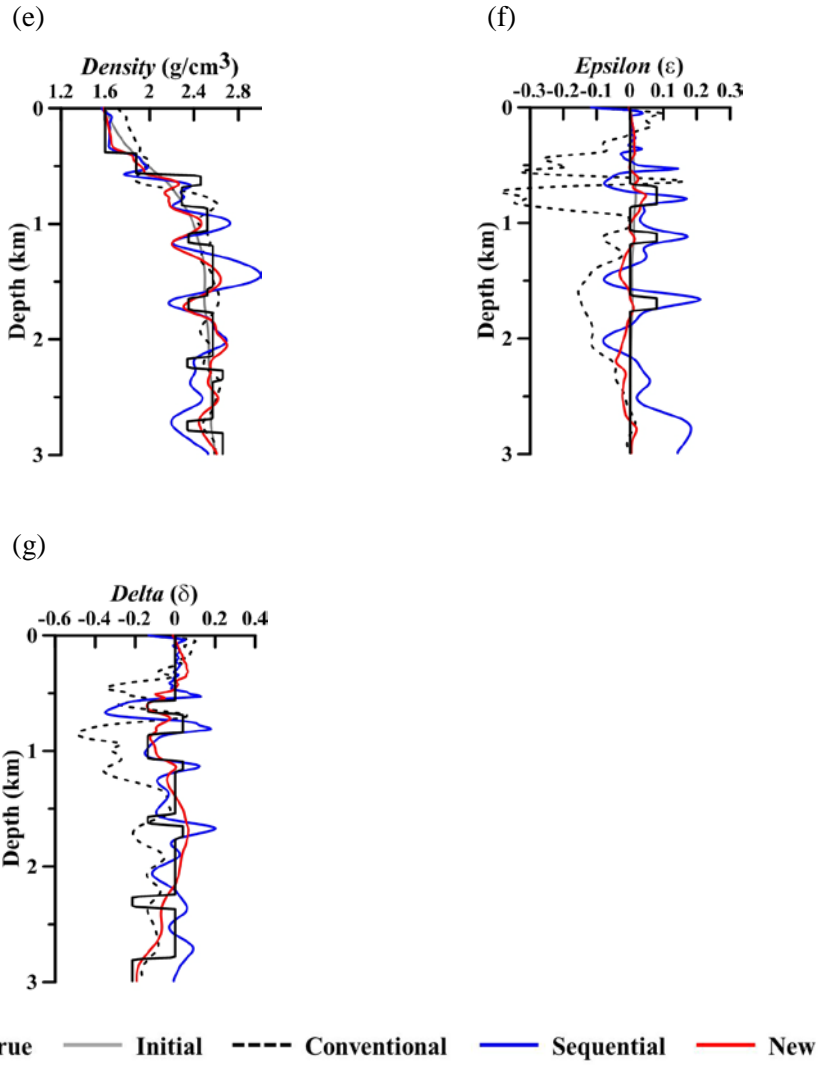


Figure 4.14 (Continued)

Figure 4.15 shows the reconstructed Poisson's ratio obtained by the inverted elastic parameters. The sequential and new inversions produce improved Poisson's ratio information compared to conventional VTI inversion because of the improved inversion results. These improvements are well identified in the depth log in Figure 4.16. The resolutions of sequential and new inversions are very similar. However, the Poisson's ratio recovered by the new parameterization is more stable than that of the sequential inversion (Fig 4.15c and 4.15d). The RMS curves in Figure 4.17 also show that the new parameterization provides improved inversion results compared to those obtained by the conventional VTI parameterization. It converges to a very similar error level as the sequential inversion. However, it must be considered that the inversion results of the new parameterization were obtained after only one inversion stage, whereas the results of the sequential inversion were obtained after two inversion stages. Table 4.3 represents model mismatch errors for each inversion technique. The mismatch errors of the new parameterization are slightly better than that of the conventional VTI inversion, and the values are not good compared to the sequential inversion, although the differences are not much larger. However, the new parameterization has very low values of mismatch errors for the density and Poisson's ratio, thus supporting that the new parameterization still exhibits effectiveness for the media with a wide Poisson's ratio and complex density distributions.

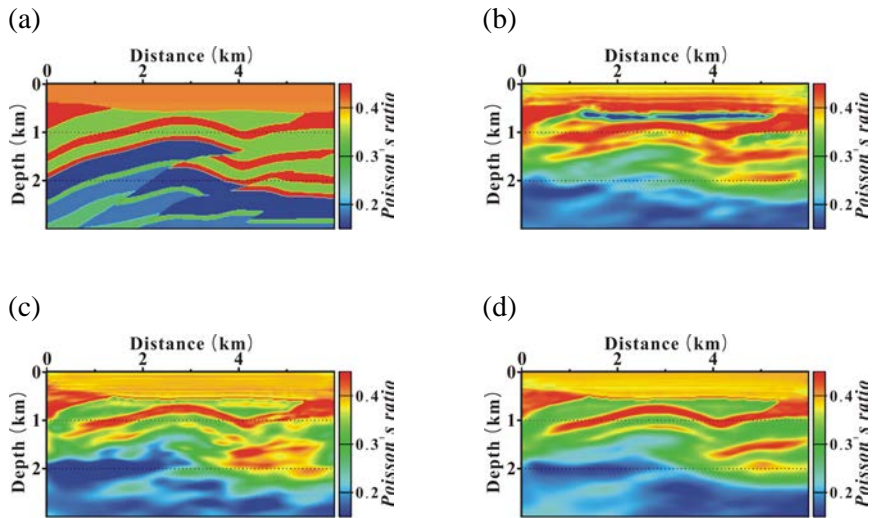


Figure 4.15 (a) True and reconstructed Poisson's ratio obtained by (b) the conventional, (c) the sequential and (d) the new inversion for the original version of the SEG/EAGE overthrust models.

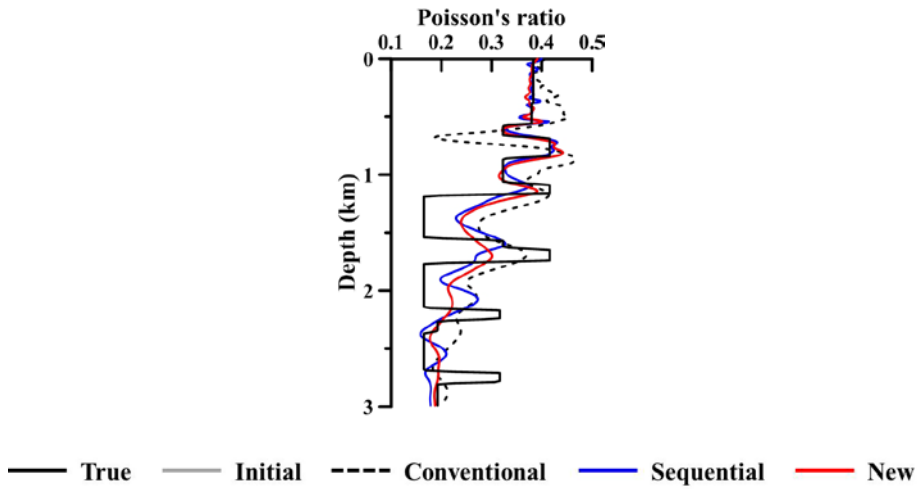


Figure 4.16 Poisson's ratio logs extracted at a distance of 3 km of the (black solid lines) true and inverted models obtained by (black dashed lines) the conventional, (blue solid lines) the sequential and (red solid lines) the new inversion.

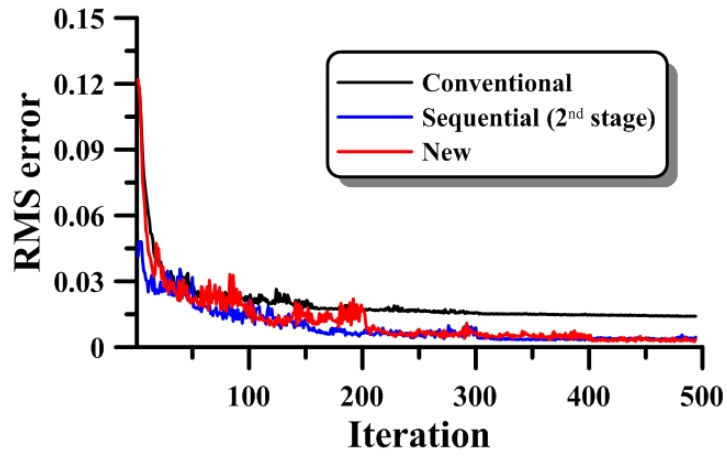


Figure 4.17 RMS error curves for (black solid line) the conventional VTI inversion, (gray dashed line) the isotropic inversion for first stage of the sequential inversion, (blue solid line) the conventional VTI inversion for second stage of the sequential inversion and (red solid line) new inversion.

Table 4.3 Model mismatch errors of the final inversion results obtained by the conventional, sequential and new inversions for the original version of the SEG/EAGE overthrust model.

	C_{11} (%)	C_{13} (%)	C_{33} (%)	C_{44} (%)	ρ (%)	Poisson's ratio
Conventional	0.076	0.080	0.069	0.085	0.018	0.052
Sequential	0.058	0.066	0.060	0.076	0.015	0.046
New	0.066	0.074	0.066	0.081	0.011	0.035

4.2 The SEG/HESS VTI model

4.2.1 Modified SEG/HESS VTI model

Seismic FWIs using the conventional VTI parameterization, the sequential inversion strategy and the new parameterization were also performed for the SEG/HESS VTI model, which contains a salt body having a high velocity and a low density (Figure 4.18; http://software.seg.org/datasets-/2D/Hess_VTI). This model originally contained a water layer, which made C_{44} equal to zero; thus, the water layer was removed, and the sea bottom was considered as the top layer of the model.

It is well known that seismic inversion for salt bodies is challenging due to the reversed tendencies of seismic velocities and density for salt bodies and the large velocity contrasts between the salt body and the surrounding layers. Furthermore, the gradient direction in our inversion algorithm is preconditioned by the pseudo-Hessian matrix in each frequency, which makes causes the gradient direction to be more affected by high frequency components than low frequency components. Accordingly, it is difficult to recover subsurface model parameters properly through our inversion algorithm for salt bodies. To overcome this problem, the weighting technique suggested by Oh and Min (2013) was adopted. The conjugate gradient method was also applied for efficient convergence rate, and source wavelet estimation was applied. Smoothed versions of the true model were used for initial guesses (Figure 4.19).

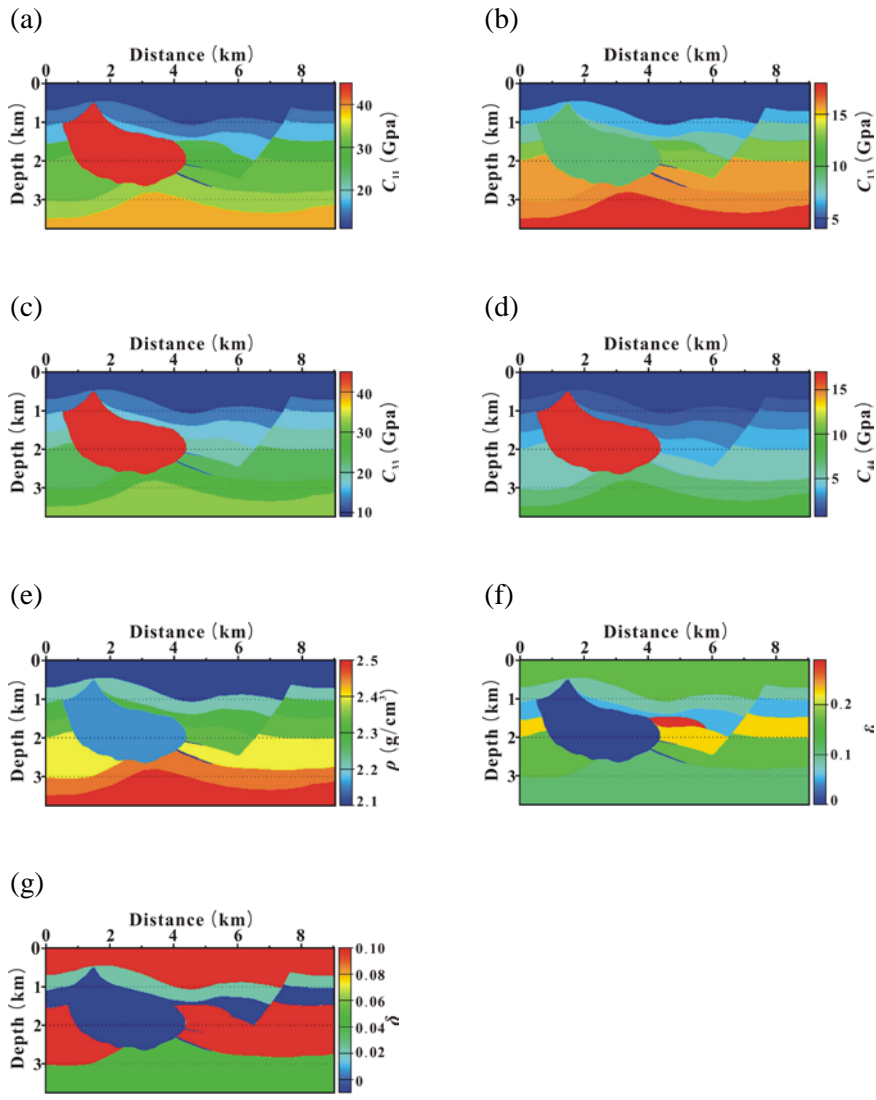


Figure 4.18 The SEG/Hess VTI models: (a) C_{11} , (b) C_{13} , (c) C_{33} , (d) C_{44} , (e) ρ , (f) ϵ and (g) δ .

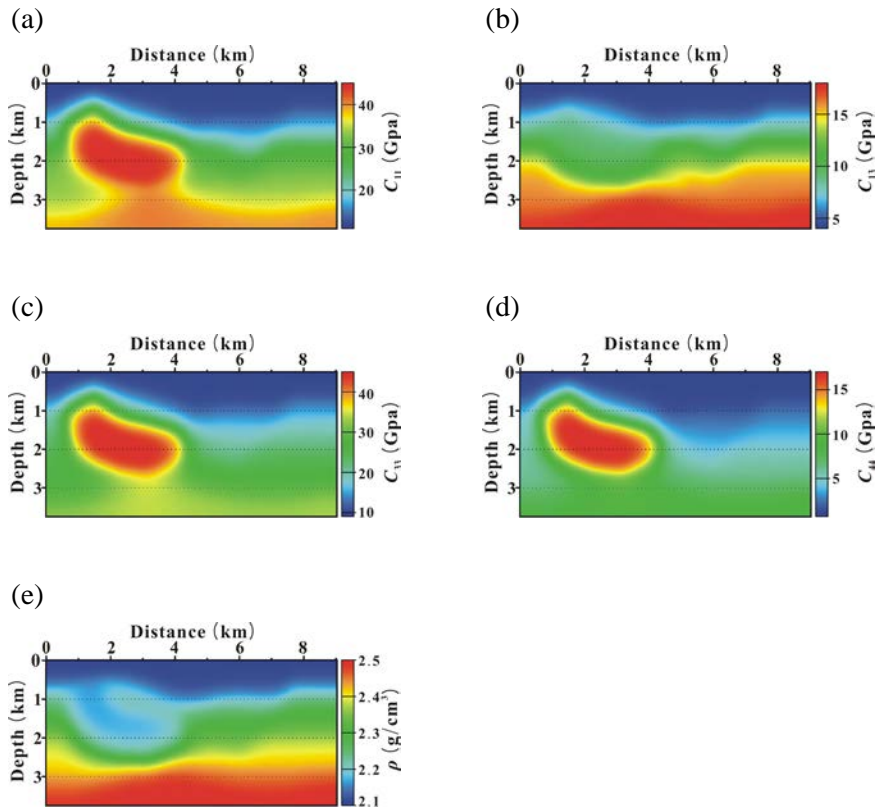


Figure 4.19 The initial guesses of seismic inversion for the SEG/HESS VTI models: (a) C_{11} , (b) C_{13} , (c) C_{33} , (d) C_{44} and (e) ρ .

Figure 4.20 shows the recovered elastic parameters by the isotropic inversion. The inverted C_{33} and C_{44} are reliable, and the salt body is reconstructed well. However, the inversion result for density is very poor (Figure 4.20c). In particular, the density of the salt body, which is inversely proportional to the seismic velocity, is not recovered properly. Figures 4.21 and 4.22 show the elastic parameter logs extracted at distances of 2.26 km and 4.52 km, respectively. It can be seen that C_{33} and C_{44} of the salt body are underestimated, and the density is not recovered properly (Figure 4.21). Furthermore, thin structures at depths of approximately 2.1 km and 2.5 km are not identified in the elastic parameter logs extracted at a distance of 4.52 km (Figure 4.22), and the anisotropic properties cannot be obtained.

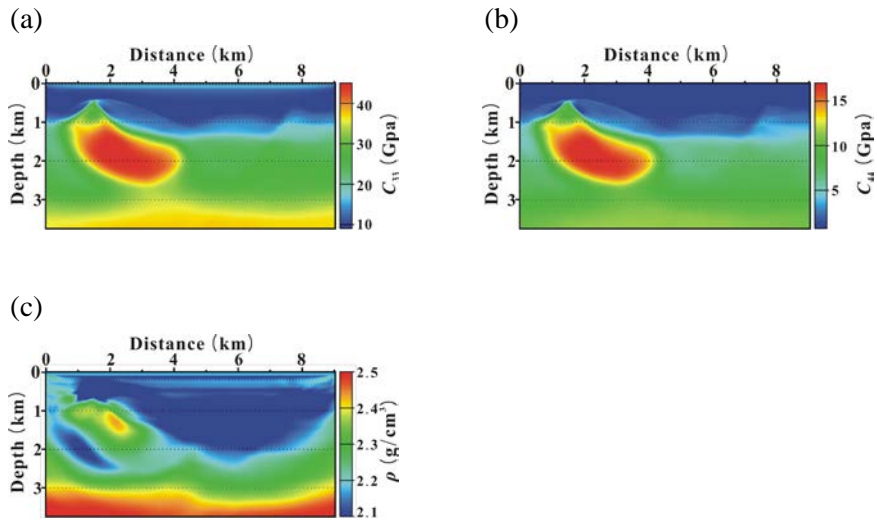


Figure 4.20 Seismic FWI results obtained by the isotropic inversion algorithm based on the Lamé constants parameterization for the SEG/HESS VTI model: (a) C_{33} , (b) C_{44} and (c) ρ . C_{33} and C_{44} can be obtained from the Lamé constants (λ and μ).

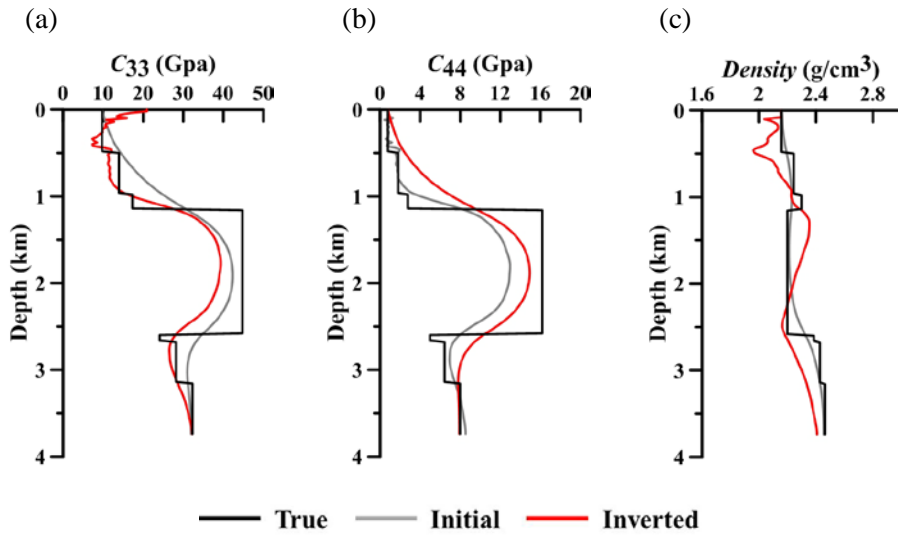


Figure 4.21 Elastic parameter logs extracted at a distance of 2.26 km of the (black solid lines) true, (gray solid lines) initial and inverted (red solid lines) models: (a) C_{33} , (b) C_{44} and (c) ρ . Inversion results are obtained by the isotropic inversion algorithm.

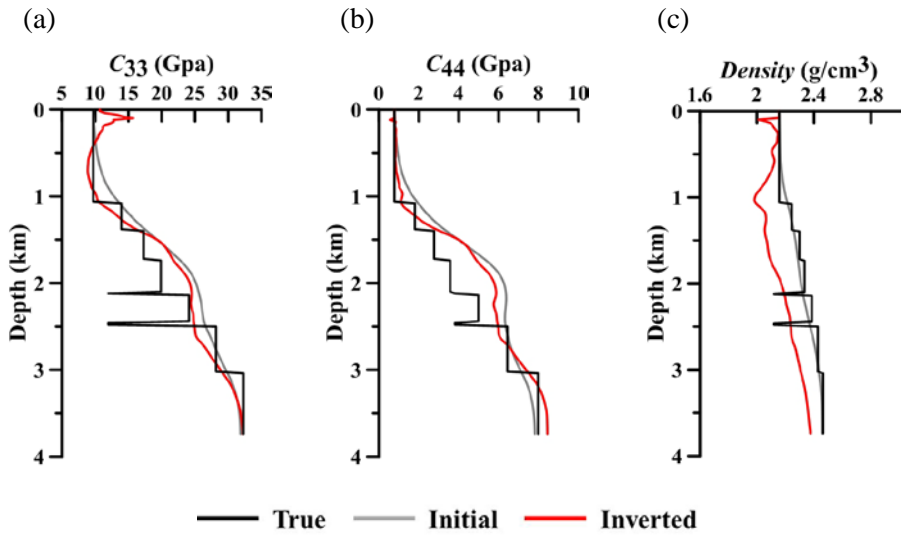


Figure 4.22 Elastic parameter logs extracted at a distance of 4.52 km of the (black solid lines) true, (gray solid lines) initial and inverted (red solid lines) models: (a) C_{33} , (b) C_{44} and (c) ρ . Inversion results are obtained by the isotropic inversion algorithm.

Figure 4.23 shows the inversion results obtained by the conventional VTI parameterization; Figure 4.24 shows the reconstructed elastic parameters, density, and the extracted Thomsen parameters by the sequential inversion using the isotropic inversion results as initial guesses (Figure 4.20). The sequential inversion strategy provides better inversion results than the conventional VTI inversion. C_{33} and C_{44} are slightly improved for the salt body, and C_{11} and C_{13} are significantly improved. However, the density of the salt body is severely overestimated. The Thomsen parameters extracted from the inverted elastic parameters are poor in both the conventional and sequential inversions due to the poor inversion results of the elastic parameters. Figure 4.25 shows the inversion results obtained by the new parameterization. All the parameters are reconstructed well compared to those obtained by the conventional and sequential inversions. The inversion results for the density of the salt body still require improvements. However, the new parameterization produces compatible results without an additional inversion stage. Figure 4.26 shows elastic parameter logs extracted at a distance of 2.26 km of the models. It is shown that the inversion results for all the parameters obtained by the new parameterization are improved compared to those obtained with the conventional and sequential inversions. The extracted Thomsen parameters (Figures 4.26f and 4.26g) are more accurate than the other inversion results because of the improved elastic parameters, although some improvements are still needed. In addition, Figure 4.27 shows that the thin structures at depths of 2.1 km and 2.5 km are identified although the values are not accurate.

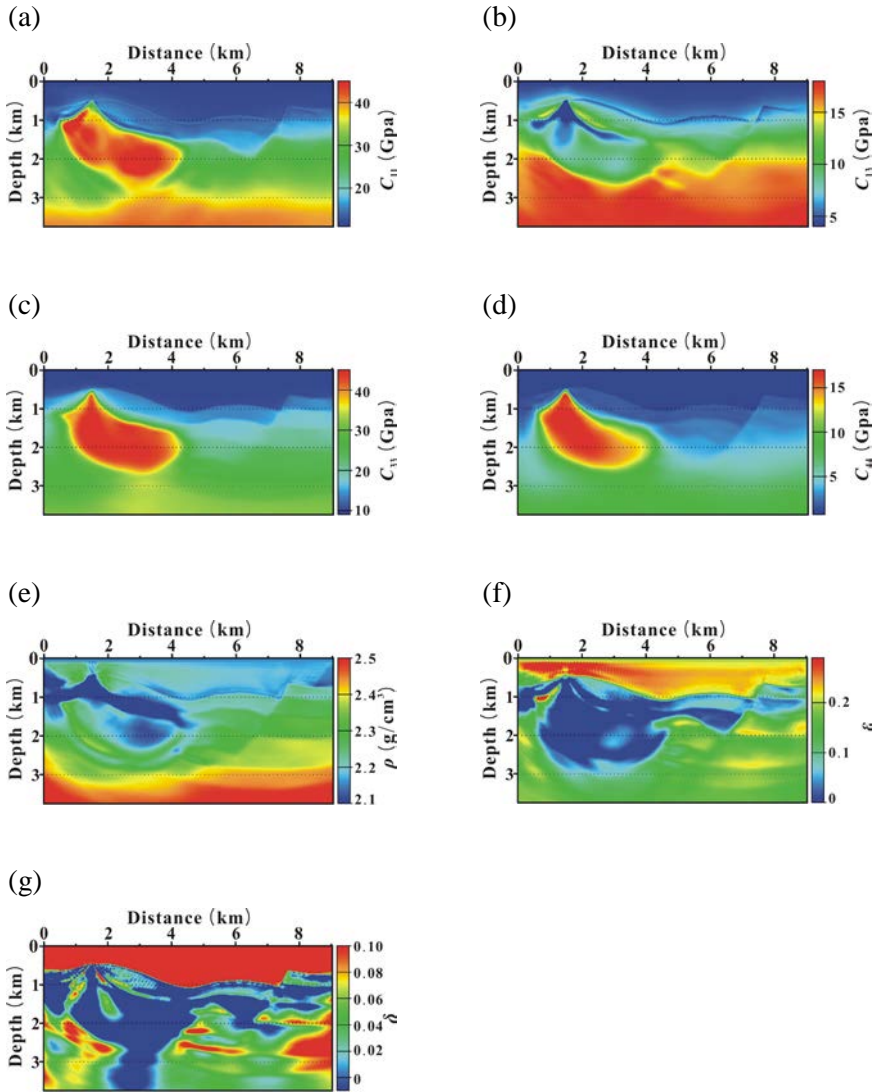


Figure 4.23 Inversion results obtained by the conventional VTI parameterization for the SEG/HESS VTI model: (a) C_{11} , (b) C_{13} , (c) C_{33} , (d) C_{44} , (e) ρ , (f) ϵ and (g) δ .

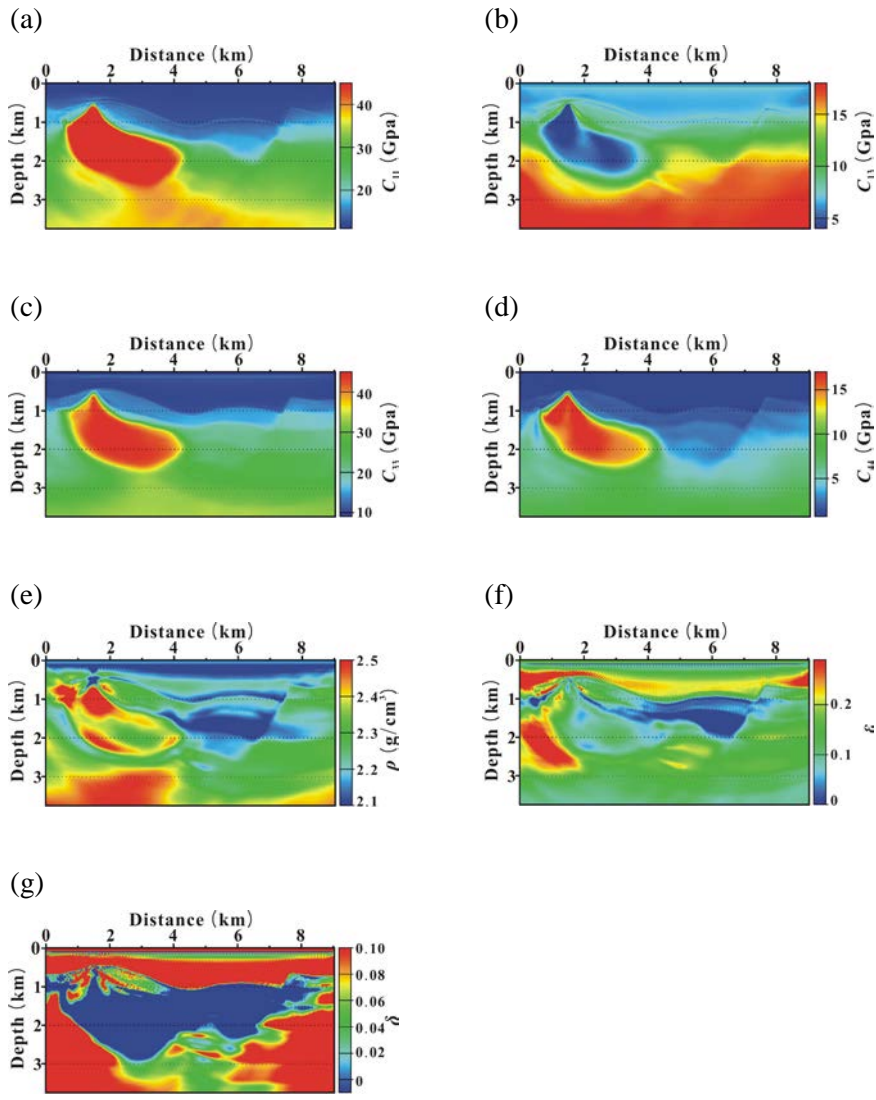


Figure 4.24 Inversion results obtained by the sequential inversion: (a) C_{11} , (b) C_{13} , (c) C_{33} , (d) C_{44} , (e) ρ , (f) ϵ and (g) δ . The inversion results obtained by the isotropic inversion in Figure 4.16 are used for the initial models.

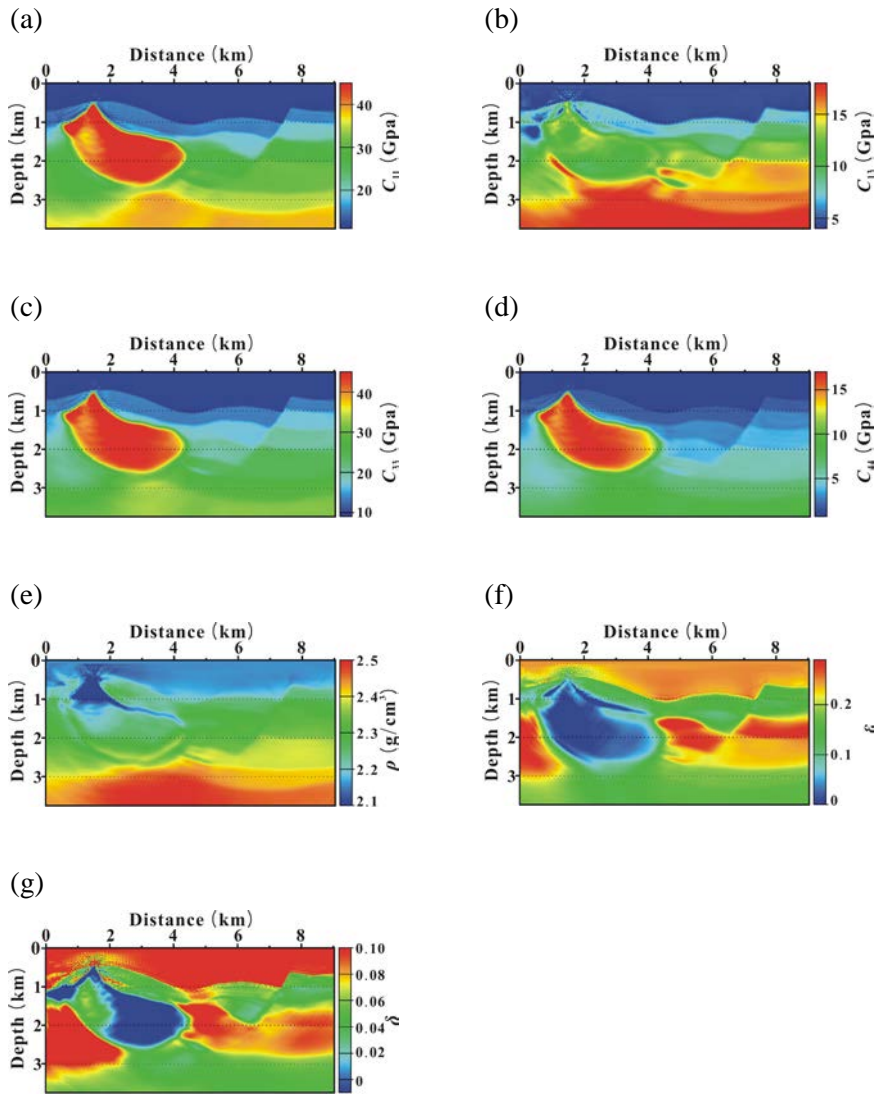


Figure 4.25 Inversion results obtained by the new parameterization: (a) C_{11} , (b) C_{13} , (c) C_{33} , (d) C_{44} , (e) ρ , (f) ε and (g) δ .

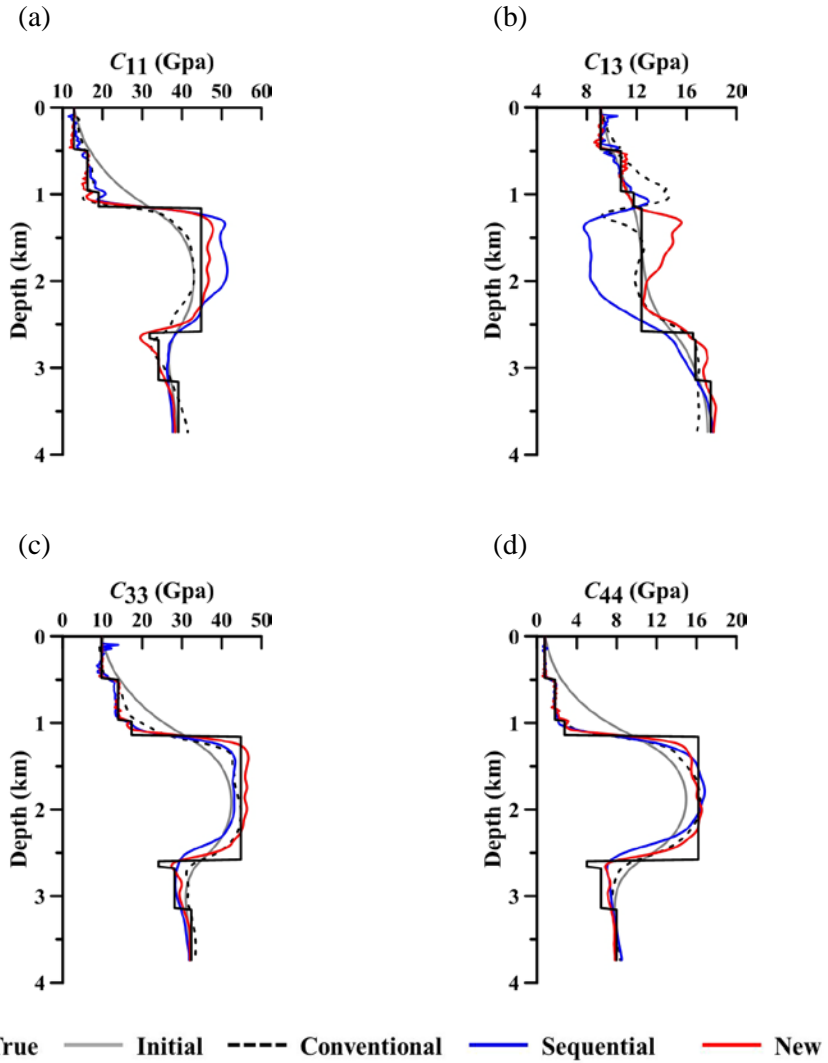


Figure 4.26 Elastic parameter logs extracted at a distance of 2.26 km of the (black solid lines) true and inverted models obtained by (black dashed lines) the conventional, (blue solid lines) the sequential and (red solid lines) the new inversion: (a) C_{11} , (b) C_{13} , (c) C_{33} , (d) C_{44} , (e) ρ , (f) ε and (g) δ .

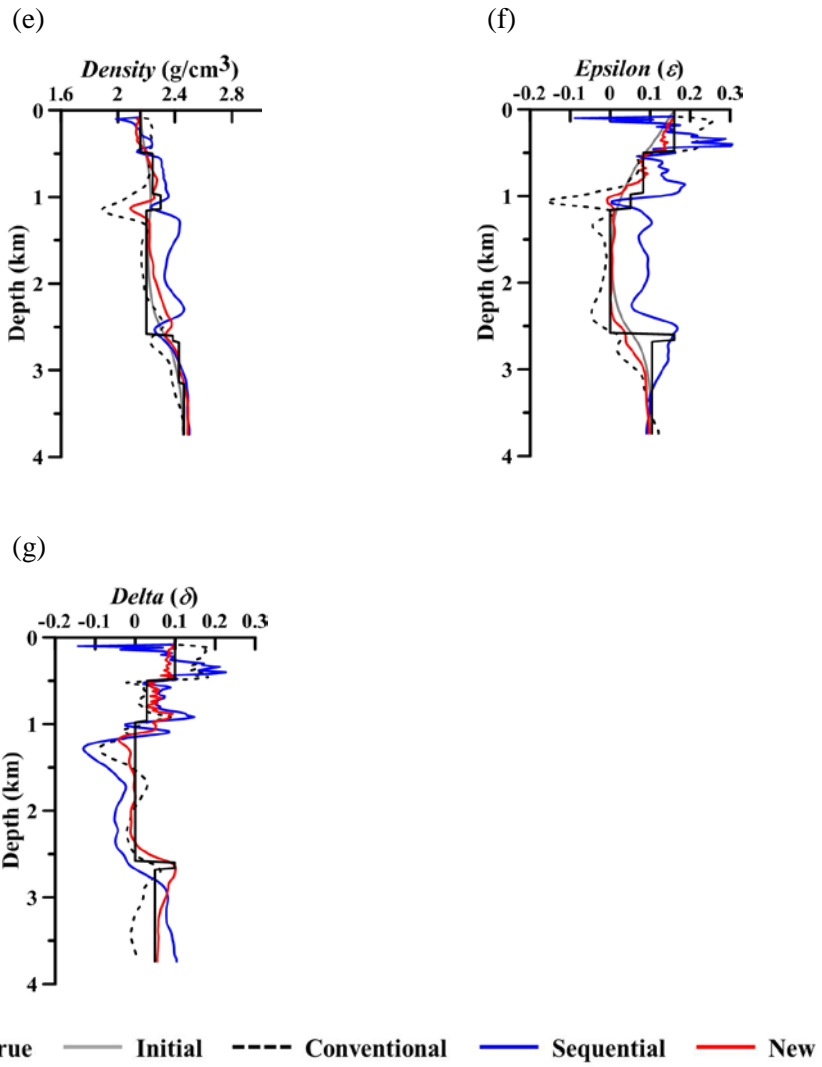


Figure 4.26 (Continued)

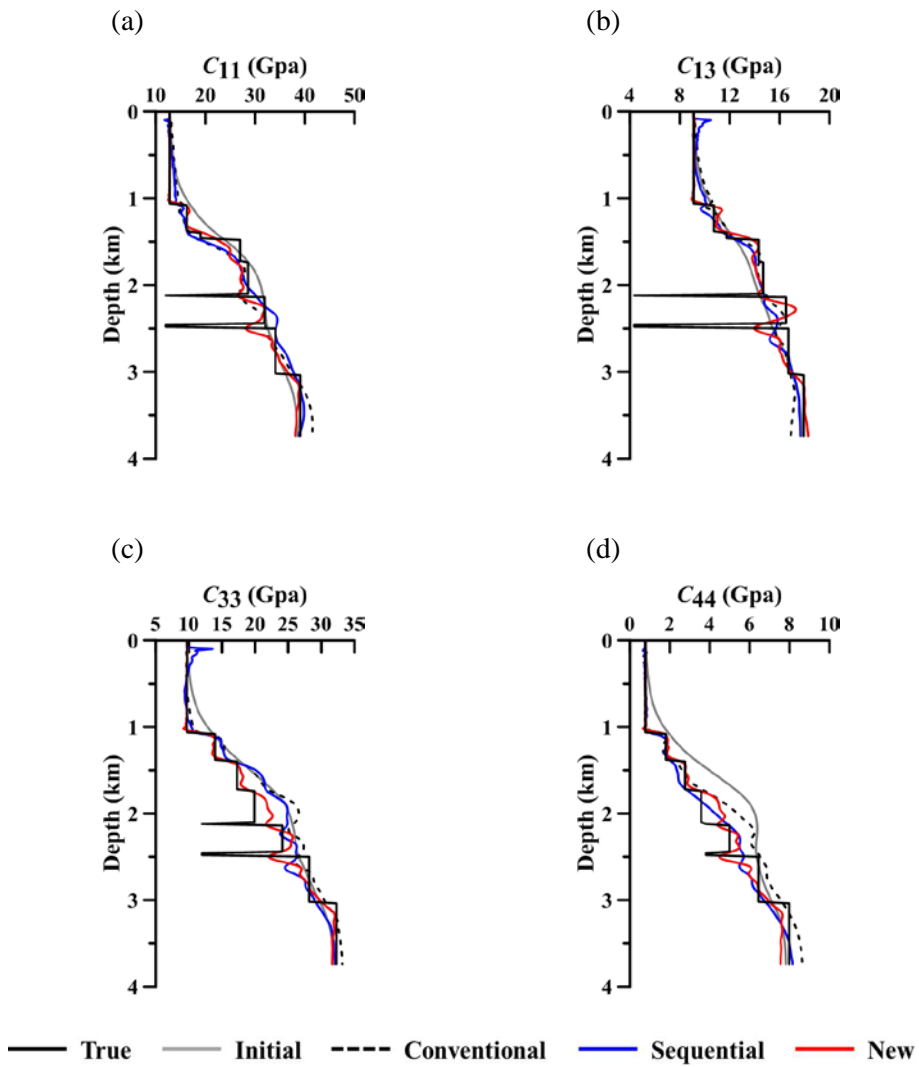


Figure 4.27 Elastic parameter logs extracted at a distance of 4.52 km of the (black solid lines) true and inverted models obtained by (black dashed lines) the conventional, (blue solid lines) the sequential and (red solid lines) the new inversion: (a) C_{11} , (b) C_{13} , (c) C_{33} , (d) C_{44} , (e) ρ , (f) ε and (g) δ .

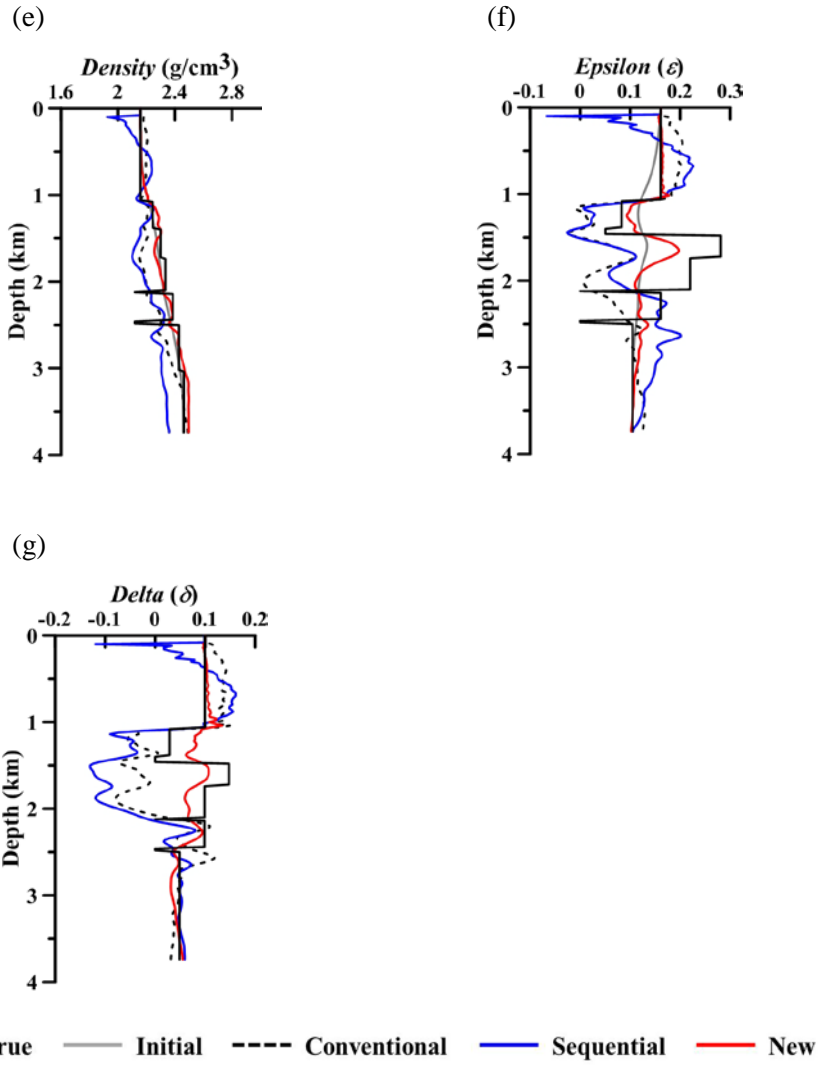


Figure 4.27 (Continued)

Figure 4.28 shows the reconstructed Poisson's ratio from the inverted parameters. The Poisson's ratio recovered by the sequential inversion is improved compared to that recovered by the conventional VTI inversion. The Poisson's ratio obtained by the new parameterization is better than that of the sequential inversion, although deeper parts of the model were not updated. These improvements by the new parameterization are identified in Figure 4.29.

Figure 4.30 shows RMS error curves of the performed inversions. In the case of this bench-marking model, the convergence rate of the conventional inversion is faster than that of the other inversion techniques. However, the convergence of the conventional inversion is not good compared to the new parameterization, and its value is very similar to that of the sequential inversion. These tendencies are also identified in Table 4.4. The model mismatch errors of the conventional and sequential inversions are very similar, whereas the model mismatch errors of the new parameterization are better than those of the other inversion techniques. These results indicate that the new parameterization provides improved inversion results without additional inversion steps compared to the conventional and sequential inversions.

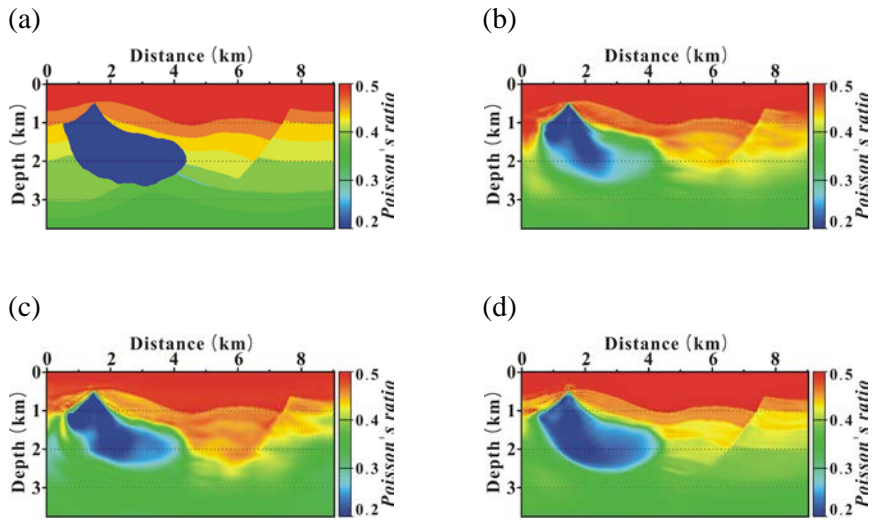


Figure 4.28 (a) True and reconstructed Poisson's ratio obtained by (b) the conventional, (c) the sequential and (d) the new inversion for the SEG/HESS VTI model.

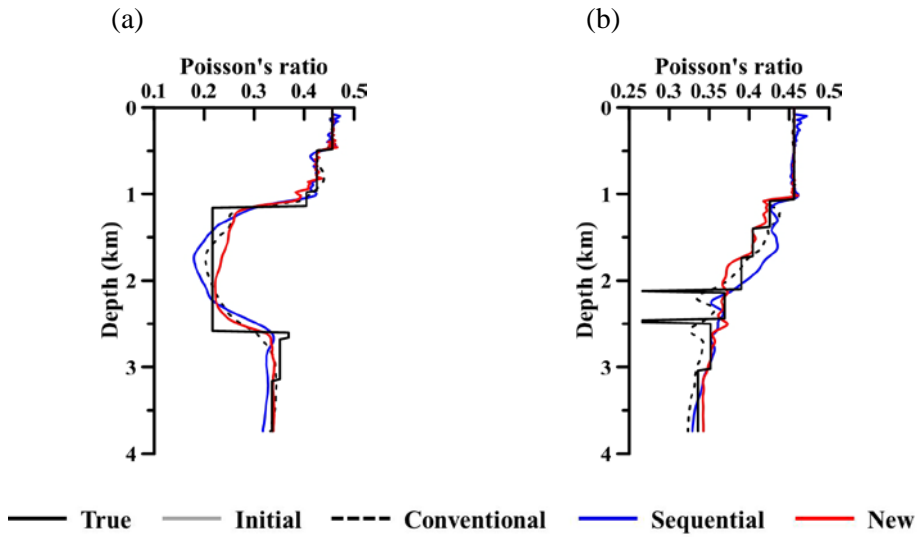


Figure 4.29 Poisson's ratio logs extracted at a distance of (a) 2.26 km and (b) 4.52 km of the (black solid line) true and inverted models obtained by (black dashed lined) the conventional, (blue solid line) the sequential and (red solid lines) the new inversion for the SEG/HESS VTI model.

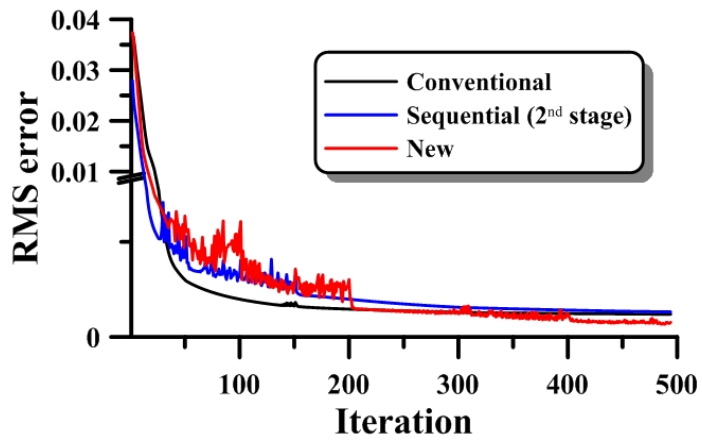


Figure 4.30 RMS error curves for (black solid line) the conventional VTI inversion, (gray dashed line) the isotropic inversion for first stage of the sequential inversion, (blue solid line) the conventional VTI inversion for second stage of the sequential inversion and (red solid line) new inversion for the SEG/HESS VTI model.

Table 4.4 Model mismatch errors of the final inversion results obtained by the conventional, sequential and new inversions for the SEG/HESS VTI model.

	C_{11} (%)	C_{13} (%)	C_{33} (%)	C_{44} (%)	ρ (%)	Poisson's ratio
Conventional	0.034	0.027	0.040	0.072	0.019	0.023
Sequential	0.036	0.037	0.043	0.075	0.019	0.028
New	0.028	0.025	0.032	0.058	0.007	0.018

Chapter 5. Conclusions

In 2-D elastic VTI media, it is difficult to reconstruct accurate elastic parameters including anisotropic parameters (ϵ and δ) and density by multi-parametric FWI due to the increased nonlinearity and the trade-off between parameters. For these reasons, the multi-parametric FWI was performed based on sequential strategies that first invert the primary parameters, which have strong influences on seismic data, and then invert the secondary parameters based on the inverted primary parameters. Therefore, the success of the sequential inversion is partly dependent on how well the primary parameters are inverted.

In this dissertation, a new parameterization using the Lamé constants is proposed based on the fact that the Lamé constants are recovered relatively well in the isotropic inversion. In this case, the Lamé constants become the primary parameters, which correspond to C_{33} and C_{44} in the conventional VTI parameterization, and all the elastic parameters are expressed by either the Lamé constants (λ and μ) alone or by a combination of the Lamé constants and two new parameters (ξ_1 and ξ_2). The new parameters represent the anisotropic characteristics of subsurface media, which correspond to C_{11} and C_{13} in the conventional VTI parameterization.

The Lamé constants in the new parameterization have scattering patterns of the partial derivative wavefields similar to those in the isotropic case, whereas the new anisotropy-related parameters retain the scattering patterns

of C_{11} and C_{13} in the conventional parameterization. This means the inversion results for the Lamé constants can be as good as those of the primary parameters in the isotropic case. The anisotropic parameters (C_{11} and C_{13}) can be improved because they are obtained through the improved primary parameters and the new parameters, although ξ_1 and ξ_2 are not improved directly by the new parameterization. The gradient directions obtained in the first iteration for the simple horizontal two-layered model showed that the new parameterization improves the resolution of μ compared to C_{44} in the conventional VTI parameterization (note that C_{44} corresponds to μ), and the new anisotropic parameters ξ_1 and ξ_2 yielded the same gradient directions as C_{11} and C_{13} in the conventional VTI parameterization. The new anisotropic parameters are the auxiliary parameters for C_{11} and C_{13} that are obtained by combining the Lamé constants, ξ_1 and ξ_2 . Accordingly, the inversion is not sensitive to ξ_1 and ξ_2 , and C_{11} and C_{13} are positively affected by the Lamé constants. This means that the improvements of the primary parameters can, in turn, enhance C_{11} and C_{13} , which is an advantage of the new parameterization.

To verify the effectiveness of the new parameterization, seismic FWIs were performed for the two bench-marking models, the SEG/EAGE overthrust model and the SEG/HESS VTI model. First, the conventional, sequential and new FWIs were applied to the modified and original versions of the overthrust model. For the modified overthrust model, the Poisson's ratio was assumed to be 0.25, and the density was regenerated using the Gardner's relationship. It was observed that the new parameterization

provides improved FWI results for not only the primary parameters but also the secondary parameters (anisotropic parameters and density) without an additional inversion stage, resulting in more reliable estimates of the Thomsen parameters and improvements in the computational efficiency. For the original model, where the Poisson's ratio is not homogeneous, the resolution of the FWI results is not as good as those for the modified version. However, the new parameterization generally gave more reliable results than the conventional and sequential inversions. In the FWI inversion of the SEG/HESS VTI model, the new parameterization provided improved inversion results for all the parameters, including density. In particular, the elastic parameters of the salt body were reconstructed well compared to those obtained by the sequential inversion. In addition, thin structures, which have very low anomalous values of the elastic parameters, were identified by the new parameterization. Thomsen parameters extracted from these improved inversion results were more stable and reliable.

These sensitivity analyses and synthetic FWI tests show that the new parameterization can provide more reliable subsurface properties than the conventional and sequential inversions for 2-D elastic VTI media achieving computational efficiency. Therefore, the new parameterization can be an effective method to overcome the intrinsic disadvantages of seismic inversion in anisotropic media.

To apply the new parameterization to real seismic data, some challenges still remain. It is well known that real seismic data are contaminated by noise and that seismic FWI is severely affected by strong noise. Furthermore, low

frequency components of real data are weak or meaningless. Some techniques should be combined with the new inversion technique to solve the noise and low frequency missing problems. In addition, 3-D seismic survey is commonly applied in oil and gas exploration. Therefore, the new parameterization also needs to be extended to the 3-D case to increase its applicability. These issues will be addressed in further work.

Bibliography

- Alkhalifah, T., 1998, Acoustic approximations for processing in transversely isotropic media, *Geophysics*, **63**, 623-631.
- Brossier, R., Operto, S. and Virieux, 2009, Seismic imaging of complex onshore structures by 2D elastic frequency-domain full-waveform inversion, *Geophysics*, **74**, WCC105-WCC118.
- Brossier, R., 2011, Two-dimensional frequency-domain visco-elastic full waveform inversion: Parallel algorithms, optimization and performance, *Computers & Geosciences*, **37**, 444-455.
- Cohen, G., 2002, High-order numerical methods for transient wave equations, Springer.
- Clayton, R. and Engquist, B., 1977, Absorbing boundary conditions for acoustic and elastic wave equations, *Bulletin of the seismological society of America*, **67**, 1529-1540.
- Daley, P. F. and Hron, F., 1979, Reflection and transmission coefficients for seismic waves in ellipsoidally anisotropic media, *Geophysics*, **44**, 27-38.
- Duveneck, E., Bakker, P. M., 2011, Stable P-wave modeling for reverse-time migration in tilted TI media, *Geophysics*, **76**, S65-S75.
- Ewing, W. M., Jardetzky, W. S. and Press, F., 1957, *Elastic waves in layered media*, McGraw-Hill Book Company Inc.
- Fletcher, R., Reeves, C. M., 1964, Function minimization by conjugate gradients, *The computer journal*, **7**, 149-154.

- Gardner, G. H. F., Gardner, L. W., Gregory, A. R., 1974, Formation velocity and density-the diagnostic basics for stratigraphic traps, *Geophysics*, **39**, 770-780.
- Gholami, Y., Ribodetti, A., Operto, S., Brossier, R., Virieux, J., 2010, Imaging of VTI media by elastic frequency-domain full-waveform inversion of global offset data, Proceedings of the 80th SEG annual meeting, Expanded Abstracts.
- Gholami, Y., Ribodetti, A., Brossier, R., Operto, S., Virieux, J., 2010, Sensitivity analysis of full waveform inversion in VTI media, 72nd EAGE Conference & Exhibition.
- Gholami, Y., Brossier, R., Operto, S., Ribodetti, A., Virieux, J., 2013, Which parameterization is suitable for acoustic vertical transverse isotropic full waveform inversion? Part 1: Sensitivity and trade-off analysis, *Geophysics*, **78**, R81-R105.
- Gholami, Y., Brossier, R., Operto, S., Prieux, V., Ribodetti, A., Virieux, J., 2013, Which parameterization is suitable for acoustic vertical transverse isotropic full waveform inversion? Part 2: Synthetic and real data case studies from Valhall, *Geophysics*, **78**, R107-R124.
- Gosselet, A. and Singh, S. C., 2006, Elastic Full waveform Inversion for CO2 Sequestration monitoring – 1D Synthetic Data Investigations, 68th EAGE Conference & Exhibition.
- Guittou, A., Symes, W. W., 2003, Robust inversion of seismic data using the Huber norm, *Geophysics*, **68**, 1310-1319.
- Higdon, R. L., 1986, Absorbing boundary conditions for difference

- approximations to the multidimensional wave equation, *Mathematics of computation*, **47**, 437-459.
- Ikelle, L., Amundsen, L., 2005, *Introduction to petroleum seismology*, Tulsa, OK: Society of Exploration Geophysicists, pp.92-95.
- Kelly, K. R., Ward, R. W., Treitel, S., Alford, R. M., 1976, Synthetic seismograms: a finite-difference approach, *Geophysics*, **41**, 2-27.
- Koo, J. M., Lee, H. Y., Jeong, W. D., Min, D. J., Yoo, H. S., 2010. Frequency-domain Elastic Full Waveform Inversion for VTI Media, 72nd EAGE Conference & Exhibition.
- Lee, H. Y., Koo, J. M., Min, D. J., Kwon, B. D., Yoo, H. S., 2010, Frequency-domain elastic full waveform inversion for VTI media, *Geophysical Journal International*, **183**, 884-904.
- Lines, L. R., Treitel, S., 1984, Tutorial: A review of least-squares inversion and its application to geophysical problem, *Geophysical prospecting*, **32**, 159-186.
- Liner, C. L., 2004, *Elements of 3D Seismology*, PennWell, USA.
- Marfurt, K. J., 1984, Accuracy of finite-difference and finite-element modeling of the scalar and elastic wave equations, *Geophysics*, **49**, 533-549.
- Nocedal, J., Wright, S. J., 1999, *Numerical optimization*. Springer, USA.
- Oh, J., Min, D., 2013, Weighting technique using backpropagated wavefields incited by deconvolved residuals for frequency-domain elastic full waveform inversion, *Geophysical Journal International*, **194**, 322-347.
- Operto, S., Virieux, J., Ribodetti, A., Anderson, J. E., 2009, Finite-difference

- frequency-domain modeling of viscoacoustic wave propagation in 2D tilted transversely isotropic (TTI) media, *Geophysics*, **74**, T75-T95.
- Pilant, W. L., 1979, *Elastic waves in the earth*, Elsevier Scientific Publishing Company.
- Pinder, G. F. and Gray, W. G., 1977, *Finite element simulation in surface and subsurface hydrology*, New York, Academic Press Inc.
- Plessix, R., É., Cao, Q., 2011, A parameterization study for surface seismic full waveform inversion in an acoustic vertical transversely isotropic medium, *Geophysical Journal International*, **185**, 539-556.
- Pratt, R. G., 1990, Frequency-domain elastic wave modeling by finite differences: A tool for crosshole seismic imaging, *Geophysics*, **55**, 626-632.
- Pratt, G., Shin, C., Hicks G. J., 1998, Gauss–Newton and full Newton methods in frequency–space seismic waveform inversion, *Geophysical Journal International*, **133**, 341-362.
- Pratt, R. G., 1999, Seismic waveform inversion in the frequency domain, Part 1: Theory and verification in a physical scale model, *Geophysics*, **64**, 888-901.
- Prieux, V., Brossier, R., Operto, S., Virieux, J., 2013, Multiparameter full waveform inversion of multicomponent ocean-bottom-cable data from the Valhall field. Part 1: imaging compressional wave speed, density and attenuation, *Geophysical Journal International*, **194**, 1640-1664.
- Pyun, S., Son, W., Shin, C., 2009, Frequency-domain waveform inversion using an l_1 -norm objective function, *Exploration Geophysics*, **40**, 227-

232.

- Reynolds, A., 1978, Boundary conditions for the numerical solution of wave propagation problems, *Geophysics*, **43**, 1099-1110.
- Shin C., 1995, Sponge boundary condition for frequency-domain modeling, *Geophysics*, **60**, 1870-1874.
- Shin, C., Yoon, K., Marfurt, K. J., Park, K., Yang, D., Lim, H. Y., Shin, S., 2001, Efficient calculation of a partial-derivative wavefield using reciprocity for seismic imaging and inversion, *Geophysics*, **66**, 1856-1863.
- Shin, C., Min, D. J., 2006, Waveform inversion using a logarithmic wavefield, *Geophysics*, **71**, R31-R42.
- Shin, C., Pyun, S. and Bednar, J. B., 2007, Comparison of waveform inversion, part1: conventional wavefield vs logarithmic wavefield, *Geophysical Prospecting*, **55**, 449-464.
- Tarantola, A., 1984, Inversion of seismic reflection data in the acoustic approximation, *Geophysics*, **49**, 1259-1266.
- Tarantola, A., 1986, A strategy for nonlinear elastic inversion of seismic reflection data, *Geophysics*, **51**, 1893-1903.
- Thomsen, L., 1986, Weak elastic anisotropy, *Geophysics*, **51**, 1954-1966.
- Tsvankin, I., Gaiser, J., Grechka, V., Bann, M and Thomens, L., 2010, Seismic anisotropy in exploration and reservoir characterization: An overview, *Geophysics*, **75**, 75A15-75A29.
- Virieux, J., 1986, P-SV wave propagation in heterogeneous media: Velocity-stress finite-difference method, *Geophysics*, **51**, 889-901.

- Virieux, J., Operto, S., 2009, An overview of full-waveform inversion in exploration geophysics, *Geophysics*, **74**, WCC1-WCC26.
- Wang, T., 2006, A weak-anisotropy approximation to multicomponent induction responses in cross-bedded formations, *Geophysics*, **71**, F61-F66.
- Zhou, H., Zhang, G., Bloor, R., 2006, An anisotropic acoustic wave equation for VTI media, 68th EAGE Conference & Exhibition.
- Zienkiewicz, O. C., 1977, the finite element method: New York, McGraw-Hill Book Co., 3rd ed.
- Zienkiewicz, O. C. and Taylor R. L., 2000, The finite element method, volume 1: The basis Butterworth-Heinemann.

초 록

2차원 횡등방성 탄성매질에 대한 주파수영역 탄성과 완전파형 역산

주요어: 탄성과 완전파형역산, 다변수, 횡등방성, 매개변수화, 탄성체
학 번: 2010-31015

본 학위논문에서는 2차원 횡등방성 탄성매질에 대한 탄성과 완전파형 역산의 결과를 향상시키기 위해 등방성 매개변수화와 유사한 새로운 매개변수화를 제안한다. 새로운 매개변수화에서는 이방성 매질의 탄성계수들(C_{11} , C_{13} , C_{33} 및 C_{44})을 대신하여 라메상수(λ 와 μ)와 매질의 이방성 특성을 나타내기 위한 새로운 변수들(ξ_1 과 ξ_2)로 매개변수화 된다.

일반적으로 이방성 매질에 대한 다변수 파형역산에서는 탄성과 자료에서 영향이 크고 역산이 잘되는 변수들을 우선적으로 역산한 후에 이 역산된 변수를 이용하여 추가적인 역산을 수행하는 단계적 파형역산기법이 많이 적용되고 있다. 이 경우 C_{33} 와 C_{44} 가 우선적으로 역산이 되는 변수들이다. 그러나 일반적인 횡등방성 매질에 대한 완전파형역산기술에서는 C_{44} 의 역산결과가 상대적으로 좋지 않기 때문에 전체 물성에 대한 역산결과가 좋지 못하다는 문제점이 있다. 또한 단계적 파형역산은 추가적인 역산수행이 필요하기 때문에 계산비용이 상승하는 문제점이 발생한다. 그러나

새로운 매개변수화를 이용할 경우 라메상수가 C_{33} 와 C_{44} 를 대신하게 되며, 새로운 변수인 ξ_1 과 ξ_2 를 통해 지해 매질의 이방성 특성을 얻을 수 있다.

새로운 매개변수화에서 라메상수는 등방성 역산에서의 라메상수와 동일한 편미분 파동장의 분산패턴을 가지고 있고, 새로운 변수들은 기존 VTI 매개변수화에서의 C_{11} 과 C_{13} 의 분산패턴과 동일한 분산패턴을 가지고 있다. 이러한 특성은 라메상수는 기존 등방성 파형역산기술과 유사한 높은 분해능을 가질 수 있으며, C_{11} 과 C_{13} 는 라메상수와 ξ_1 과 ξ_2 로 얻어질 수 있기 때문에 향상된 역산결과를 기대할 수 있다. 새로운 매개변수화를 통한 역산결과의 향상은 최대 급경사 방향을 직접적으로 비교함으로써 확인할 수 있었다. 매우 복잡한 지층모델에 대한 역산결과에서는 새로운 매개변수화가 추가적인 역산 수행 없이도 이방성계수 및 밀도를 포함한 탄성계수들을 보다 정확하게 제공한다는 것을 확인할 수 있었다. 아직까지 실제 현장자료에 대해 적용하기 위해서는 제한적인 저주파수 성분의 이용과 현장잡음에 대한 문제점들이 남아있지만, 새로운 매개변수화는 이방성 완전파형역산의 본질적인 단점을 극복할 수 있는 효과적인 방법이 될 수 있을 것으로 기대된다.

새로운 매개변수화의 현장자료 적용성을 향상시키기 위해서는 현장자료에 존재하는 잡음의 영향과 제한적인 저주파 성분 이용에 따른 문제점을 극복할 수 있는 기법 개발에 대한 연구가 필요하다. 또한 최근에는 3차원 탐사가 활발히 적용되고 있기 때문에 3차원 자료에 대한 적용성 연구 또한 진행되어야 할 것으로 판단된다.